MODELLING 3D SEISMIC WAVE PROPAGATION IN MARMARA REGION

by

Seda YELKENCİ

B.S. Geophysical Engineering, İstanbul University, 2002

M.S. Geophysics, Boğaziçi University, 2006

Submitted to the Kandilli Observatory and

Earthquake Research Institute in partial fulfillment of

the requirements for the degree of

Doctor of Philosophy

Graduate Program in Geophysics

Boğaziçi University

2016

MODELLING 3D SEISMIC WAVE PROPAGATION IN MARMARA REGION

APPROVED BY:

Prof. Dr. Mustafa Aktar   …………………..……

(Thesis Supervisor)

Assist. Prof. Dr. A. Özgün Konca   …………………..……

Prof. Dr. Semih Ergintav   …………………..……

Boğaziçi University, Dep. of Geodesy

Prof. Dr. Argun Kocaoğlu   …………………..……

Istanbul Technical University

Assist. Prof. Dr. Tuna Eken   …………………..……

Istanbul Technical University

DATE OF APPROVAL: 31.05.2016

ACKNOWLEDGEMENTS

ABSTRACT

MODELLING 3D SEISMIC WAVE PROPAGATION IN MARMARA REGION

This study focuses on the modeling of 3D seismic wave propagation in the east of the Marmara Sea in particular for the city of Istanbul, which is identified as one of the megacities with the highest seismic risk in the world. For the first time, an attempt is made for creating a 3D seismic model and for testing the new model with real data. In the frame of constructing 3D velocity model, previous crustal studies of Marmara region and all other available field data, including surface and borehole measurements, are compiled to form a collection of 1D models. Each 1D model relates to a specific location point inside the study area. We have used interpolation methods, in particular Delaunay triangles approach, in order to fill in the no-data zones, which separate the 1D observation points. Elastic wave propagation is simulated inside the newly created 3D model using finite difference approach. An open source code called Wave Propagation Program (WPP), which operates on parallel processing environment, is used for that purpose. We have tested the performance of the 3D model with real data using the earthquake of September 29, 2004 (Ml=4.1) occurred in Çınarcık Basin, which was recorded by 18 permanent broadband stations and 100 strong motion stations. A detailed analysis of the source properties of the event is done, both for the location and the fault plane solution. Real and synthetic waveforms are compared both in time and frequency domains. Matching of the waveform shapes are studied in detail. In each case improvement of 3D model over 1D counterpart is discussed. A more quantitative evaluation of 1D and 3D performances is carried out using waveform correlation. The final result shows that a considerable improvement is achieved with 3D model both in terms of amplitudes and P and S arrival times. The finite difference method is also applied to specified basin structures filled with soft sediments of low shear velocities. Sabiha Gökçen Airport area in Pendik, is studied in detail because its basement geometry and sedimentary cover are well-known. The analysis, performed both in the time and frequency domain, helps to understand the characteristics of the 3D wave propagation inside the basin and the site effects related to it.

ÖZET

MARMARA BÖLGESİ İÇİN 3B SİSMİK DALGA YAYILIMI MODELLEMESİ

Çalışma kapsamında, Marmara denizinin doğusunda, spesifik olarak İstanbul ve çevresinde üç boyutlu sismik dalga yayınımı modellemesi yapılmıştır. Bu çalışma ile ilk kez birleştirilmiş bir 3 boyutlu sismik model oluşturulması ve bu modelin gerçek veriler ile test edilmesi girişiminde bulunulmuştur. 3B hız modeli oluşturulması aşamasında, Marmara bölgesinde önceden yapılmış kabuk çalışmaları ile İstanbul'da yapılmış tüm arazi ölçümleri (kuyu logları ve yüzey ölçümleri) bir araya getirilerek 1B hız modelleri derlenmiştir. Böylece, çalışma alanı içinde belli noktalara ait 1B modeller oluşturulmuştur. Çalışma bölgesinde yer alan 1B ölçüm noktaları dışında very olmayan noktaların doldurulması için çeşitli interpolasyon tekniklerinden Delaunay üçgenleri yaklaşımı kullanılmıştır. Oluşturulan 3B model içinde sonlu farklar yaklaşımı kullanılarak elastik dalga yayılımı modellenmiştir. Bu amaçla, parallel işlem çevrelerinde çalışan yeni bir sonlu farklar kodu, Dalga Yayılımı programı (WPP) kullanılmıştır. 3B modelin performansı gerçek veriler ile test edilmiş ve bu aşamada 29, Eylül 2004 tarihinde Çınarcık baseninde meydana gelen ve 18 broadband istasyon ile 100 strong motion istasyonu tarafından kaydedilen 4.1 büyüklüğündeki deprem kullanılmıştır. Bu depreme ilişkin lokasyon ve fay düzlem çözümü açısından detaylı analizler yapılmıştır. Gerçek ve sentetik dalga formları zaman ve frekans ortamında karşılaştırılmıştır. Her durumda 3B modelin 1B modele göre gelişimi tartışılmıştır. Dalga formları korelasyonu ile 1B ve 3B model karşılaştırmaları daha kantitatif olarak değerlendirilmiştir. Elde edilen sonuçlara göre, 3B model ile hem genlikler hem de geliş zamanları açısından kayda değer gelişmeler sağlanmıştır. Sonlu farklar yöntemi ayrıca düşük hızlara sahip sedimanlarla dolu olan lokal havza yapılarına da uygulanmıştır. Bu amaçla geometrisi ve sedimanter özellikleri iyi bilinen bir alan olan Sabiha Gökçen havaalanı bölgesi detaylı olarak çalışılmıştır. Zaman ve frekans ortamında yapılan analizler, bölgede sismik dalga yayınımı özelliklerinin araştırılmasına yardımcı olmuştur.

TABLE OF CONTENTS

LIST OF FIGURES

LIST OF TABLES

LIST OF SYMBOLS

N	Number of reference locations
k	Number of points in convex hull boundary
$\frac{V_p}{V_s}$	Poison ratio
V_p	P wave velocity
V_s	S wave velocity
L_{min}	Minimum wavelength
f_{max}	Maximum frequency
f_o	Center frequency
P	Number of grid points per smallest wavelength
ρ	Density
μ	Rigidity
λ	Lame constant
h	Grid size
N_{samp}	Number of sample points
N_{grid}	Number of grid points
T_{total}	Signal Duration
dt_{true}	True sampling rate
dt_{limit}	Limit sampling rate
λ	Slip angle
δ	Dip angle
ϕ_s	Strike angle
i_ξ	Take off angle
ϕ	Azimuth
R^{SH}	SH radiation pattern
R^P	P radiation pattern

LIST OF ACRONYMS/ABBREVIATIONS

NAF	North Anatolian Fault
EAF	East Anatolian Fault
RR	Rapid Response
1D	One-dimension
3D	Three- dimension
FPS	Fault Plane Solution
4D	Four Dimension
OBS	Ocean Bottom Seismometer
NMT	North Marmara Trough
REMI	Refraction Microtremor
PS Log	Suspension P-S velocity logging
JICA	Japan International Cooperation Agency
WPP	Wave Propagation Program
EW	East- West direction
NS	North- South direction
FDM	Finite-difference method
SEM	Spectral-element method
BEM	Boundary-element method
FEM	Finite-element method
SBP	Summation by parts
MPI	Message Passing Interface
ODE	Ordinary Differential Equation
PDE	Partial Differential Equation
CPU	Central Processing Unit
CFL	Courant-Friedrichs-Lewy
DWNM	Discrete Wave Number Method
SAC	Seismic Analysis Code
GMT	Generic Mapping Tool
ITU-UYBHM	ITU High performance computing center.
TUBITAK-ULAKBIM	TUBİTAK Ulusal Akademik Ağ ve Bilgi Merkezi

TRUBA	Türk Ulusal e-Bilim e-Altyapısı
BTIM	Regional Earthquake–Tsunami Monitoring Center
IEEWRR	Istanbul Earthquake Early Warning and Rapid Response
KOERI	Kandilli Observatory and Eaerthquake Research Institute
RMS	Root mean square
FAS	Fourier Amplitude Spectrum

1. INTRODUCTION

The North Anatolian Fault (NAF) is well-known for the western migration of destructive earthquakes during the second part of the 20th century (Stein *et al.,* 1997). In Marmara Region, the disastrous results of the 1999 Izmit and Duzce earthquakes revealed the dimension of the seismic risk in the western part of the NAF. Therefore, especially the city of Istanbul with more than 15 million inhabitant is under a significant seismic risk due to its close distance to the NAF. In fact it is widely recognized as being one of the megacities with the highest seismic risk in the World. Investigation of the wave propagation around the Marmara Sea, and in particular for Istanbul, is one of the key issues for the hazard mitigation.

The modeling of 3D seismic wave propagations is an important topic both for the physical and engineering aspects of the science of seismology. Different numerical methods were developed for that purpose. In particular, 3D geometries have been considered for some sedimentary basins around the world: Olsen and Archuleta (1996) and Olsen (2000) used finite differences to simulate the ground motion in the Los Angeles Basin and construct site amplification maps for the region. Olsen *et al.* (1995) studied the propagation of P waves in the Salt Lake Basin. Frankel and Stephenson (2000) computed the ground motions in the Seattle region. Frankel *et al.* (2001) have evaluated in detail the effects of a deep sedimentary basin and shallow sedimentary deposits on earthquake ground motions in San Jose, California. Rodgers *et al.* (2005) have studied the simulation of the 1906 San Francisco Earthquake and showed the ground motion and the curl of the velocity at the surface shortly after initiation. They also simulated the moderate earthquakes using the USGS regional model and provided some tests for its validity. Their results identify some elements and/or regions of the model that need further improvements (Rodgers *et al.,* 2008). The common characteristics of most the above studies is that they are of regional scale, in other words they cover a large area and therefore are concerned only with the lower frequency band of the seismic spectra (<0.5 Hz). Increasing the frequency band is often not realistic due to the limited knowledge of both the shallow and the deep crustal structure. Local studies with high frequency coverage are rare and often do not include any real data. An example of such study of local scale is the one by Skarlatoudis *et al.* (2011) who examined the wave propagation

characteristics and the spatial distribution of site effects in the Thessaloniki city with the finite-difference method.

As far as Marmara Region and the city of Istanbul is concerned, 3D wave propagation approach are very rare. Sørensen *et al.,* (2006) estimated the local site effects in the Atakoy area (southwestern Istanbul) by applying several techniques using synthetic data (hybrid 3-D modeling and 1-D modeling) and comparing to empirical data using the applied hybrid 3-D FD procedure for calculating spectral amplifications. This study concern a very limited coverage as compared to our study area.

On the other hand, there are quite a number of geological-geotechnical studies for hazard which do not used waveform simulation and are only based on site response approaches. In particular for the regional scale, Marmara region has been subject to several studies since 1999 mostly for engineering purposes (e.g. Atakan *et al.,* 2002; Erdik *et al.,* 2003a; Erdik *et al.,* 2004). Pulido *et al.* (2004) and Birgören *et al.* (2004) performed strong ground motion simulation for the Sea of Marmara region with emphasis given to fault rupture scenarios. Picozzi *et al.* (2009) proposed a microzonation characterization for the western part of Istanbul. They also calculated theoretical site responses from the S-wave velocity profiles obtained from the micro-array data using the propagator matrix method for a 1D-layered medium.

This study makes an attempt for the precise simulation of the 3-D wave propagation in and around the city of Istanbul. The work comprises mainly two parts. In the first part, a 3D seismic velocity model is developed, which is the first of its kind in terms of coverage area and precision. The model is developed in two steps, namely the deep and the shallow parts, which includes processes relatively independent from each other. The deep structure concerns depths greater than 1km and uses relatively coarser grid spacing. It is constructed by the combination of 1D velocity models, which are derived from earlier studies in the Marmara region, such as refraction seismic, tomography and receiver functions (Karabulut *et al.,* 2002; Zor *et al.,* 2006; Bayrakçı G., 2009; Bécel *et al.,* 2009; Bécel *et al.,* 2010; Bayrakçı *et al*., 2013). The velocity structure for the shallower part is confined to the upper 1 km and in particular to the top few hundred meters. It is derived from the recent geophysical and geotechnical surveys carried out by the Istanbul Municipality

microzonation study for Eastern European part, (2007) and Anatolian part, (2009) of the Istanbul as well as from other related studies (Birgören *et al.,* 2009; Özgül, 2011). The 3-D model is constructed by combining the already available 1-D models, using interpolation approaches, in particular the well-known Delaunay triangulation techniques (Delaunay, 1934). The final 3D velocity model extends from Moho to the surface and includes details of the shallow structures of the order of few tens of meters.

The second part of the study concerns the testing of the constructed model with real earthquake data. First an appropriate software infrastructure is built to simulate the 3-D wave propagation. In this thesis we have used a new 3-D finite difference tool (WPP) developed at National Lawrence Livermore Laboratories and made available for public use (https://computation.llnl.gov/project/serpentine/). The code defines second order accurate discretization of elastic wave equation based on energy stability (Nilsson *et al.,* 2007). The code is operated in parallel processing environment and it was built on two national high performance laboratories at ITU-UYBHM and at TUBITAK-ULAKBIM systems. Tests are carried out for selecting the optimal operational parameters suited for our particular geometry. We have also calibrated the results with those of the well-known 1D methods for waveform synthetics (Bouchon, 1970). The computational domain in our case includes a rectangular volume of 63.5 x 36.6 x 20 km and with an average grid spacing of 100 m. Using mesh refinement property we were able to resolve frequencies up to 1.6 Hz, in zones with a minimum shear velocity of 230m/s.

The second critical step in model testing is to find a real event, which was recorded by sufficient number of stations located inside the study area. One moderate size earthquake occurred in the Marmara Sea within the boundaries of the study area (Ml=4.1, 29 September 2004) was found to be suitable for the testing purpose. This event was recorded not only by the National Seismic Network of Turkey but also the strong motion network of Istanbul Earthquake Early Warning and Rapid Response System (IEEWRR). The source properties of this event are analyzed with unprecedented details. Source location is improved by including a total of 115 P and 81 S phase reading and by appropriate modification of earlier crustal models (Bulut *et al.,* 2007; Karabulut *et al.,* 2002). The fault plane solution of the event was determined using a multi stage estimation process starting with the classical P-wave first motion approach and evolving to P and S-wave amplitude fitting. The best fitting

of P and SH waves amplitude for real and theoretic values resulted in a right lateral strike slip motion in agreement with the NAF. Accurate estimation of the location and the focal mechanism for the test event provided an excellent tool to study the performance of the 3D modeling. We have found a significant improvement in terms of both the amplitude and the arrival time of P and S-wave were achieved by 3D modeling.

Finally the application of the 3D wave propagation method is used to investigate the seismic response of some of the major basins in the study area. In particular the shallow basin of Sabiha Gökçen airport is studied in detail with synthetic data. The performed analysis is carried out both in the time and frequency domain. Observations are made on situations where the 3D effects become important, and site amplification from the simple 1D model fail to provide a realistic description.

The work presented by an overview of geological and tectonic evolution of the study region, in Chapter 2. The description is given at three different scales: Marmara region, city of Istanbul, and local basins.

In chapter 3, we present the basic approach for developing the 3D velocity model. This is done in two stages namely, the deeper and the shallower parts. Previous studies, which provide the backbone data for the development of the 3D model, are also presented in this same chapter. Finally, the results are given using subparallel N-S cross sections.

In chapter 4, a review of the basic numerical tools for modeling the seismic wave propagation is given. This is followed by a comprehensive overview of Finite difference method in seismic applications. Additionally, the finite difference code used in our application, namely WPP is presented in terms of its general properties. We next present a verification of the WPP by comparing the results to a well-established 1D method (DWNM by Bouchon (1981). Finally details on the parallel computations are presented in terms of CPU time, CPU efficiency, etc.

In chapter 5, we describe the real data available for the testing of the 3D model. All earthquakes, which triggered the rapid response stations, are presented as part of data availability. We then present the selection of the reference event that will be used for the

testing. We also show how estimation of the earthquake location and of the fault plane solutions is improved by the use of more advanced techniques. The complete description of data processing and the analysis steps for the location and focal mechanism are also given.

Chapter 6 contains an extensive presentation of the testing results. We describe how we compare the observed and the synthetic data for both the 1D and the 3D models. The results are given in two ways: a direct comparison in time domain and a comparison of amplitude spectra in the frequency domain. We also present the results of an automatic comparison in time domain, both for the amplitude and the arrival time of the main source pulse. We present an overall quantitative evaluation of the performance improvement due to 3D modeling.

In chapter 7, as the last part of our study, we investigated in detail the seismic behavior of the shallow basins located inside the study area. The key question here is to see how much the amplification is modified by the 3D structure of the basin. 3D wave propagation and local amplification properties are investigated by both time and frequency domain analysis.

In chapter 8, the thesis concludes with the main outline of the work and a summary of results obtained from 3D velocity modeling. We also include some discussions and suggestions for future studies.

2. GEOLOGICAL AND TECTONIC FRAMEWORK OF THE AREA

Tectonic evolution and structural geology of the region can be explained in three different scales, namely the Marmara region, city of İstanbul, and local basins. In the first section of this chapter, basic information about the Marmara Region and the North Anatolian Fault Zone (NAFZ), based on geodynamical context is given and then geological properties of the Marmara Region are explained. In a second section, structural and lithological characteristics of the geological formations exposed within the city of Istanbul are described. Different types of Plio-Quaternary deposits encountered in İstanbul metropolitan area are discussed in the last section.

2.1. Marmara Region

2.1.1. Geodynamic aspect of the Marmara Region and the NAFZ

Before discussing geodynamic structure of the Marmara region and the NAFZ, the tectonic evolution of Turkey is briefly reviewed here. Turkey is made up of different pieces of ancient continental and oceanic blocks, stuck together in the Tethyan oceanic realm by younger igneous and sedimentary rocks (Okay, 2008). It is known that the Tethyan Ocean, which is established between Laurasia and Gondwana, was not only continuous oceanic plate. It rather composed of unequal sized continental segments throughout its history. This characteristic structure of the Tethyan realm is well reflected on the geology of Turkey (Figure 2.1). During the evolution of Tethyan oceans continental fragments rifted from the Gondwana margin and, as the rifts widened, oceans (mainly described as Prototethys, Paleotethys and Neotethys in the literature) were created. These continental fragments subsequently collided with Laurasia so that these oceans sequentially closed. The present tectonic regime is the consequence of the closure of the Neotethyan Ocean (Görür *et al.,* 1997).

Turkey is located at the collisional boundary between Afro-Arabian plate in the south and Eurasia in the north, forming an east-west trending fragment of the Alpine-Himalayan orogenic belt (Dewey and Şengör, 1979). Many scientists have been engaged in studies of

this area, because, along with the Andes and the Alp-Himalayan collisional belts, Turkey is one of the best regions for testing hypotheses relating to the subject of which forces drive active surface deformation while continental collision induces strong resistance (Becker and Faccenna, 2011). Looking at the eastern Mediterranean, geodetic velocity maps indicate a rapid westwards extrusion of Anatolia away from the Arabia plate (McClusky *et al.,* 2000; Reilinger *et al.,* 2006). The Arabia push was initially considered as the main force driving the relative motion of Anatolia with regard to Eurasia, with the consequent localization of shear on the NAFZ (e.g., Dewey and Şengör, 1979; Armijo *et al.,* 1999). However, the geodetic data of Reilinger *et al.* (2006) refer that there is no fault-normal convergence on the East Anatolian fault that marks the boundary between Anatolia and Arabia, which implies that the Arabia push is not the main cause of the present motion of Anatolia. In addition, abundant tectonic and petrologic data collected by some scientist (e.g., Le Pichon and Angelier, 1979, 1981; Lister *et al.*, 1984; Brun and Faccenna, 2008; Jolivet *et al.*, 2013) indicate strong back-arc distribution in the Aegean Sea due to the retreat of the Hellenic trench since the early Miocene. According to this, the fast retreat of the Hellenic trench and the related slab pull is considered to be the main forces that drive the westwards motion of the Anatolian microplate (Jolivet *et al.*, 2013).

The geodetic evaluation of McClusky *et al.*, (2000) indicates that the African and Eurasian lithospheric plates converge at a rate of ~1 cm/yr, while distortion of the Aegean is fast and strong, and convergence across the Hellenic Trench is >4 cm/ yr. This implies that internal deformation affects the Aegean region (Le Pichon and Angelier, 1979; England et al., 1985; Hatzfeld *et al.,* 1997). This internal deformation is certainly fast as referred by the presence of major active crustal faults, by the seismic activity, and by the thinning of the crust (Hatzfeld, 2001). Taking into account the eastern side of the Anatolian microplate, the Bitlis suture/thrust zone and the East Anatolian strike-slip fault (EAF) show a distributed, irregular and young continental collision zone as suggested by Jackson and D. McKenzie (1984). It is stated that the 2km topographic high of Anatolian plateau which is representing the Arabia-Eurasian plate boundary is underlain by uppermost mantle with excessively low seismic velocities (*Al Lazki et al*., 2003).
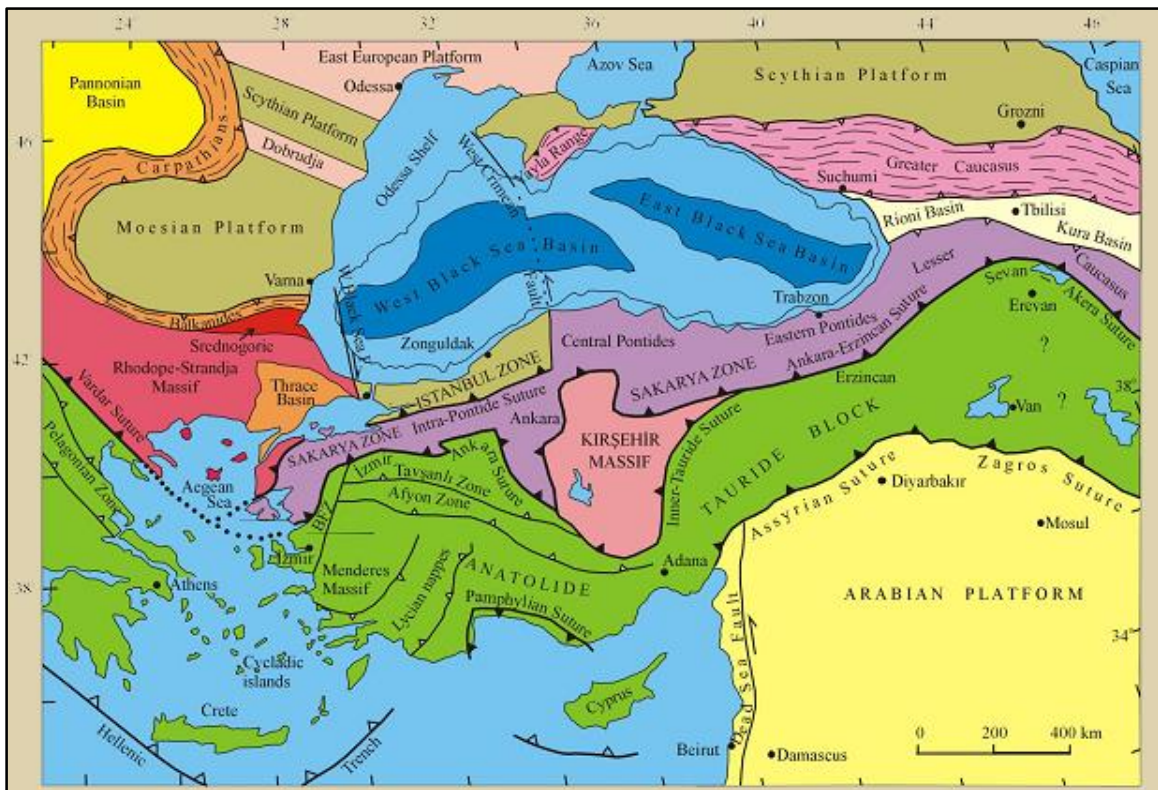
Figure 2.1. Paleo-tectonic setting for Turkey (from Okay and Tüysüz, 1999)

We particularly review the basic tectonic and geological properties of the NAF because it has significant impact on the tectonic evolution of Marmara region. As known, the NAF system stretches across the northern part of Turkey in east-west direction for more than 1500km. It accommodates an average slip of 25mm/yr with right-lateral behavior between the Anatolian and the Eurasian Plates (McClusky *et al.,* 2000). This fault zone lies down from the Karlıova Junction where it joins the EAF, to the Gulf of Saros in western Turkey, and then further west through The North Aegean Trough (Gürer *et al.,* 2006). As a consequence, Marmara Region, located in a transition zone, which joins the right lateral strike-slip regime dominating in the western Turkey to the extensional deformation of the Aegean (Dewey & Sengor 1979; Sengor *et al*., 1985; Smith *et al,.* 1995). Looking at the northwestern part of Turkey, fault segments appear shorter and discontinuous which result in a number of basins such as the Iznik, Bursa, Karacabey, Manyas and Marmara Sea basins (Barka & Kadinsky-Cade, 1988). However, the Sea of Marmara is the largest of these basins, with its 280km length and 80km width (Gürer *et al.,* 2006). The Marmara Sea is an E-W directed intra-continental sea with complex sub-bottom topographic features, especially in

its northern part where three deep basins are located. These three deep basins are Tekirdağ basin to the western end, Çınarcık basin in the east and Central basin in the center. There is also a smaller and shallower basin between the Central and Çınarcık basin, which is called Kumburgaz Basin (Figure 2.2).
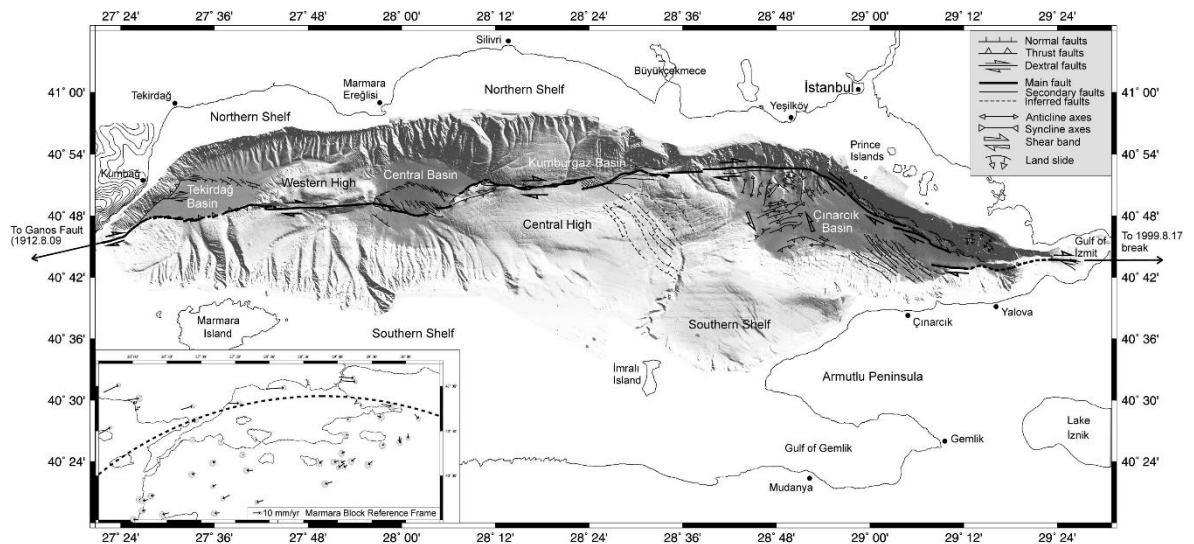
Figure 2.2. Principle sub-bottom features of the Sea of Marmara (Le Pichon *et al*., 2001).

Presently, details of the geometry of the NAF inside the Marmara Sea is still under debate so that it arouses interest of many scientists (Aksu *et al.,* 2000; Imren *et al.,* 2001; Le Pichon *et al.,* 2001; Le Pichon *et al.,* 2003; Yaltirak, 2002; Barka and Kadinsky- Cade, 1988; Wong *et al.,* 1995; Ergün and Özel, 1995; Armijo *et al.,* 2002; Armijo *et al.,* 2005; Parke *et al.,* 1999; Okay *et al.,* 2000; Siyako *et al.,* 2000). Different models have been suggested to express the complicated bottom morphology of the Sea of Marmara. One of these models describes the Marmara Sea as a pull-apart basin (Barka and Kadinsky-Cade, 1988; Wong *et al.,* 1995; Ergün and Özel, 1995; Armijo *et al.,* 2002; Armijo *et al.,* 2005). A second model considers the NAF as splitting into several en echelon structures in the Marmara Sea (Parke *et al.,* 1999; Siyako *et al.,* 2000; Okay *et al.,* 2000). A third model defines the NAF in the northern Marmara Sea as a through going, continuous fault structure (e.g. Aksu *et al.,* 2000; Imren *et al.,* 2001; Le Pichon *et al.,* 2001; Le Pichon *et al.,* 2003; Yaltirak, 2002). There are both evidences and counter evidences for all of these models, intensively discussed in the literature.

The age and the cause of the dextral motion along the NAF are even more controversial issues in the literature. Barka (2000) suggested that NAFZ was not initiated until the Latest Miocene or the Early Pliocene. Another suggestion put forward by Okay (1999) suggests that the NAF was initiated in the Eastern Anatolia in Late Miocene and transferred westwards reaching the Marmara Sea region during Pliocene. According to another opinion (Arpat and Şengör, 2000) the Sea of Marmara was a preexisting extensional basin prior to the westward development of the NAF. These authors state that The Marmara Sea and the North Aegean Trough have similar origin and the same geological age (Uppermost Miocene-Pliocene). They propose that the Marmara Sea region was a mountainous area forming the southern border of the Thracian Upper Eocene-Oligocene basin. Inversion of the topography started in Middle Miocene and a shallow sea branch invaded the area at the beginning of the Late Miocene. Deepening of both the Marmara Sea area and the North Aegean Trough occurred during Pliocene under local extensional stress regime. The right lateral NAF system entered these depressions in Late Pliocene, using the preexisting weakness zones those were developed under compressional forces that affected the whole northwestern Turkey at the end of Oligocene.

2.1.2. Geological Setting of the Marmara Region

Geologically, the Marmara Region contains three different tectonic zones, namely, Strandja massif, Istanbul zone and Sakarya zone according to Ketin (1973) and Okay (1986) (Figure 2.1). The Strandja Massif consists of sandstone, quartzite, limestone, shale and late Permian granitoid. All of these materials deformed and metamorphosed during Late Jurassic. The metamorphic rocks of the Strandja massif consist of metagranite, micaschist, marble, calcschist and quartzite (Ketin, 1973). Thrace basin filled by Cenozoic sedimentary rocks covers the southern part of the Strandja massif. The Intra-Pontide Suture in Thrace separates the Strandja-Rhodope Massif in the north from the Sakarya Zone in the south. It extends in an east-west direction under the Sea of Marmara between the spread outcrops of ophiolitic mélange in the Geyve-Armutlu area in the east, and around the Gulf of Saros and Şarköy in the west (Şengör and Yılmaz, 1981). The Istanbul zone covers a well- developed, unmetamorphosed, thick sedimentary sequence extending from Ordovician to Carboniferous age. Istanbul zone is very distinguishing from its surrounding tectonic units with respect to

its geological stratigraphy and lack of metamorphism (Ketin, 1973). Sakarya zone differs from İstanbul zone by not having a Paleozoic basement (Hoşgören, 1995).

The Izmir-Ankara Suture separates the Sakarya zone from the Anatolide-Tauride units. The Sakarya zone is characterized by a flexibly metamorphosed and hardly deformed Triassic basement. This is called by the Karakaya complex, overlain with a major unconformity by Liassic conglomerates and sandstones (Ketin, 1973). The sequence continues upward by Middle Jurassic-Lower Cretaceous limestone and Upper Cretaceous flysch (Hoşgören, 1995).

2.2. Local Geology of the Istanbul Metropolitan Area

The majority of the information in this section, unless indicated otherwise, is based on Özgül (2011) and Arpat, E., personal communication. Pre-Late Cretaceous formations cover large areas on both Anatolian and European parts of the city of İstanbul. They consist of two different tectono-stratigraphical units. One is a metamorphic assemblage named Strandja Unit (Ketin, 1973) and the other is an unmetamorphosed sedimentary series, which is called İstanbul Unit (Özgül, 2011). Upper Cretaceous volcano-sedimentary sequence, distinguished from the İstanbul Unit by a major thrust, covers large areas along the Black Sea coast (Figure 2.3).

Strandja metamorphic assemblage consists of gneisses, schists, quartzites with subordinate marbles. All of these metamorphic rocks are assigned to Permo-Triassic ages. The metamorphic mass was intruded by Cretaceous magmatic rocks.

İstanbul Unit overlies a Precambrian crystalline basement, not unveiled in İstanbul region. The Istanbul Unit itself forms a well-developed transgressive Ordovician to Carboniferous sedimentary series. Stable shelf-type carbonates and clastic deposits represent the Ordovician-Early Carboniferous period (Özgül, 2012). İstanbul Unit ends with a flysch deposit of Carboniferous age. A rather detailed geological map of the eastern part of the İstanbul area is given in Figure 2.4. A brief description of the lithological units shown on this map is given below. Özgül (2012) reviews İstanbul Paleozoic in detail.
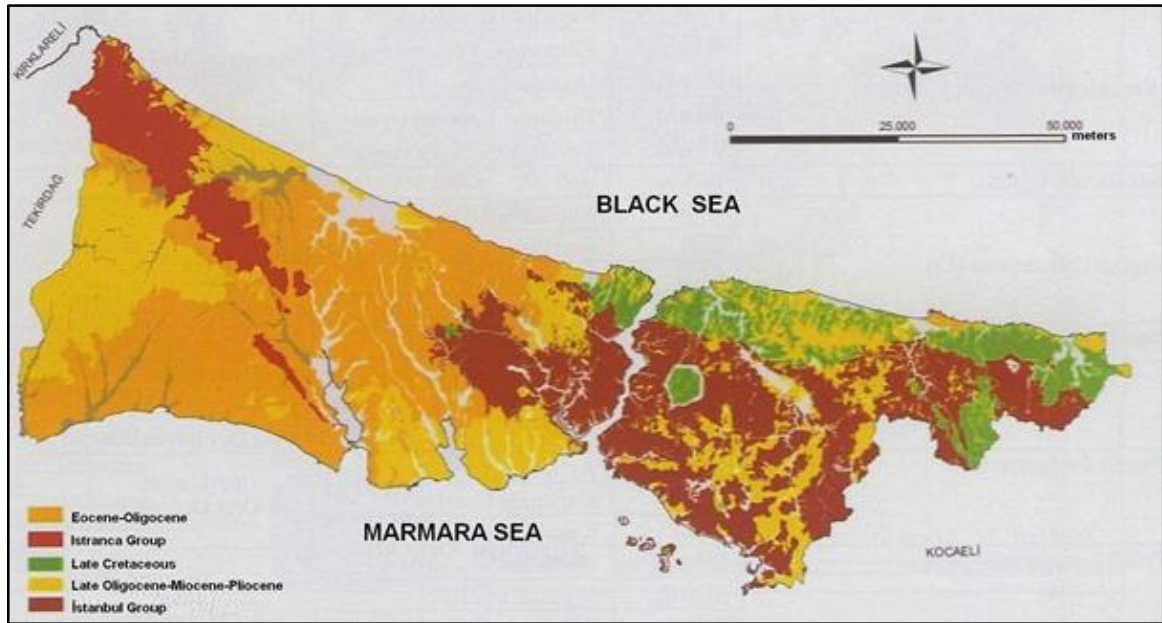
Figure 2.3. Map showing gross-scale geological outline of the İstanbul city area (from Özgül, 2011).

The basal part of the Paleozoic sequence comprises Kocatöngel and Kurtköy formations. Özgül (2012) stated that Kocatöngel Formation mainly comprise of laminated light green, thinly-to-medium bedded siltstone and mudstone with local fine-grained graded micaceous sandstone intercalations. Kurtköy Formation consists of purple arkosic clastic rocks. An Early Ordovician age has been assigned to Kocatöngel and Kurtköy formations.

Kurtköy Formation is conformably overlain by Kınalıada Formation. Kınalıada Formation subdivided to Gülsuyu and Manastırtepe members mainly consists of feldspathic quartz-arenites. No fossils have been observed in the Kınalıada Formation. However its stratigraphic position proposed a Middle-Late Ordovician age (Özgül, 2012).

Paleozoic sequence of İstanbul Unit continues upward by Aydos Formation of clayey siltstones enclosing quartzite lenses of different sizes. Quartzites creates the prominent hills in İstanbul region according to Özgül (2012). Aydos Formation is considered to be of Late Ordovician-Early Silurian in age.
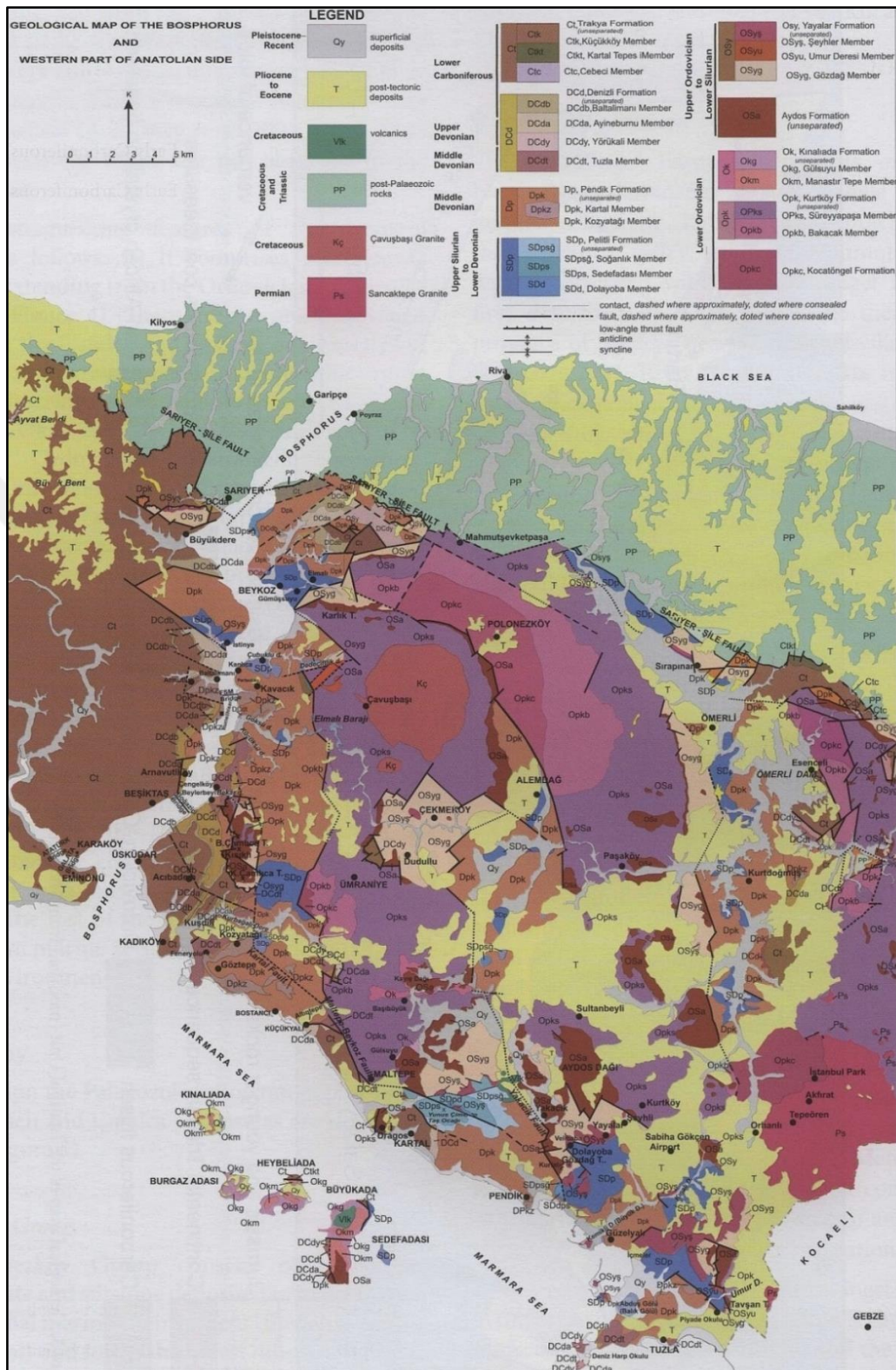
Figure 2.4. Detailed geological map of the eastern part of the İstanbul city area (from Özgül, 2012).

Özgül (2012) indicate that Yayalar Formation consisting principally of micaceous feldspathic sandstones lies with a conformable and transitional contact over the Aydos Formation. It encompasses several members, namely Gözdağ, Umurderesi and Şeyhli members. Dominant lithology for Gözdağ member is micaceous sandstone. Umurderesi member consists mainly of shales and siltstones, while Şeyhli member is a feldspathic quartzite sequence. Fossils content of the Yayalar Formation has been interpreted as being of Early-(?)Middle Silurian age.

In respect to definition of Özgül (2012), Kocatöngel, Kurtköy, Aydos and Yayalar formations, which are the widespread and thick clastic sequences, gives way to a carbonate deposition with the Pelitli Formation. This formation is defined by shallow marine limestone with a little intercalations of shale. According mainly of their shale content and carbonate textures several members have been differentiated in Pelitli Formation. These are Mollafenari, Dolayoba, İçmeler, Sedefadası and Soğanlık members. Özgül (2012) stated that a critical appraisal of the paleontological data show that the Pelitli Formation is of Early Silurian to Early Devonian age.

Pendik Formation gradationally overlies the limestone beds of the Pelitli Formation. It predominantly comprise of micaceous, fine grained clastic rocks with a limestone-rich horizon in its upper part (Olempska *et al.,* 2015). Kozyatağı Member is the name for this limestone-rich zone. The rest of the formation, rich in siltstone, shale and fine sand have been named Kartal member. Rich fossil fauna indicates an Early Devonian age for Pendik Formation.

The Pendik Formation is overlain conformably by the Denizli Köyü Formation. The Denizli Köyü Formation mainly comprise of limestone clayey limestone (Tuzla member), nodular limestone (Ayineburnu member), black chert (Yörükali and Baltalimanı members) and includes variable proportions of shale intercalations (Özgül, 2012). Deposition of the Denizli Köyü Formation covers an interval from Middle Devonian to the lowermost Carboniferous.

Uppermost formation of the İstanbul Unit is the Trakya Formation of Carboniferous age. Cebeciköy, Acıbadem, Kartaltepe and Küçükköy are the members of the Trakya

Formation. With the exception of Cebeciköy member which consists of limestone lenses, the Trakya Formation is a thick flysch sequence. This flysch of Early Carboniferous age marks the termination of the İstanbul Paleozoic sequence.

İstanbul Paleozoic terrane is covered by Triassic sediments in its easternmost part. A very strong angular disconformity exists between them. Jurassic and Lower and Middle Cretaceous are not developed in the region. However a thick volcano-sedimentary sequence of Late Cretaceous age forms a continuous belt along the İstanbul Black Sea coast. This sequence has been interpreted by Keskin and Ustaömer (1999) as beginning in an extensional environment passing to an island arc setting.

Paleocene-Lower Eocene deposits consisting of a siltstone-claystone sequence with olistostromal intercalations crop out in a limited area under a thrust sheet at the Black Sea coast. On the other hand, a thick sequence of limestone and marl-claystone of Late Eocene age covers large area in the Thrace basin and in its continuation in western İstanbul region. Limestone unit, named Soğucak Formation constitutes basal part of thick Late Eocene-Oligocene deposits filling an extensional basin of debated origin. Ceylan Formation, contemporaneous with the Soğucak Formation forms the deeper environment counterpart of it.

Following the deposition of the Ceylan Formation sedimentation continued in Thrace basin in a shallower environment. Deposits of that period are mainly of brackish water environment. Only Gürpınar Formation of this sequence crops out within the limit of the İstanbul city. It consists of claystone, siltstone and sandstone all of them being mainly derived from contemporaneous volcanic activity. Several tuff and tuffite units are discernible in the sequence.

Late Oligocene marks gradual upwelling of the Thrace and Marmara sea areas, and then evolution of an intensive compressional tectonic environment. These followed by an erosional phase during the Early Miocene epoch. Sediments of this epoch are of fluvial origin, deposited by a running water system developed on a pediment-like slope at the foot of a high area then located in the present Marmara Sea region. These fluvial deposits are known under the name of Kıraç Formation.

A sequence of processes of drastic inversion of topography started in the Marmara Sea region in the Middle Miocene time. A shallow inner sea developed in the area forming a gangway between Paratethys and the Mediterranean realm (Çağatay *et al.,* 2006). Brackish water sediments deposited in this shallow basin. Prominent formation of this period is called Güngören Formation. It consists of inter fingering clay, silt, sand and marl horizons. Brackish water limestone beds are encountered in the upper part of the sequence. In rare areas the limestone unit reaches a thickness of several meters and then in such situation it is differentiated under the name of Bakırköy Limestone. Çukurçeşme Formation is the name for gravel-sand deposits of fluvial, deltaic and in places of beach origin. It occurs mainly just above the Middle Miocene disconformity surface Miocene.

Younger sediments encountered in İstanbul city area are of Pliocene-Quaternary ages and are treated below in a separate chapter.

2.3. Local Young Deposits in the Istanbul City Area

The majority of the information in this section, unless indicated otherwise, is based on Özgül (2011) and Arpat, E., personal communication. Aside from the main Marmara basin, three different types of sedimentary environment can be identified in the İstanbul metropolitan area. These can be categorized as fluvio-lacustrine, torrential, and fluvial-estuarine environments (Arpat, E., personal communication).

Young sediments of fluvio-lacustrine origin cover rather large areas at the easternmost part in the İstanbul metropolitan area; namely, in Sultanbeyli, Orhanlı regions and in and around Sabiha Gökçen airport area (Figure 2.5). These sediments, gathered under the name of Sultanbeyli Formation, occupy interconnected lozenge shaped depressions. These depressions forming depositional environment for fluvio-lacustrine sediments are bounded by growth faults having dominantly NE-SW and NW-SE trends. Sultanbeyli Formation consists mainly of mildly compacted silty clays and clayey silts; but, coarser detrital sediments such as gravels and sands occur at the northern parts of the sub-basins. Sand and gravel deposits are interpreted as of fluvial origin: while, finer sediments were deposited in lacustrine environments. Data from boreholes clearly show that these basins were bordered by growth faults and shallow lakes taking place in these depressions were supplied sediments

from northerly creeks. These depressions were short-living features. Samples from organic-rich horizons have been determined being of Late Miocene-Lower Pliocene ages.

The origin of these depressions is believed to be contemporaneous with the medial stage of the generation of the Marmara Sea. Marmara Sea area was a rather high region during Early Miocene time, draining its water toward the Black Sea. Down warping of the Marmara Sea region dates Late Middle Miocene. During that stage a shallow sea branch entered the area and sediments of brackish water environment deposited. The present day morphology of the Marmara Sea area, with lozenge shaped depressions reaching 1000m depths, initiated during Early Pliocene. The North Anatolian Fault joined this area later, at the most a few million years ago. An explanation, amongst others, for the origin of North Aegean and Marmara troughs is the reactivation of preexisting conjugate shear fractures that had been formed under Oligocene compressional tectonics (Arpat and Şentürk 2003). Sultanbeyli Formation deposited in the continental counterpart of the Marmara Sea depression.

One of the consequences of the rapid effondrement of the Marmara Sea area is the occurrence of sudden diversions in the drainage system around the depression (Arpat, E., personal communication). This phenomenon caused widespread destabilization of the landforms. Chaotic fluvial deposits are the evidences testifying to this drastic change in the topography. These chaotic, sometimes torrential deposits have been gathered under the name of Altıntepe Formation. Main material of this formation consists of heterogeneous, angular fragments of rocks with huge blocks of different origin. Deposits of Altıntepe Formation are lenticular in shape. Maximum thickness is around 50m. Outcrops of Altıntepe Formation cover rather large areas in Kozyatağı, Göçbeyli, and Yeni Sahra.

Another deposit, a somewhat problematical one, encountered in the Istanbul metropolitan area is unconsolidated estuarine and alluvial sediments deposited in valleys surrounding the Marmara Sea (Arpat, E., personal communication). The name for these deposits is Kuşdili Formation. They are incised-valley fills. They exhibit a record of depositional system responses to changes of glacioeustatic sea-level. Due to sea-level fluctuations up to 110m during Pleistocene, several creeks flowing toward the Marmara Sea exhibit alluvial drawning along their lower courses. Thickness of these alluvial prisms

reaches 100m in regions neighboring the sea. Lower part of these prisms consist of unconsolidated estuarine deposits, of sapropelic character in places. These deposits are prone to liquefaction and constitute a threat in the context of earthquake-induced ground shaking. Kuşdili Formation has been particularly developed in Karasu, Sazlıdere, Alibeyköy, Kâğıthane, and Kurbağalıdere valleys.
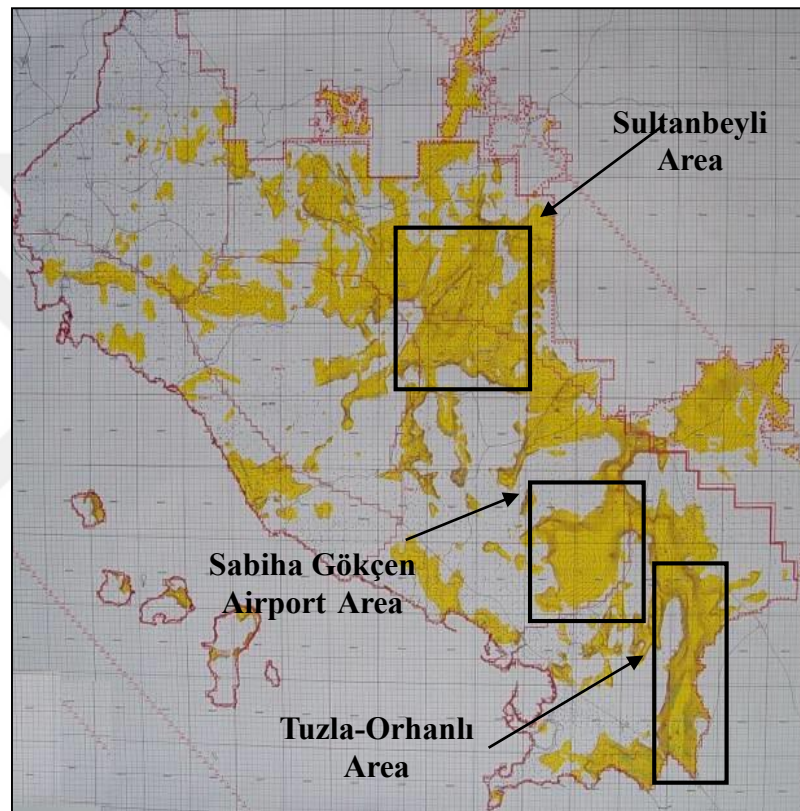
Figure 2.5. Young sedimentary basins (yellow areas) of the Anatolian side of the Istanbul area.

3. DEVELOPMENT OF 3D VELOCITY STRUCTURE

3.1. Introduction

The earthquake hazard can be best estimated in reliable way if a realistic crustal model and stable wave propagation algorithm are available. One of the most important necessary conditions of obtaining meaningful results with seismic wave propagation is creating a detailed and realistic crustal model. Therefore, development of an integrated 3D seismic/geologic model is one of the basic targets of the study. Such model will be the basis to understand seismic behavior of the city of Istanbul and surrounding in the case of a major seismic event occurring in the Sea of Marmara.

The approach followed in this work follows two stages: first a coarse model is developed for the deeper parts and then details of shallow structures are added on top of it. In accordance with this purpose, first a development of deep velocity model is needed based on the information about the 3D depth topography of the Moho surface as well as the smooth lateral variation of the velocity at deeper scale. At second stage, details of shallow structures needs to be added to reflect the characteristics of the local basins and other geologic formations in and around Istanbul. In the modelling stage, the general approach is to combine all the existing 1-D velocity information into a single comprehensive 3-D velocity model using an appropriate interpolation method. This interpolation procedure is repeated twice for both the deep and the shallow structures independently, and the outcomes are combined to form a single integral model. The deep model comprises the crust down to Moho including the layer below the Moho which is considered as half space. The shallower structure extends down to a maximum depth of 1 km and contains more detail as compared to the deeper one. The two are combined simply by substituting the upper 1 km of the deep model by the detailed shallow model. In the first section of this chapter, the already existing sources of information for both scales are presented and discussed. Next the methodology used for creating the 3D velocity model is explained. This is followed by the actual application of the interpolation method to the existing data. Finally a general description of the resulting 3D velocity structure is presented by means of a number of cross sections in the NS directions.

3.2. Previous Studies

3.2.1. Deeper Structure

The deep velocity structure down to the depth of Moho is constructed based on the data from already published papers on crustal models. A close survey of previous studies for the crustal structure of Marmara region shows that, although intensive surveys were done for the marine part and in particular for the shallow structures, there is no single 3D velocity model developed for the whole region covering both marine and continent parts.

The first generation of crustal studies use local earthquakes as the seismic source and consists of finding the optimal crustal structure that minimize the arrival time error. Optimization tools such as VELEST (Kissling *et al.,* 1995a) were used in this context. These first line of studies used data from off-shore seismic sources observed at on-shore stations. As a result, the inferred velocity structure corresponds to a model which represents and average of both the marine and the land side of the Marmara Region. In this line, Gürbüz *et al*. (2000) used local micro earthquake activity to find a 1D crustal structure to be valid for the whole Marmara Region. Karabulut *et al.* (2002) investigated average P wave velocity for upper crust on the Eastern Marmara using the aftershocks of the 1999 earthquake sequence. The next generation of studies used the tomographic approach for developing 3-D models (Barış *et al*., 2005). Once again the lack of observation on the marine part (i.e. OBS) lead to a nonuniform distribution of hit counts among the nodes meaning a serious imbalance of tomographic resolution. Furthermore, since only local earthquakes with limited magnitudes were used in these studies, only the seismogenic zone was sampled properly, therefore ignoring structure below 15-20 km.

A parallel line of studies on the structure are based on receiver functions and aimed at providing pointwise crustal information down to the Moho depth. These studies utilise the teleseismic events recorded at broadband stations. Zor *et al.* (2006) investigated in detail the shear velocity structure in the Eastern Marmara region at 5 selected stations (Figure 3.1). Büyükakpınar (2013) used multiple reflections at the Moho and focused only on the variation of Moho Topography for whole Marmara region. A more recent work is the study by Bayrakçı *et al.* (2013) which investigates the 3D velocity of the North Marmara Trough

(NMT) by a tomographic inversion. This work uses data from a comprehensive geophysical survey including both offshore and onshore seismometers (OBS), marine refraction seismic and coincident MCS (marine multichannel reflection) profiles (Becel *et al.*, 2009). However the focus point of this survey is mainly limited to the offshore areas, in particular to the detailed structures of the off-shore basins. The same data set were also the basis of other off shore studies: a detailed P-velocity model of Marmara Sea is developed in order to understand the off-shore structure at crustal even lithospheric scale as seen in Figure 3.2 (Laigle *et al.*, 2008, Becel *et al.*, 2009, Becel *et al.*, 2010). Güvercin (2013) also investigated 3D velocity structure using local earthquake tomography and gives information about both marine and continent parts of the Marmara region.

None of the study described above is suitable to be used directly for our purpose. The main limitation comes from either because their focusing area does not overlap with ours (such as the detailed marine observations by Bayrakçı *et al.*, 2013, Becel *et al.*, 2010 etc.) or they cover a larger area and does not have the resolution required in our application (such as the land based tomographic work of Barış *et al.*, 2005, Güvercin, 2013, etc.). However we make use of these results by selecting relevant information efficiently and combining them to producing a single 3-D structure model that covers only the deep part of metropolitan area of Istanbul.
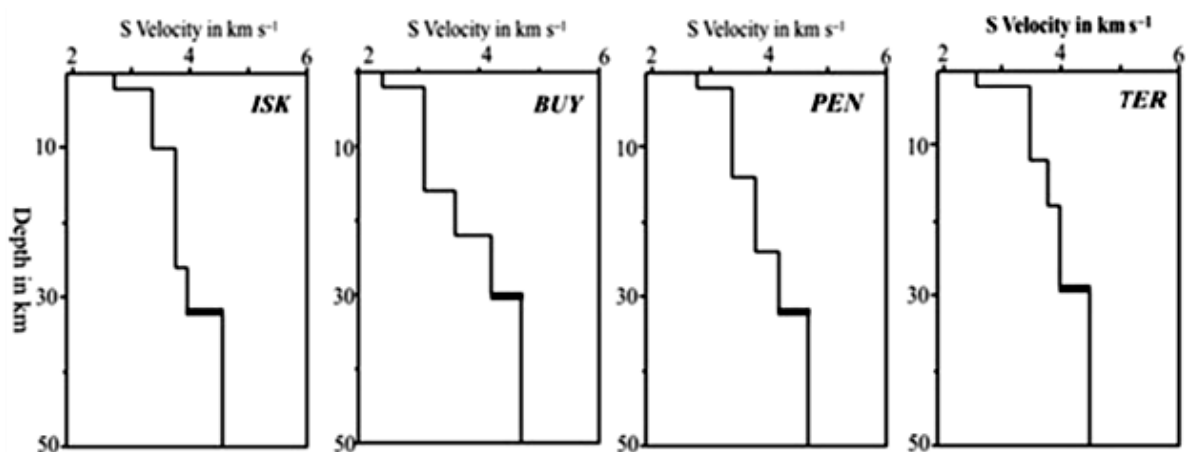
Figure 3.1. 1D S-velocity structure from receiver function study (Zor *et al.*, 2006).
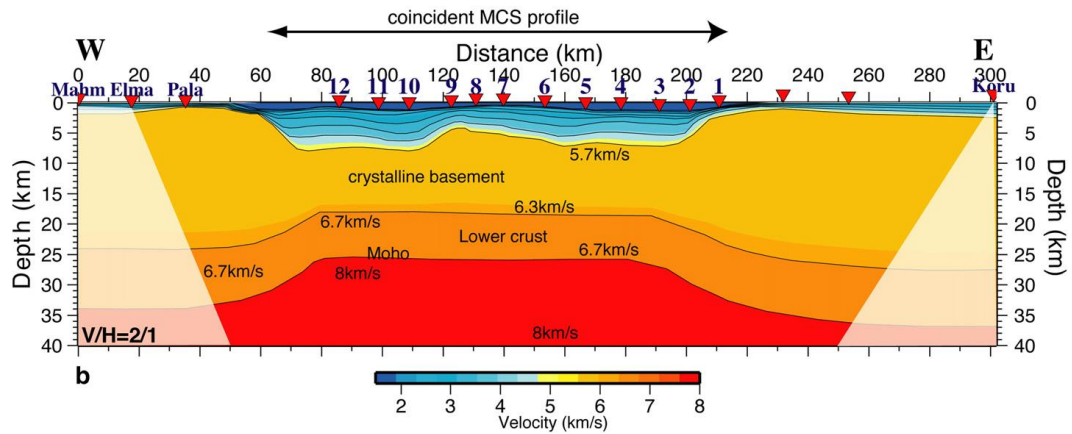
Figure 3.2. Vp structure from wide angle reflection-refraction data (Becel *et al*., 2009).

3.2.2. Shallower Structure

In this thesis, the majority of information for the modeling of shallower part of the study comes from geotechnical and geophysical surveys carried out by İstanbul Municipality during the period of 2006-2009. Seismic profiles, boreholes, suspension P-S velocity (PS Logging) and refraction microtremor (REMI) measurements were performed by İstanbul Municipality, in the context of microzonation Project of Anatolian and European parts of the city. Within the framework of this project, 18 PS Logging measurements with depths varying between 60-240m and 30 REMI measurements down to depths of 1km were implemented on the European side (Figure 3.3). Similarly, 16 PS Logging measurements with depths varying between 80-190m were obtained for the Anatolian side (Figure 3.4). We used these results as the starting point of the modelling for the shallow structures.
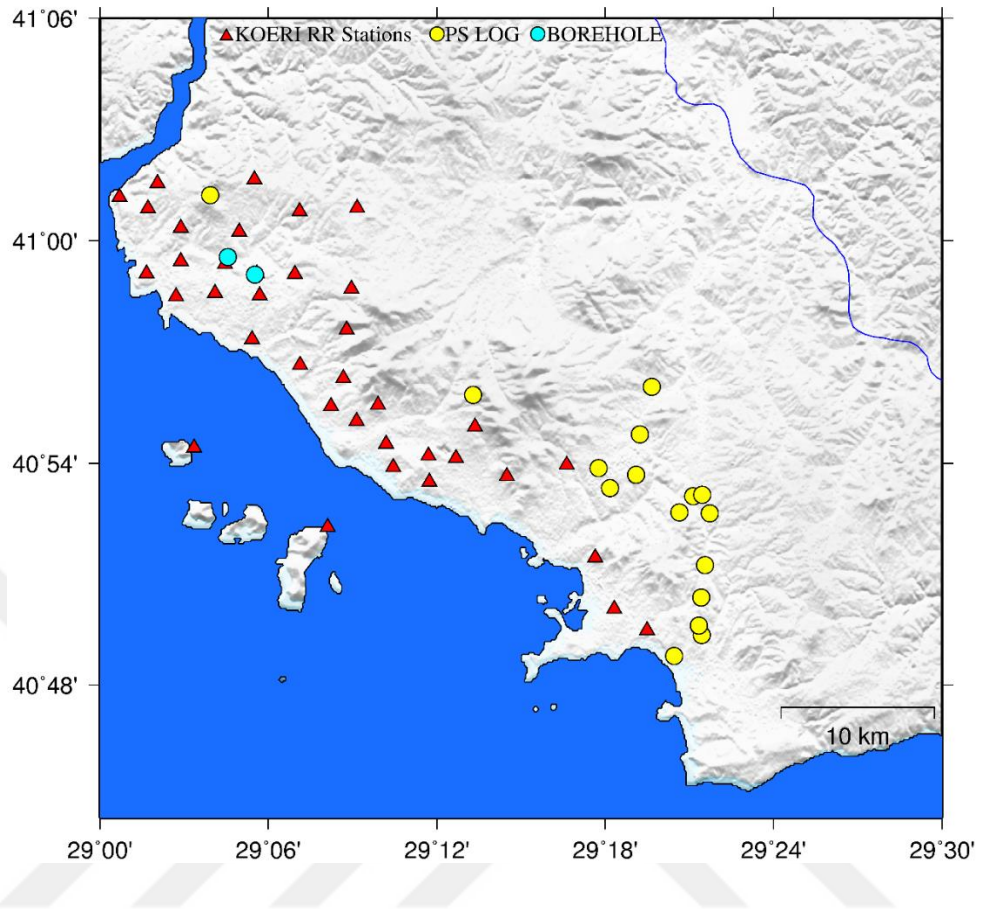
Figure 3.3. Location of measurement points at the Anatolian part.
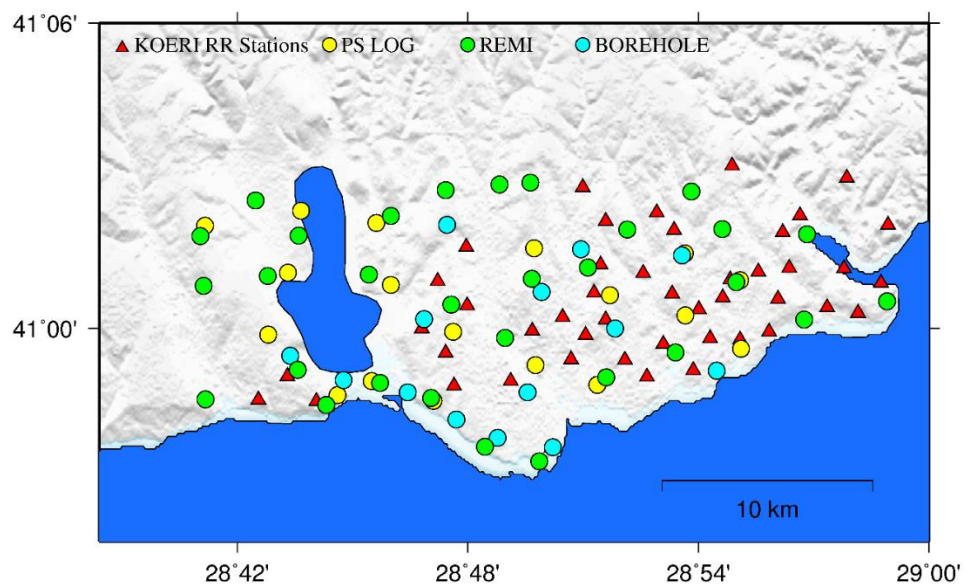
Figure 3.4. Location of measurement points at the European part.

Additionally, the study concerning the mapping of bedrock in the coast south of İstanbul by Birgören *et al.* (2008) was extensively used for increasing the number of reference points around the coastal areas of İstanbul. In that study, experimental transfer functions from microtremor analyses are compared with analytical transfer functions for each site (Figure 3.5). Moreover, one dimensional site response were modelled using Shake91 program (Idriss&Sun, 1992), down to a depth of 500m using data from borehole sites of JICA project and other private companies. Finally, at total of 14 1-D velocity models, covering both European and Anatolian parts, were readily available for our application.
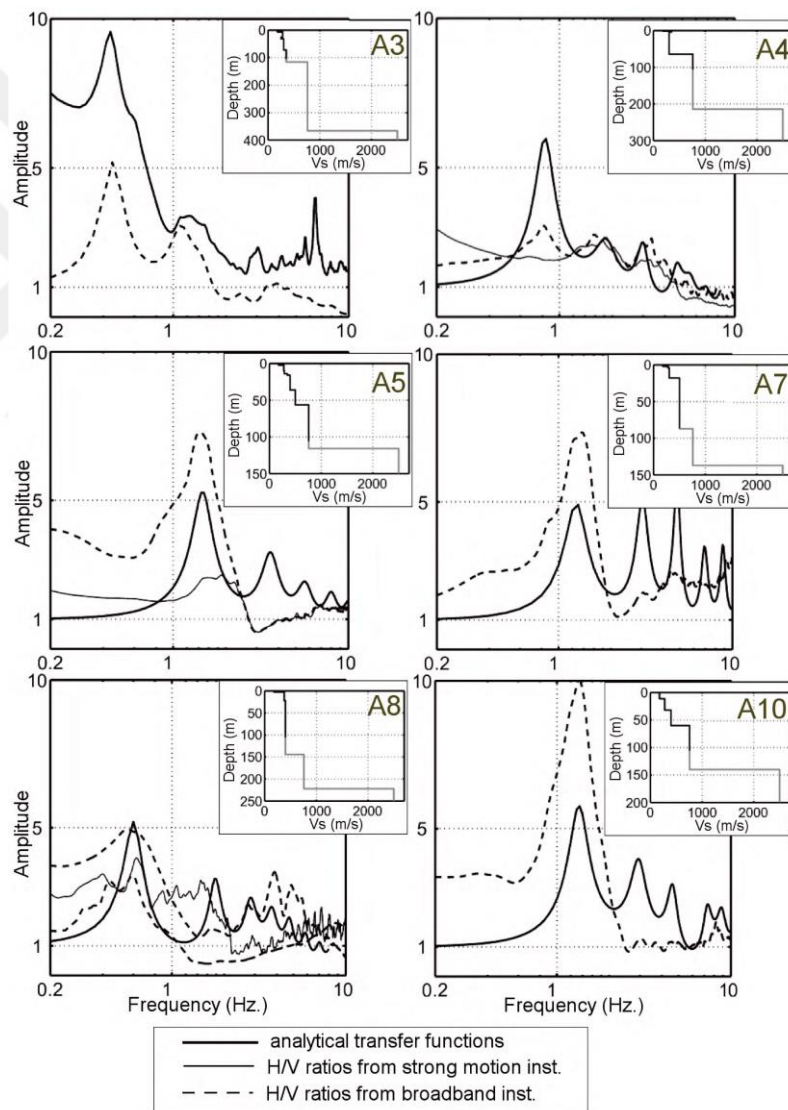
Figure 3.5. Example of additional 1D velocity models which are used in our application from study of Birgören *et al.* (2008).

3.3. Procedure for Constructing 3D Model from 1-D Reference Points

The construction of the 3-D model consists of using efficient interpolation tools to fill in the gaps between a set of reference points obtained from 1D velocity models. In other words everything is built over the 1D data available at the start. We therefore prepare a collection   of reference data points scattered over the study area covering both the deep and the shallow structure of the crust. For the purpose of creating the 3D velocity model, we follow the application steps which are summarized by the flow chart given in Figure 3.6.
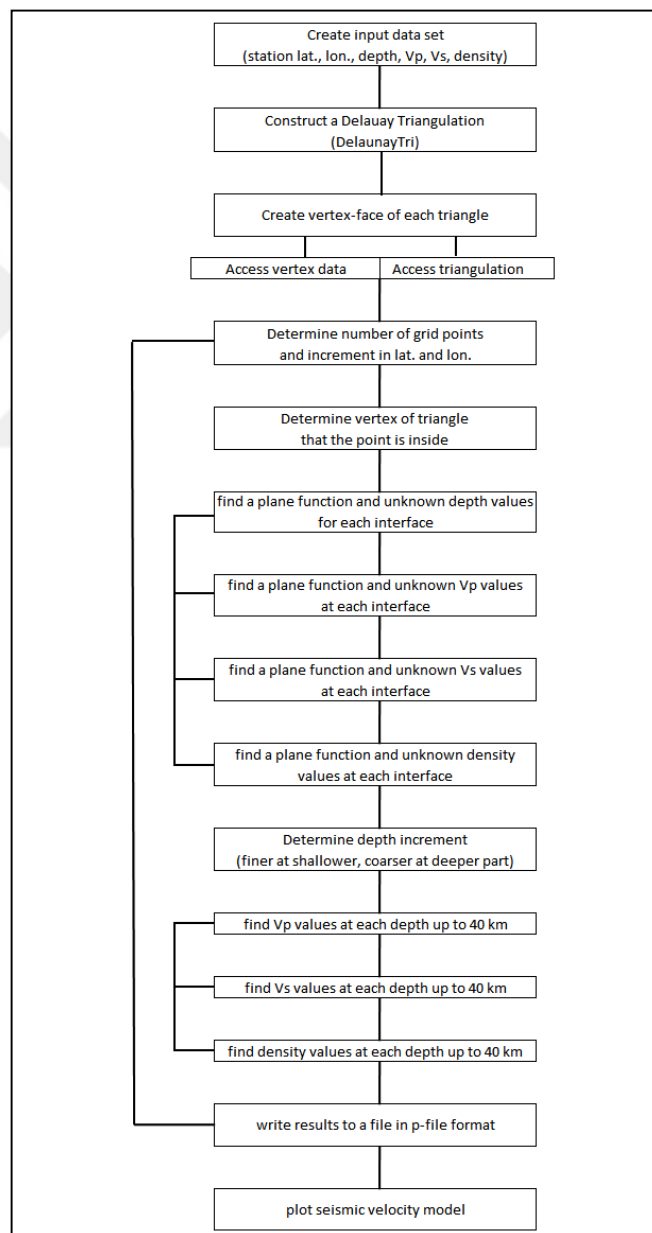
Figure 3.6. Flow chart for creating 3D velocity model.

The first step of constructing 3D velocity model is creating a reference data set which includes all the locations where 1D information is already available. In our case, the reference points are spread over the modeling area in an irregular manner. Every reference point include a certain number of layers, each with a corresponding V_p, V_s and density values. To determine a strategy for connecting these reference points and generating an interpolated volume is the most critical part of the procedure for constructing 3D model. There are different approaches for interpolating scattered data such as linear, nearest neighbor, polynomial, Gaussian and Kriging interpolation. We prefer one widely used approach, which consist of triangular mesh generation by Delaunay triangulation of the reference points (Delaunay, 1934). We first describe Delaunay triangulation method and how it is applied in our problem. Next, we discuss the issue of optimal sampling interval for constructing the 3D model.

3.3.1. Delaunay triangulation

To understand the basic principles of the Delaunay triangulation, we make use of the Voronoi diagram which is a geometrical dual to the Delaunay triangulation (Tsai, 1993). A Voronoi polygon is defined as a polygon. It contains exactly one generating point and every point placed in a given polygon is closer to its generating point than to any other one (Khazai *et al.,* 2008). When forming Voronoi polygon the edges are selected from the orthogonal bisector lines in such a way that any point in a given Voronoi polygon is closer to the generating point of this polygon. (Note: Orthogonal bisector of line segments are loci of points that are equidistant to two reference points). The Delaunay triangles can be formed by connecting generating points of neighboring Voronoi polygons (Figure 3.7a). This guarantees that, in two neighboring triangles, the sum of the angles looking at the common edge never exceeds 180^0. This concept can be better illustrated using a practical example (Figure 3.7b). In practice, two neighboring triangles are defined using 4 points as vertex (say A, B, C and D). Therefore there are only two ways that one can define two triangles: by joining either A and C or B and D, such that AC or BD becomes the common edge. If a situation would arise that one of the angle looking at the common edge exceeds 180^0, then the common edge needs to be flipped to the other option (say AC needs to be flipped to BD or vice versa).
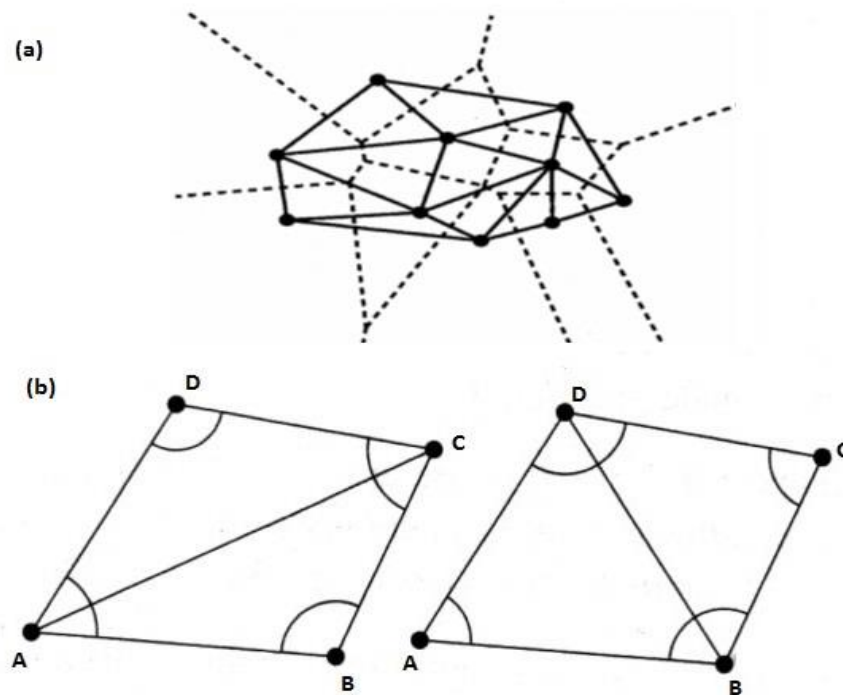
Figure 3.7. (a) Voronoi diagram and Delaunay triangulation (Mcallister and Snoeyink, 2000), (b) generating a Delaunay triangulation by flipping the common edge.

There are numerous algorithms for computing triangulations. Delaunay triangulations are commonly used in scientific computing in a variety of applications due to their helpful properties (Matlab, Mathworks). Below we give a summary of various properties which makes this interpolation method suitable for our purpose:

(i) First one is that the triangulation is independent of the order the points are processed. This comes from the fact that there is always one unique triangulation of the Delaunay type. Therefore whichever path is followed when doing the triangulation the final result should always be same.

(ii) Another fundamental property of this method is that all circumcircles of Delaunay triangles are empty circles (Delaunay, 1934) . In other words they contain no other reference point in their interior. It is also called Delaunay circumcircle criterion (Berg, M., Cheong, O., Kreveld, M. and Overmars M., 2008). This means that when a triangulation is chosen with three points, the next nearest forth point is kept sufficiently away from the triangle so that its influence in minimized. In other words, any property of the area inside the triangle is

determined through interpolation of the vertex of the triangle; all the other points are kept to a significant distance from the triangle. Since all properties of the area in the triangle is determined through interpolation of only the vertex of the triangle, the strategy would be to keep the fourth point as much away as possible. This is suitably achieved by Delaunay method. This property gives a local character to the interpolation, which is opposite if we were using a curve fitting. The example in Figure 3.8 illustrates the validity of this criterion. The figure shows various ways of passing a circle (namely circumcircle) through a given set of 5 points. The figure on the left shows the only case which corresponds to Delaunay triangulation. Only in this situation, all of circumcircles associated with triangles are empty and they do not contain any point in their interior. However, in the central case, the circumcircle associated with ABE, is not empty; it contains point C in its interior. Therefore, this triangulation is not a Delaunay triangulation. Finally in the illustration on the right, the Delaunay triangulation property is not valid once again since the circumcircle contains B and C.
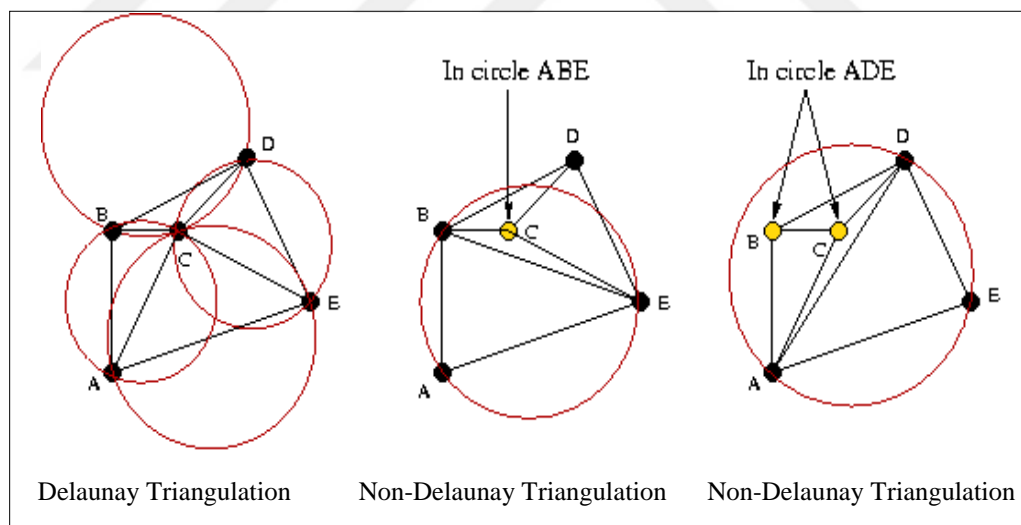
Figure 3.8. Empty circumcircle criterion of Delaunay Triangulation (Matlab, Matworks).

(iii)The other important geometrical property of the method is that triangles are as equi-angular as possible. Thus, Delaunay triangles are defined to be 'well shaped triangles' which means triangles with wide internal angles are preferred over ones with narrow internal angles (Li *et al.,* 2014). This feature helps avoiding long and thin triangles as much as

possible and reducing any numerical precision problems created by these type of triangles. In other words, combination of points which are distant from each other are prevented by this property.

(iv) Another important feature of Delaunay triangles is that they vary in dimension according to the partial data density. They adjust to the data set so that they are small and multiplexed in areas with high sample density, large and lesser in low density areas (Viezzoli *et al.,* 2007). In other words, because reference points are placed irregularly over the modeling region, it has a higher resolution in area that has a higher sampling density and vice versa.

Once the Delaunay Triangulation is chosen as the preferred interpolation method for 3D model creation, the next step is to determine the implementation of procedure. In the application of the method, we used DelaunayTri class algorithm in the light of the criteria mentioned above and made use of a MATLAB tool dedicated for this purpose (Matlab, Mathworks).

At the start, we have a set of N number of reference locations where 1D data is available. Each of these points is represented by its geographical coordinates, leading to an array of 2xN real number. We combine these points in groups of 3 vertices, each defining a Delaunay Triangle. To determine the number of triangles in the triangulation, a rule which is defined as 2N-2-k is applied. Here, N is number of points and k is number of points in convex hull boundary so that outer polygon must be convex hull on triangulation. According to that rule a set of 25 reference points would define 41 triangles, for example.

3.3.2. Optimal Grid Spacing in 3-D velocity modelling

The critical step for constructing 3D model is deciding about the optimal gridding parameters that guarantee the best representation to the region of interest. In our case, we use a nearly uniform grid spacing in the horizontal and nonuniform grid spacing is in the vertical direction. Horizontally, a dense grid of points is created by choosing a grid spacing of 0.005 degree both in latitude and longitude. This corresponds to a horizontal array of 160x88 grid points. In the vertical direction we have chosen to have a finer depth increment

at the shallower part which has lower velocities and coarser sampling at the deeper part. This corresponds to keep a more or less similar number of sample points for a given wavelength. This approach increases the computational efficiency by making use of the mesh refinement procedure available in the WPP software. In our case (for modelling deeper structure) non irregular sampling of the vertical direction is as follows: is 1 km for first 8km, 2km in between 8km and 20km, 4km from 20 km up to 40 km.

Applying the procedure for constructing 3D model which is summarized in Figure 3.6 for the area of interest (60x40km) we obtain a total of 2.3×10^8 grid point. Attributing 3 distinct material properties at each grid point, namely P velocity, S velocity, and density, we obtain a final 3D model, expressed as an asci file of 15MB. The format of this file is well-fined and is called P-file, which description is given in the WPP package. This file can be used directly as input for the WPP package. The package internally reprocess the structure to make it more suitable for finite difference computations.

3.4. Final Results for the 3-D structure

3.4.1. Deeper Structure

Receiver function studies provided the main information source for modeling the deeper parts of the study area, on the land side (Zor *et al.,* 2006). We have used five-layered 1D S velocity structure and V_p/V_s ratio for stations (ISK, BUY, PEN, TER, KAL) located in the eastern Marmara Region (Figure 3.1). P velocities are derived from V_s velocities using the inferred V_p/V_s ratio for the structure corresponding to each of these stations. Note that our study extends beyond the area covered by the polygon created by stations ISK, BUY, PEN, TER. We therefore introduce additional stations where deep structure are obtained not directly from the receiver functions but indirectly from other data sources. In particular we made use of the tomographic studies by Becel *et al.* (2009) for the locations which are offshore. For this purpose, synthetic stations were added to complete the triangulation of our study area. Basically two family of additional structures were used: offshore and onshore structures.

Typically two different types of structures were used for the offshore locations, one to represent the shallow margin close to the coastline (stations Mx) and the other for the deep basin floor of the Çınarcık Basin (stations Bx) (Figure 3.9). To assign the structural values to stations on the margins, we make use of the closest observations of offshore (Bayrakçı *et al.*, 2013) for M1 and M2 stations. We used 1D models beneath the OBS24 station which was on a basement high on the northern border of NMT (Bayrakçı *et al.,* 2013). M4 and M5 were approximated by BUY receiver function model (Zor *et al.,* 2006). Finally station M3 was modelled as a combination of BUY and OBS24 stations. P and S velocities for the basin floor of the Marmara Sea were determined making use of the results of a deep seismic survey in the Marmara Sea investigates the Moho, whole crustal architecture and deep basins (Laigle *et al.,* 2008, Becel *et al.,* 2009, Becel *et al.,* 2010) as figured out in Figure 3.2. The deep velocity structure at stations which were located on Çınarcık Basin (represented by Bx) were taken directly from the velocity profiles given by Becel *et al*. (2009). In this line, five layered 1D models were generated for Bx stations corresponding OBS locations on the E-W profile across the North Marmara Trough. Note that as far as the wave propagation on the metropolitan area is concerned the detailed knowledge of the velocity structure below Çınarcık Basin is not critically relevant.
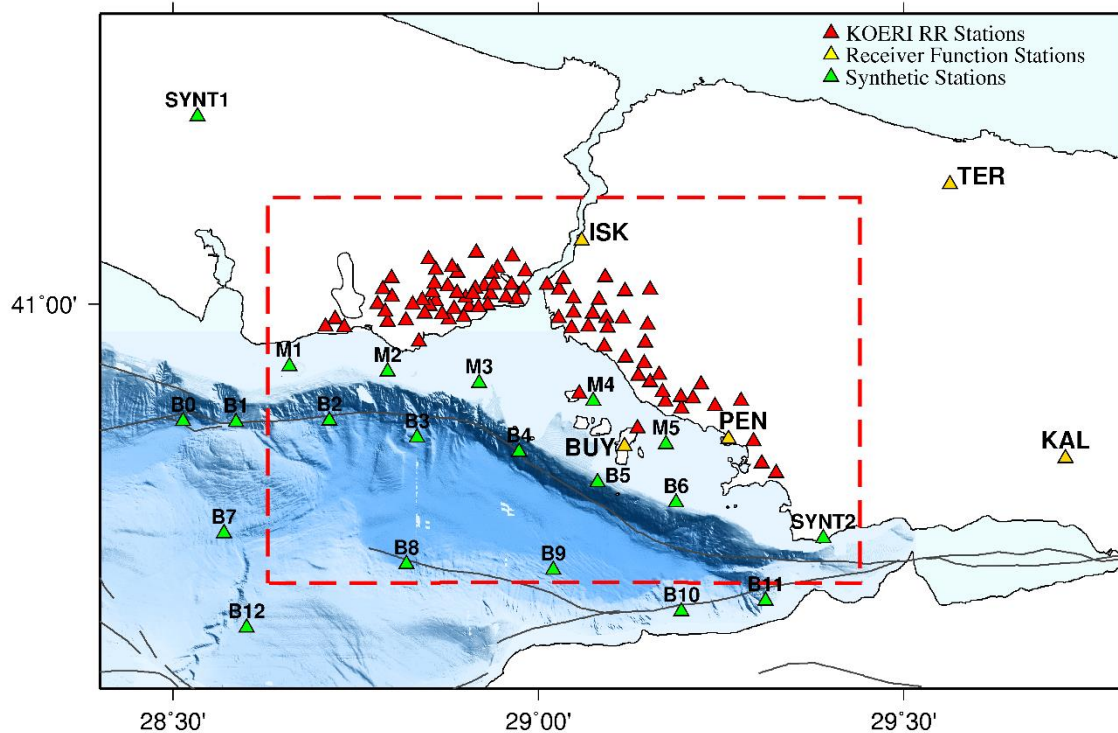
Figure 3.9. Map of study area showing the location of data points.

The two stations located onshore, namely SYNT1 and SYNT2, were modelled using the 1D P and S modelling at CTT station (Gürbüz *et al.,* 1992) and the receiver function at PEN station respectively. The number of 1D velocity structures to be used in developing the 3D model is 25 in total and S velocity- depth variation of these five layered 1D models are presented in Figure 3.10.
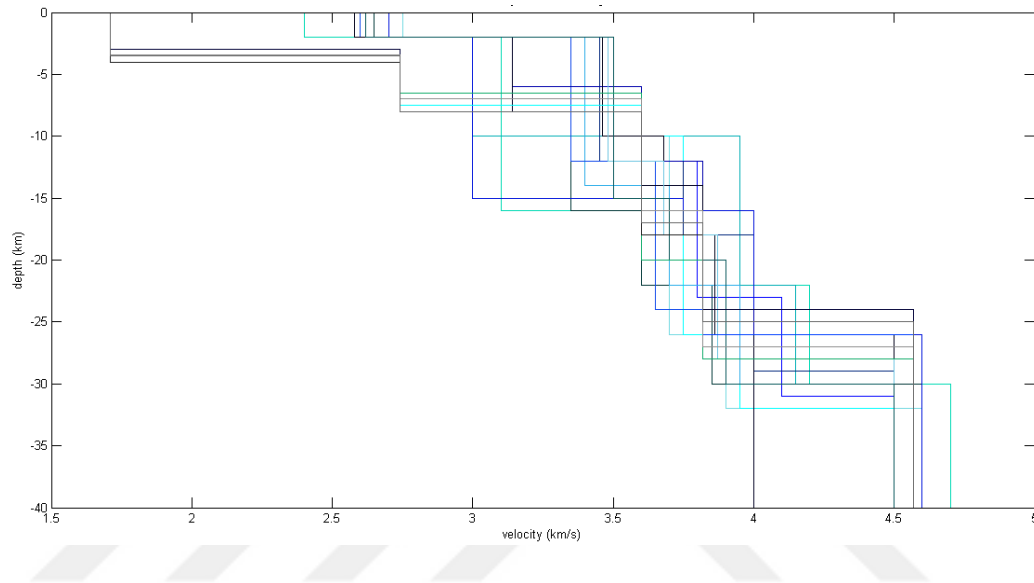
Figure 3.10. 1-D S velocity models for whole region.

Also, distribution of (x,y) data as a scatter plot and the Delaunay triangulation from this data set are presented in Figure 3.11. Note that here, number of triangles and vertices of each triangle are defined namely, Tx and Vx, respectively. 25 reference points we used in our study creates 41 triangles with respect to their location and also followed Delaunay triangulation criteria.
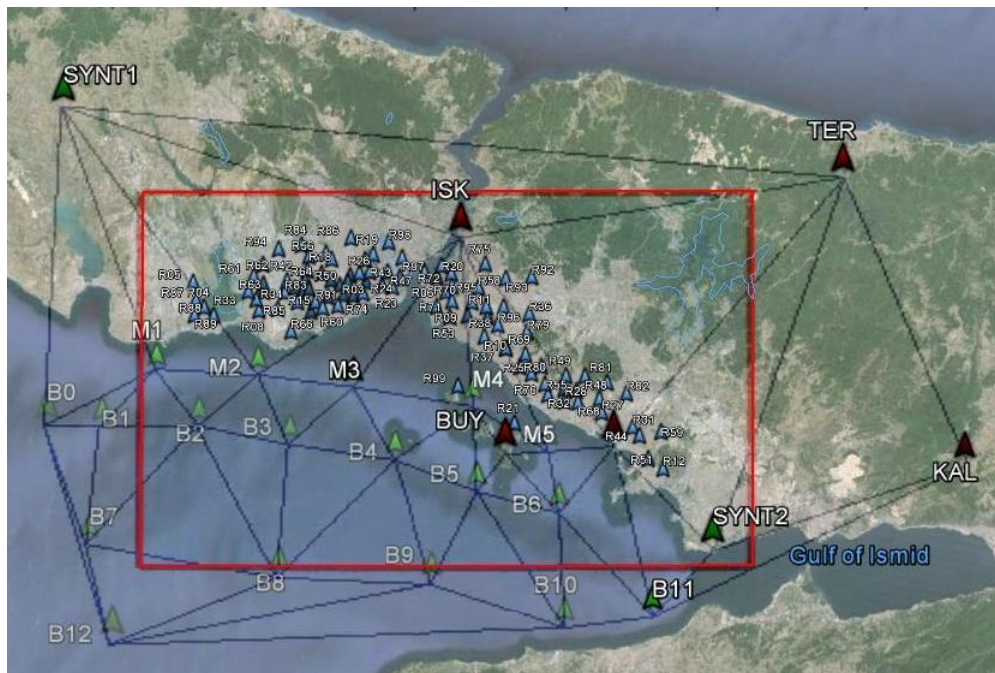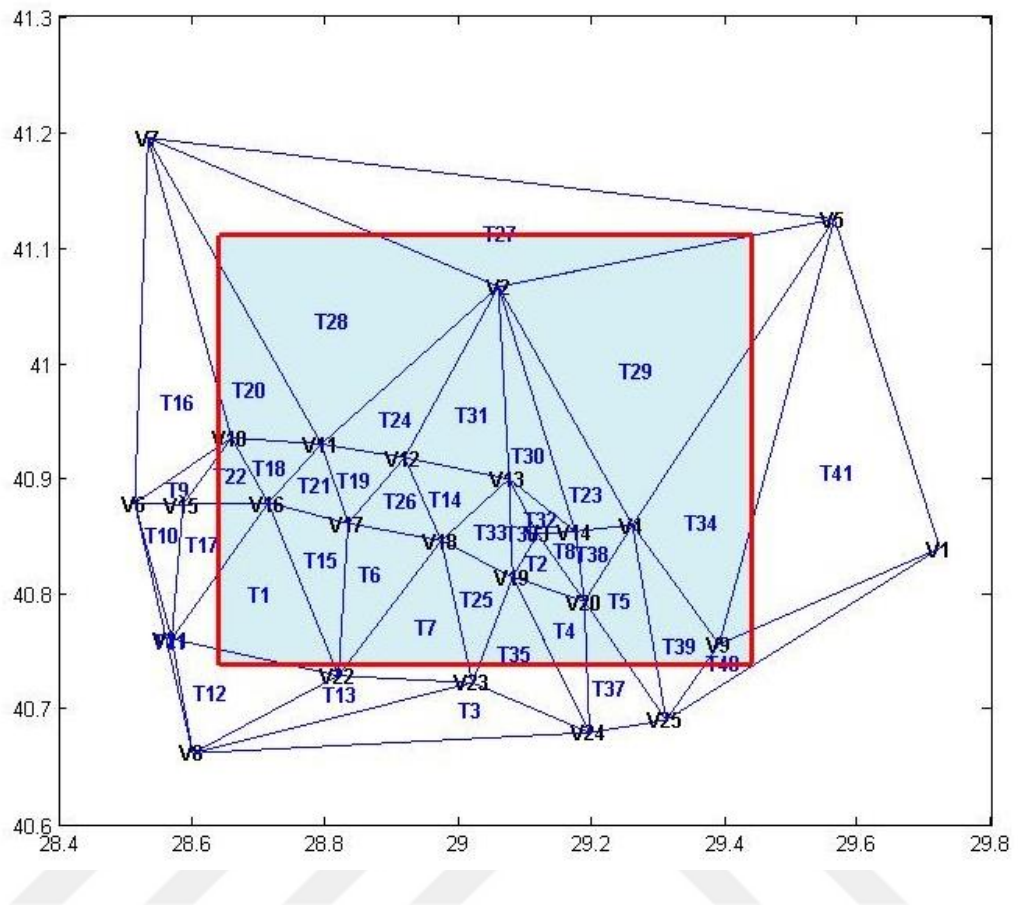
Figure 3.11. Delaunay triangulation with vertex-face format (top), with locations of rapid response stations (bottom). Red square also shows modelling region**.**

3.4.2. Shallower Structure

At the second stage of the modeling process, velocity structure is based on the identification and interpretation of complex geometry defined by mainly the V_p, V_s velocities and densities of the shallow structure. Studies based on PS logging and REMI provided the main information source for modeling the shallower parts of the study area. Both data set include different number of layers for borehole and REMI locations. Our first goal is to express all different measurements using a single format consistent with each other in terms of number of layer as well interpolation methodology. For the purpose of getting fixed number of layer, we calculated total travel time by considering the velocity and the thickness of each layer for each location. And then, we decreased the total number of layers to four layers at each location by keeping the total travel time constant. Resultant measurements obtained using this approach are represented in the graphics given in Figure 3.12.
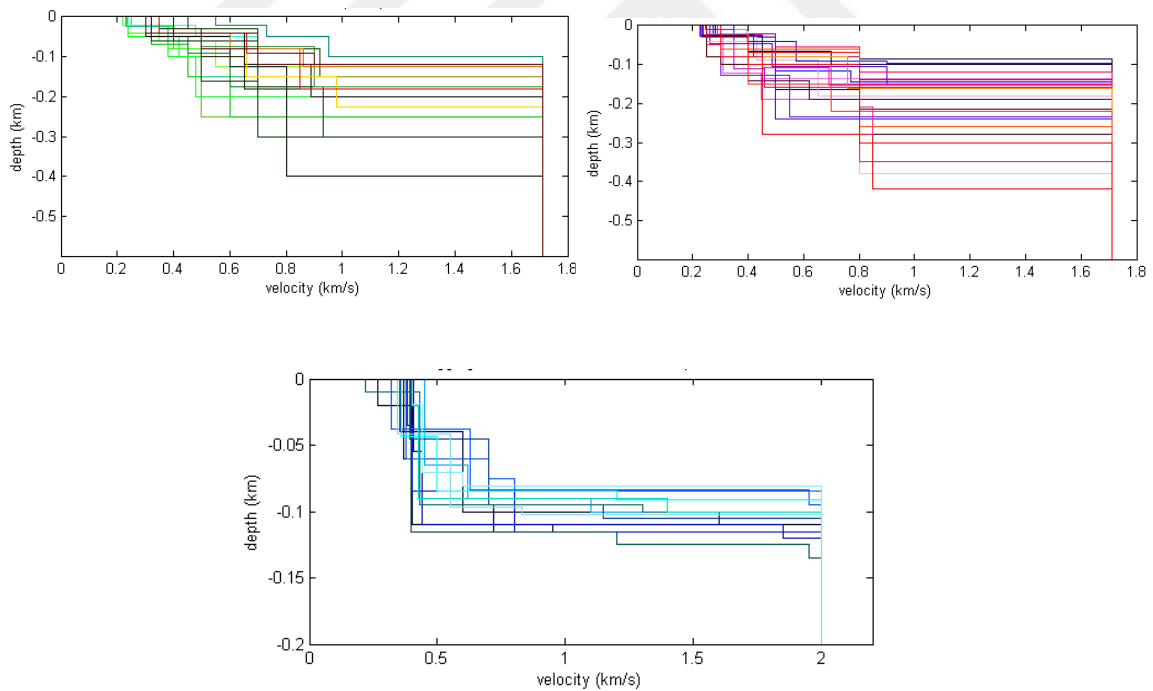
Figure 3.12. 1-D S velocity models from PS Logging (upper left) and REMI (upper right) measurements for European part. 1-D S velocity models from PS Logging measurements for Anatolian part (bottom).

Similar to the case of deeper structure, we added some additional synthetic reference points for various practical reasons. These are summarize below:

Note that our modelling region extends beyond the area covered by the polygon created by REMI and PS logging stations. Therefore, we added four synthetic stations to complete the triangulation of our study area (A1, A2, A3 and A4).

We added points S1-S6 (west of Golden Horn), S7 (Salacak) and S8 (Moda) in order to represent the hard rock sites that are well known to exist at these particular locations. We also added additional reference points to represent the marine part which are not represented by any local study. These are two types: those representing the self (V_p =1.5km/s down to 300m) and the other representing the floor of Cınarcık basin (V_p =1.5km/s down to 1000m).

For the Anatolian part, we have observed that the real data collected from rapid response records shows hard rock conditions for nearly all of the sites. It is clear that soft soil conditions exist in Anatolian part but they are restricted only into narrow zones such as Kurbağalıdere river bed or Maltepe shoreline. Such small scale features are too small to be taken into account in our 3D model. Therefore we assume that hard rock conditions are valid for most of the Anatolian part, and these are represented by the synthetic reference points, hard1 (Çayırova), hard2 (Tuzla) and hard3 (Burgaz Ada). As a result, distribution of (x,y) data as a scatter plot and the Delaunay triangles we created from this data set are presented in Figure 3.13.

Same interpolation methodology (triangulation and resampling) was applied and same application steps were followed to create 3D model from several 1D models for the shallower part. This procedure is illustrated in Figure 3.6. The only difference from the deeper part is the depth constraints shown in Table 3.1 and therefore finer depth increments comparing with deeper part of the structure. In consequence of building velocity structure of shallower part over the deeper part, we developed general 3D velocity model for the study area.
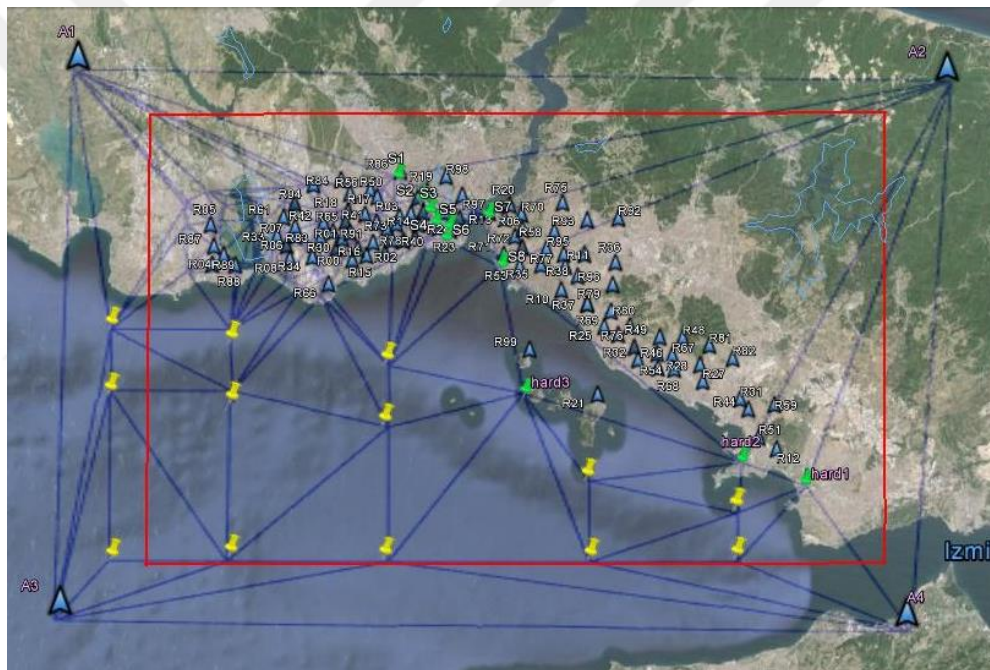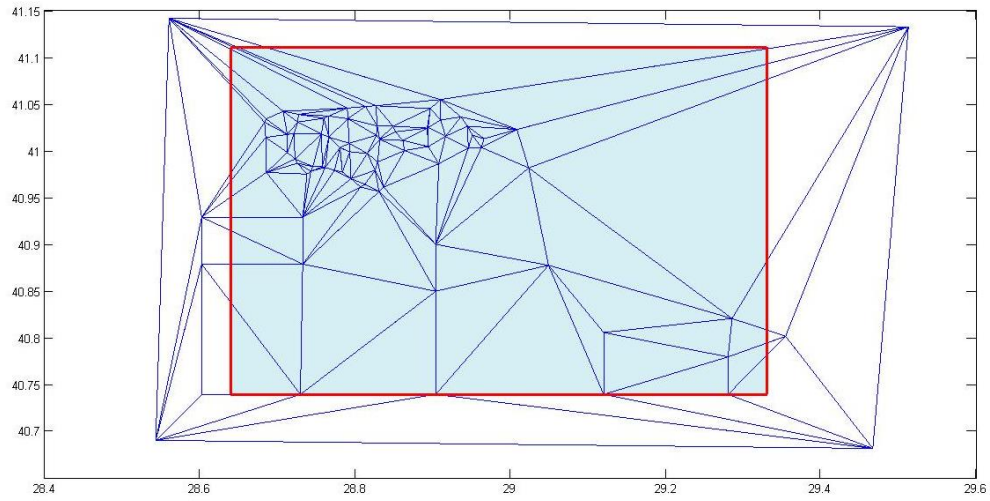
Figure 3.13. Delaunay triangulation with vertex-face format (top), with locations of rapid response stations (bottom). Red square also shows modelling region.

Table 3.1. Depth constraints of application steps

Sampling interval	Depth Range
10m	0-40m
20m	40-120m
40m	120-280m
80m	280-920m

3.4.3. Investigation of constructing 3D model using N-S Profiles

The final 3-D velocity structure using the method described above is analysed using NS cross sections shown in Figure 3.15 and 3.16. We have used two scales to illustrate the velocity variation in detail: the deep scale and the shallow scale. Color coding is used to indicate the velocity variation across the cross sections. Location of NS cross sections are presented in Figure 3.14.
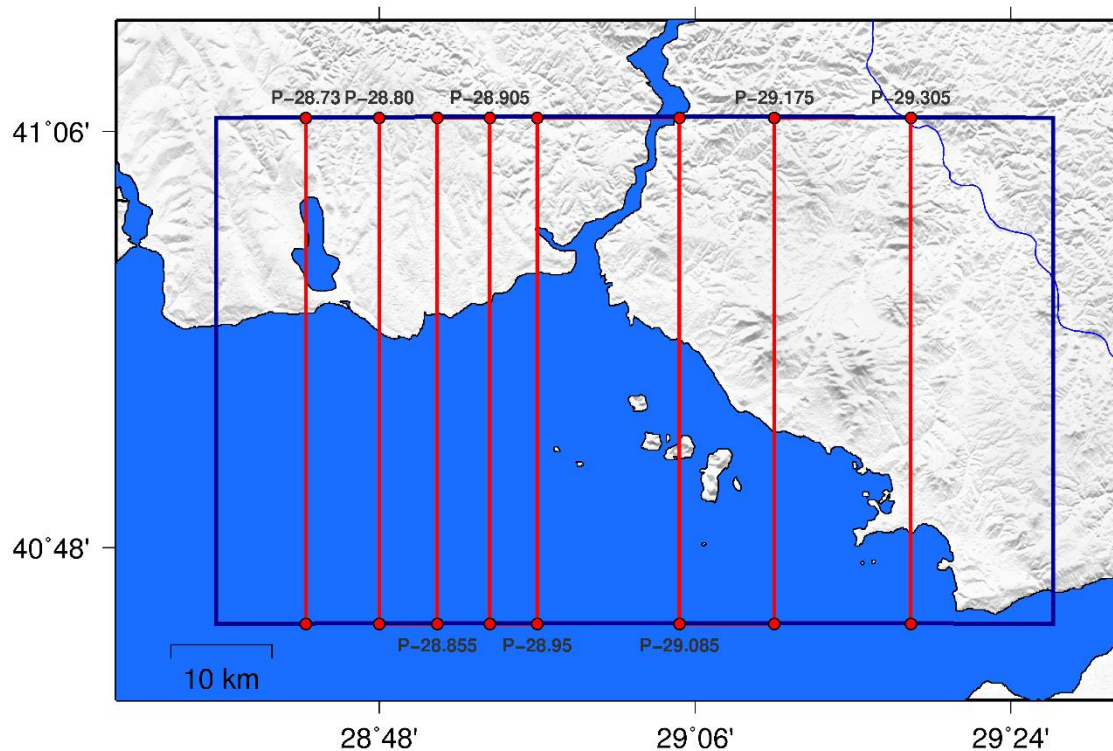
Figure 3.14. Location of the cross sections across the study area.

Figure 3.15 shows the deep scale which includes the entire crust from 0-40 km. The first 5 images in this figure represent cross sections which cut through the European side of Istanbul. The last three images show the profiles through the Anatolian part of the İstanbul, with Profile-29.085 representing the cross section cutting through the Heybeli Ada (Princes Islands). We observe that the main feature of the deep scale velocity variation is the layers with relatively low velocity below the Çınarcık basin. The layer velocities corresponding to the sedimentary basin fill varies between 3.5 and 4.0km/s and reach a depth of about 6 km.

This structural characteristic is observed at all profiles except for the last section in Figure 3.15 which crosses the Tuzla Peninsula, where the effect of Çınarcık Basin disappears. It should be underlined that the effect of this marine basin is felt down to a depth of 5-6 km in locations where the sea bottom level goes down to about 1300m depth.

The other characteristic observed trough the profiles is the slow variation of the Moho topography both in NS and EW directions. The Moho depth is shallower offshore beneath the Çınarcik Basin pointing to a thinner crust in the Marmara NS extension zone (Becel *et al.,* 2009). The Moho depth variation in the EW direction onshore is less significant, showing 25 km depth under European part and reaching 28-30km depth beneath the Anatolian part. Comparison of the deep structure of the inland and the margin slopes does not show much difference. There is only a slow variation due to slight differences that exist among the receiver function at various stations.

We note that some of the velocity transition zones show a staircase pattern that does not look natural. These are in fact an artifact of the nonregular grid spacing in the vertical direction. This artifact disappear in the real computation stage where the WPP algorithm resamples and reinterpolate the velocity information to create a new velocity data.

Figure 3.16 shows the details of the first 400 meters of shallow structure obtained from observational data. The critical point to underline here is the very high aspect ratio used in the profile representation (the vertical scaling is 60 times the horizontal scaling). A general inspection of the profiles shows that the European part includes much more low velocity features at shallow depth than the Anatolian counterpart. The first 5 profiles shows various ondulations with amplitudes up to 100 meters with a wavelength of about 1-5 km. The Anatolian part is on the other hand is more compact at the shallow depth. Additionally, 1500 m/s of P velocity which define the presence of marine part is observable. Another characteristic is presence of soft materials which has lower velocities coming from REMI and PS Logging measurements.
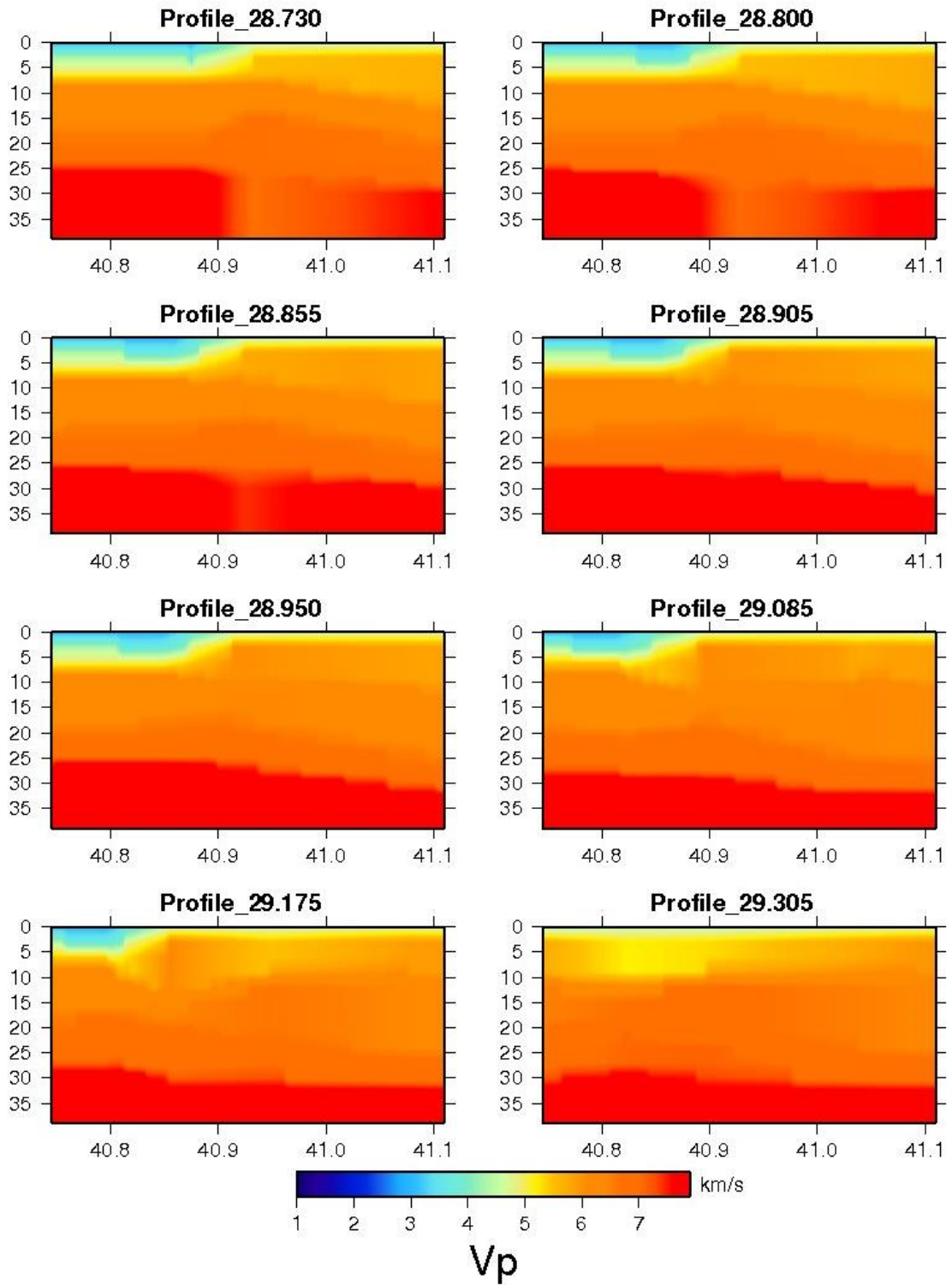
Figure 3.15. Cross sections through the model showing deep crustal structure.

Taking third and fourth images of the Figure 3.16 into consideration; a sudden increase in velocities towards to north is observed due to the presence of more compact materials. We also note that at the easternmost cross section in the European part (Profile 28.95), we observe a local velocity decrease which reflect soft sedimentary fill near Yenikapı. Considering profiles through Anatolian part, low velocities of marine part and hard rock characteristics with increasing velocities to the north are underlined.
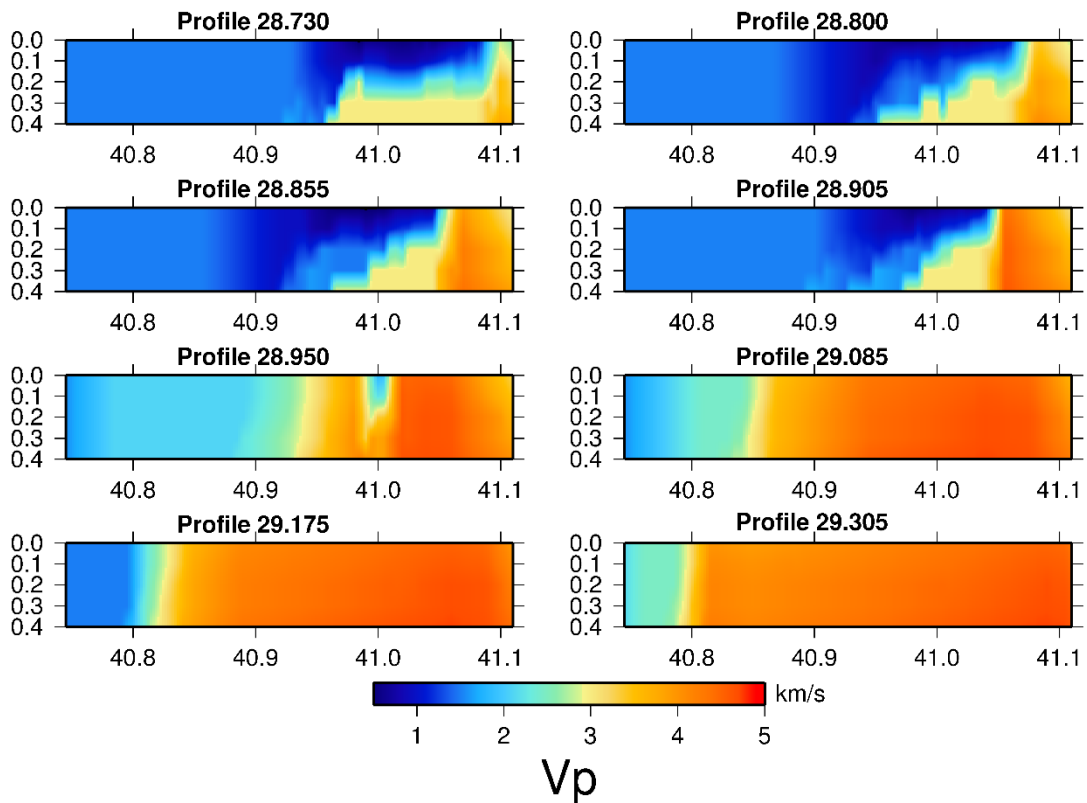
Figure 3.16. Cross sections through the model showing shallow structure.

We have tested the velocity model by generating 3D synthetic seismograms that we have compared with real recorded waveforms of real earthquakes. The overall fitting of model and data was highly satisfactory in a general way. However one cannot expect a full agreement between model and data when one consider that the model is essentially based on the pointwise measurements which are interpolated into a full volume. This issue is discussed in more detailed in the next chapter.

4. WAVE PROPAGATION SIMULATION METHODOLOGY

4.1. Introduction

It is clear that numerical modeling is indispensable tool in seismological research when studying the seismic wave propagation in the Earth's interior. The internal part of the Earth has structurally complex geometry with the interfaces which have different material parameters such as seismic wave velocities, density and attenuation. Therefore, purely analytical approaches are not enough to provide a solution for realistic and complex Earth models. Therefore numerical methods have to be used for modelling the seismic wave propagation and simulate the seismic behavior in the earth.

Moczo *et al.* (2007) indicate that the numerical methods basically transform a differential formulation of any problem into an algebraical equation system in order to be actively performed using computers. Numerical methods differ from each other with respect to how they solve this task and also how they approximate space and time derivatives of the functions. Additionally, accuracy and computational efficiency in the sense of computer memory and time are the other important aspects of the each numerical method (Moczo *et al.,* 2007).

To simulate seismic wave propagation, various numerical methods have been developed among which the finite-difference method (FDM), the finite-element method (FEM), the spectral-element method (SEM), the boundary-element method (BEM) are the most widely known. The examples of different types of numerical models are presented in Figure 4.1. For Finite Element Method, problem region is divided to small sub-areas (or sub-volume), called as element. The advantage of the FEM is to be applicable for models with complex geometries thanks to flexibility of finite element shape and size used in computational domain. FEM satisfies the internal boundary condition, so it does not act each body separately (Shi-Zhe Xu, 2001). However, spatial discretization itself is inadequate because of first and second order polynomials used to expand functions within each element. For 3D problems, increasing of the number of nodes is necessary and a large quantity of computer memory is required in this case (Xu, 2001). Semblat *et al.* (2000a) used high order

finite element method for application of seismic wave propagation. Bao *et al.* (1998) successfully implemented the method to the study of seismic wave propagation in 3-D sedimentary basins.

The Spectral Element Method is a kind of numerical modelling technique which combine the superiority of pseudo spectral and finite element methods (Komatitsch *et al.,* 2005). Therefore, this method is also called as high order finite element method. For that method, model is discretized similar to finite element method. Tromp (2007) stated that the advantage of pseudo spectral method is that computational error exponentially decays with polynomial order. However this method can be applied for models with simple geometries. Therefore, spectral element method uses the flexibility of the finite element method in identification of model geometry. Because spectral techniques uses basis functions such as Chebyshev or Legendre polynomials, these are restricted to smooth media and numerical noise seems in the presence of major interfaces or faults (Tromp, 2007). The spectral element method is first applied on 2D seismic wave propagation problems by Cohen *et al.* (1993) and Priolo *et al.* (1994). It has also been a powerful tool at 3D regional (Komatitsch and Vilotte, 1998; Komatitsch and Tromp, 1999; Komatitsch *et al.,* 2004) and 3D global scales (Chaljub *et. al*; 2003; Chaljub *et al.,* 2004; Komatitsch and Tromp, 2002a, b).

The Boundary Element (BEM) divides only the boundaries of the domain and solves the boundary integral equations (Beskos, 1997; Bonnet, 1999; Sanchez-Sesma, 1995; Xu, 2001; Semblat 2008 and 2000b). Therefore, it lowers the dimensionality of the problem and also the number of equations in the system (Xu, 2001). This situation becomes advantageous for 3D problems. However, BEM has also some drawbacks. It is limited to a finite number of homogeneous regions (Komatitsch and Tromp, 1999) and it is difficult to compound the boundary integral equations related to each homogeneous medium when the region has a complex distribution of physical properties (Xu, 2001).

The Finite Difference is one of the most widely used method in seismology especially for full-waveform modeling by comparison with other numerical tools. This method approximates derivatives by differences between neighbor grid points (Tromp, 2007). This is still dominant method in ground motion modelling due to the fact that it is suitable to apply to complicated models and computationally efficient (Moczo *et al.,* 2004). Moreover, the

method enables parallelization and it is relatively easy to encode. From the historical point of view, wave propagation simulation with the finite difference method was first proposed by Madariaga (1976). Later, improved versions of the method have been widely used over time for full waveform modelling (Virieux, 1986), for 3-D local and regional models (Graves, 1996; Ohminato and Chouet, 1997; Bohlen, 2006) and for smooth and steep topography (Olsen, 2000). Some mathematical books such as Isaacson and Keller (1966), Morton and Mayers (1994), Durran (1999) can be helpful tool for more detailed information of FD method and solving different types of differential equations.
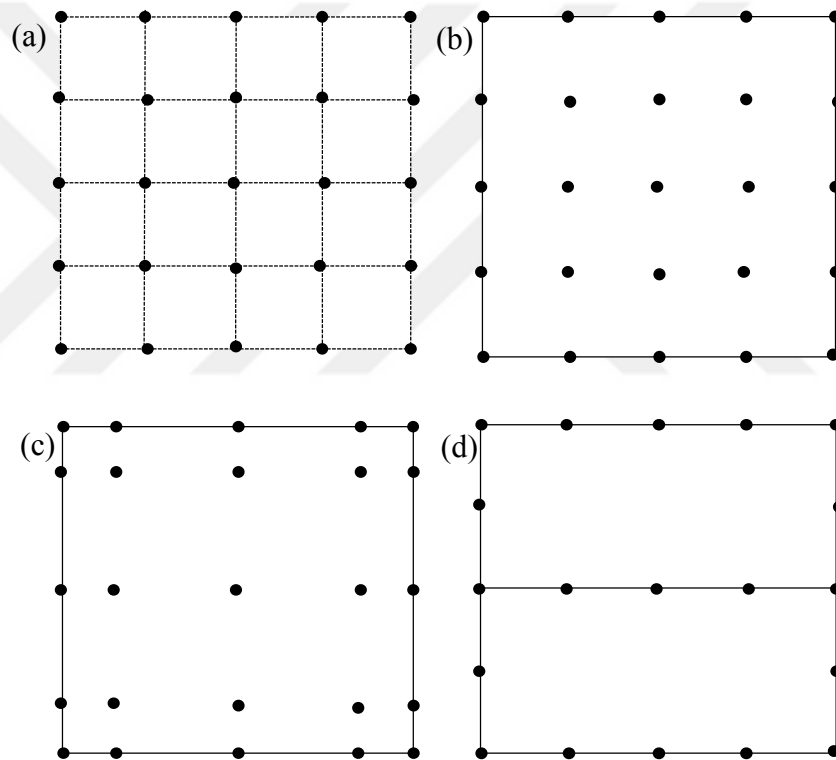
Figure 4.1. Schematic representation of different numerical methods for seismic wave propagation modelling as shown in Semblat (2011) : (a) the Finite Difference Method, (b) the Finite Element Method, (c) the Spectral Element Method, (d) the Boundary Element Method.

The finite difference methods varies in the way they divide the domain into regular grids, the way they formulate the difference equation, the way they handle the boundary conditions, and the way they preserve stability. In our case, we have used a new finite

difference approach which is called Wave Propagation Program (WPP) and developed by a research team (Serpentine Project) at Lawrence Livermore Laboratory. In some ways the method is different from traditional finite difference methods. This code solves the wave equations in second order displacement formulation. A node based finite difference approach which fulfills the summation by parts (SBP) principles is used in the application (https://computation.llnl.gov/project/serpentine/). SBP operator is a kind of FD stencil that generalizes the energy method for bounded domain. Energy method is the approach which guarantees stability of FD by posing non-increasing energy constrain over a volume for a given time. This stable second order accurate technique has substantial capabilities for 3-D seismic modeling. The boundaries are defined as stress-free boundary conditions along the flat free surface on the top, and non-reflecting or absorbing boundary conditions on the three other sides. The source can be defined in two ways: point force and point moment tensor with various types of predefined time dependencies. WPP is also well adapted for parallel processing for the case of a Cartesian grid, with variable wave speeds and density throughout the domain. The parallelization is carried out by using the Message Passing Interface (MPI) library, available in most common operating systems, such as UNİX. In this chapter, the principle of FD method, implementation of the WPP method and basic concepts related to the methodology are presented briefly.

4.2. The Finite Difference Method (FDM)

The application of Finite difference method or seismic wave propagation has been discussed in several sources (Boore, D. M., 1972; Graves, 1996; Kristek and Moczo, 2003; Moczo *et al.,* 2004 and Moczo *et al.,* 2007). However, Moczo *et al.* (2004) and Moczo *et al.* (2007) are referred mainly in this part. Approximation of the partial differential equation by linear combinations of variables at the grid points is the basic principal of finite difference method. The application of the method to a certain differential problem involves some process steps. First one is the construction of a discrete FD model. It includes coverage of the computational area by a space-time grid, the formulation of the equation of motion in terms of the chosen grid type, FD approximations to derivatives, approximation of initial and boundary conditions, setting of the finite difference equations system (Moczo *et al.,* 2007). Next step is the analysis of the FD model which covers certain properties of FD

equations such as consistency, stability and convergence. The last step concerns numerical computations.

In this chapter, I will focus on each of these items separately.

4.2.1. Formulation of the Equation of Motion

When we describe a problem of seismic wave propagation, the equation of motion and Hooke's law which defines the relationship of stress-strain are taken into account together with the initial and boundary conditions (Moczo *et al.*, 2004). At this stage, alternative formulations depending on which field quantity is considered as the unknown variable can be defined. We can obtain four different formulations. They are named in terms of the quantities chosen as the unknown variable, such as displacement vector, particle-velocity vector or stress tensor. These formulations of equation of motion vary with respect to which grid types we will use in FD schemes. These different formulations are given in Moczo *et al.* (2004) as the following.

If equation of motion is kept separately from Hooke's law, ***displacement-stress*** formulation can be referred;

$$\rho \ddot{u}_i = \sigma_{ij,j} + f_i \tag{4.1}$$

$$\sigma_{i,j} = \kappa \varepsilon_{kk} \delta_{i,j} + 2\mu \left(\varepsilon_{ij} - \frac{1}{3} \varepsilon_{kk} \delta_{i,j} \right) \tag{4.2}$$

or

$$\sigma_{ij} = \ddot{u}_i \lambda \varepsilon_{kk} \delta_{ij} + 2\mu \varepsilon_{ij} \tag{4.3}$$

where $\ddot{u}_i$ is second derivative of displacement vector, σ_{ij} is stress tensor, ε_{ij} is strain tensor, f_i is body force, ρ is density, δ_{ij} is Kronecker Delta, λ and μ are Lame constant in a Cartesian coordinate system (x_1, x_2, x_3).

While keeping Hooke's law, the definition of particle velocity is also added and displacement-***velocity-str***ess formulation can be obtained;

$$\rho \dot{v}_i = \sigma_{ij,j} + f_i, \qquad v_i = \dot{u}_i \tag{4.4}$$

$$\sigma_{i,j} = \kappa \varepsilon_{kk} \delta_{ij} + 2\mu \left(\varepsilon_{ij} - \frac{1}{3} \varepsilon_{kk} \delta_{ij} \right) \tag{4.5}$$

or

$$\sigma_{ij} = \lambda \varepsilon_{kk} \delta_{ij} + 2\mu \varepsilon_{ij} \tag{4.6}$$

Instead of adding particle velocity, the time derivative is applied to Hooke's law and the *velocity-stress* formulation can be obtained as follows:

$$\rho \dot{v}_i = \sigma_{ij,j} + f_i \tag{4.7}$$

$$\dot{\sigma}_{ij} = \kappa \dot{\varepsilon}_{kk} \delta_{ij} + 2\mu \left(\dot{\varepsilon}_{ij} - \frac{1}{3} \dot{\varepsilon}_{kk} \delta_{ij} \right) \tag{4.8}$$

or

$$\dot{\sigma}_{ij} = \lambda \dot{\varepsilon}_{kk} \delta_{ij} + 2\mu \dot{\varepsilon}_{ij} \tag{4.9}$$

If stress tensor components are eliminated by placing Hooke's law into the equation of motion, the *displacement* formulation can be obtained. Displacement formulation is another alternative that the only formulation with second spatial derivatives.

$$\rho \ddot{u}_i = \left[\left(\kappa - \frac{2}{3} \mu \right) u_{k,k} \right]_{,i} + \left(\mu u_{i,j} \right)_{,j} + \left(\mu u_{j,i} \right)_{,j} + f_i \tag{4.10}$$

or

$$\rho \ddot{u}_i = \left[\lambda u_{k,k} \right]_{,i} + \left(\mu u_{i,j} \right)_{,j} + \left(\mu u_{j,i} \right)_{,j} + f_i \tag{4.11}$$

The strain tensor,

$$\varepsilon_{ij} = \frac{1}{2} \left(u_{i,j} + u_{j,i} \right) \tag{4.12}$$

and its time derivative,

$$\dot{\varepsilon}_{ij} = \frac{1}{2} \left(v_{i,j} + v_{j,i} \right) \tag{4.13}$$

were used for all formulations except the last one (displacement formulation).

4.2.2. Space-time Grids

Before definition of the grid types that are used in finite difference method, it will be helpful to address some basic concept. Let take in consideration a cartesian coordinate system (x, y, z) and computation area in four-dimensional variables with time, t. In this case, a set of discrete space-time points, (x_I, y_J, z_K, t_m) are defined by Moczo *et al.* (2007) as follows:

$$
\begin{aligned}
x_I &= x_0 + I\Delta x, \\
y_J &= y_0 + J\Delta y, \\
z_K &= z_0 + K\Delta z, \\
t_m &= t_0 + m\Delta t,
\end{aligned}
\tag{4.14}
$$

Here, *I, J, K, m* describe a space-time grid. $\Delta x, \Delta y$ and Δz are called grid spacing and Δt is the time step. The value of a function u at a grid point (x_I, y_J, z_K, t_m), that is *u(I, J, K, m),* is approximated by a grid function $U_{I,J,K}^m = U(x_I, y_J, z_K, t_m)$.

According to Moczo *et al.* (2007), the preference of grid type specify the structure and characteristics of FD approximations to derivatives and also the properties of the FD equations. The regular or uniform grid with grid spacing $\Delta x = \Delta y = \Delta z = h$ is a reasonable choice generally. Conventional and staggered grids are two essential types of regular rectangular grids. A conventional grid uses displacement formulations and in this case all functions are approximated at the same grid positions (Moczo *et al.,* 2007). Here, all displacement components are located and all material parameters are identified at each grid point. This technique is first applied for modelling seismic wave propagation by Alterman and Karal (1968), Kelly *et al.* (1976). However, conventional grid FD shemes have some problems such as instability and grid dispersion in media in case of high Poisson's ratio (Moczo *et al.,* 2004).

Displacement-stress and velocity-stress formulations are used in a staggered grid, as the most preferred FD grid type. In staggered grid, different displacement/particle-velocity and stress-tensor components and also material parameters are identified in varied grid

positions (Moczo *et al.*, 2001). Madariaga (1976) proposed a velocity-stress finite-difference method on a staggered grid. The scheme was adapted for the SH and P-SV wave modelling by Virieux (1984, 1986). Bayliss *et al.* (1986) and Levander (1988) also presented 4th order staggered grid FD. This method has been used in 3D seismic wave propagation modelling by Olsen and Schuster (1992), Graves (1993), Yomogida and Etgen (1993). Although staggered grid technique has been very popular, it is limited to box shaped geometries and also sometimes goes unstable when material properties vary rapidly on the grid. The so-called grid cells of regular rectangular grids are illustrated in Figure 4.2.
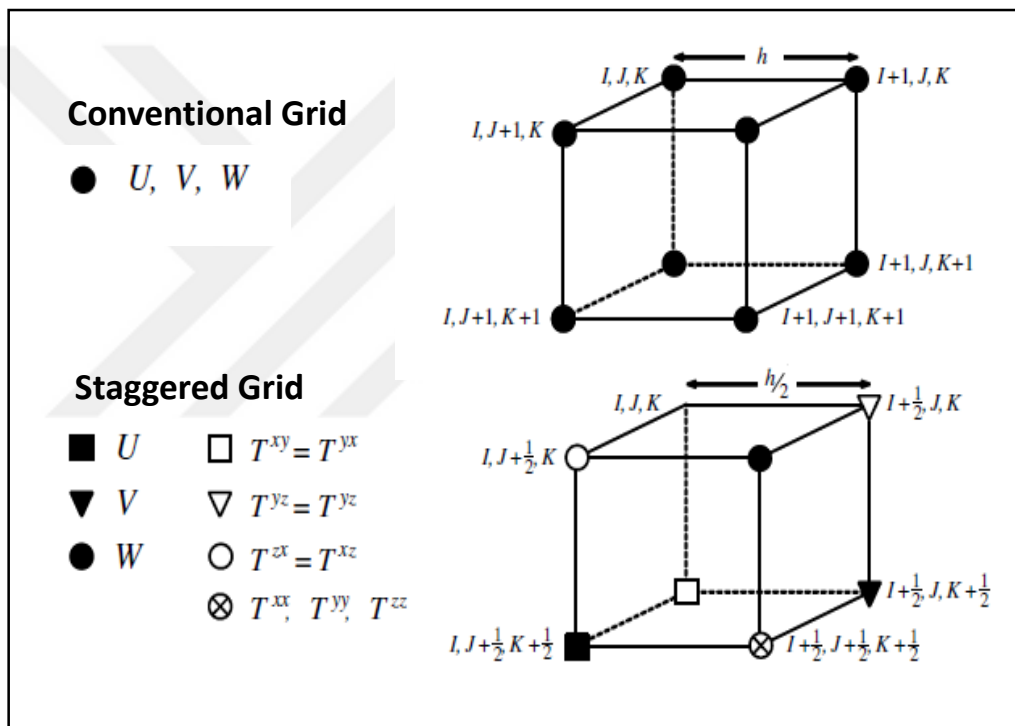
Figure 4.2. Spatial grid cells in conventional and staggered grids as shown in Moczo *et al.* (2007). In conventional grid (top) all displacement vectors U, V, W, are placed at each grid point. In staggered grid, (bottom), displacement and/or particle velocity components U, V, W are located at different grid points. Shear stress tensors T^{xy}, T^{yz}, T^{zx} have their own grid position whereas normal stress tensors T^{xx}, T^{yy}, T^{zz} all share one grid position.

The regular rectangular type of grid yields algorithmically the simplest FD schemes. But, this can be disadvantageous in terms of computational efficiency. Instead of this, combined or composite grids which are defined as irregularly varied grid spacing size with

an abrupt change in the size of the grid spacing (Moczo *et al.,* 2007). This can be a better choice for reducing total number of grid points in computational space. This type of grid was first used by Boore (1970). A significant progress was performed in advancing years by Moczo (1989) and (1993), Pitarka (1999). In combined grid, varying grid spacing as coarser and finer grid is adopted to computational domain. In other words, one part of the computational domain is solved using lesser time step while the other part is solved by greater time step (Moczo *et al.,* 2004). More complex cases of modeling by the velocity-stress finite difference scheme on a combined rectangular grid are introduced by Jastram & Tessmer (1994) and Falk *et al.* (1996). Kang and Baag (2004a, b) developed an efficient FD scheme where larger time step is used in coarser grid and smaller one in finer grid (Moczo *et al.,* 2004). In that approach, a finer grid covers a rectangular region which includes the free surface. Therefore, it makes that approach more efficient for modelling localized soft materials such as the sedimentary basins.

4.2.3. Finite Difference Approximations to derivatives

Partial differential equations involve derivatives which physically represents the ratio of change of a physical quantity represented by a function.

In 1D case: $\Omega = (0, X)$, $u_i \approx u(x_i)$, $i = 0, 1, \dots\dots N$

Here, grid points and grid spacing are stated as;

$x_i = i\Delta x$ and $\Delta x = {X}/{N}$, respectively.
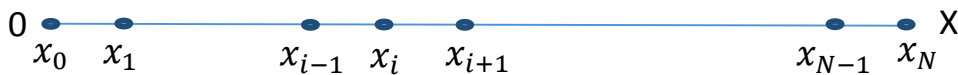
$$\frac{du(x)}{dx} = \lim_{\Delta x \to 0} \frac{\Delta u}{\Delta x} \approx \frac{\Delta u}{\Delta x} \qquad (4.15)$$

This equation depicts the principle of finite difference approximation. Figure 4.3 shows the function $u(x)$ and basic finite difference shemes graphically.
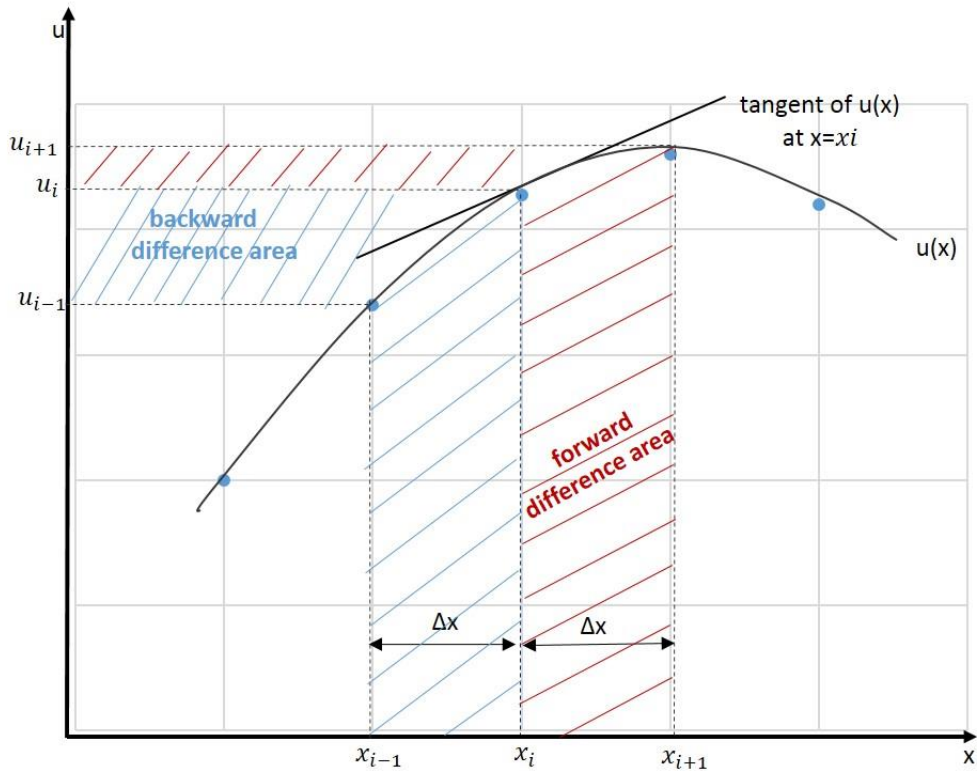
Figure 4.3. Geometric interpretation of the basic finite difference schemes.

The value of a function at a given point x (*u(x)),* can be expressed by the value of the function at a point x_i and the derivatives at the same point, using the Taylor expansion:

$$u(x) = \sum_{n=0}^{\infty} \frac{(x - x_i)^n}{n!} \left(\frac{\partial^n u}{\partial x^n}\right)_i \tag{4.16}$$

Assuming that the function is expressed at the grid point as $u(x + \Delta x)$ and $u(x - \Delta x)$, for forward and backward steps, with Δx as the grid spacing. Expressing with indexes in discrete notation as u_{i+1} and u_{i-1}, the Taylor expansion can be written as:

$$u_{i+1} = u_i + \Delta x \left(\frac{\partial u}{\partial x}\right)_i + \frac{(\Delta x)^2}{2!}\left(\frac{\partial^2 u}{\partial x^2}\right)_i + \frac{(\Delta x)^3}{3!}\left(\frac{\partial^3 u}{\partial x^3}\right)_i + \frac{(\Delta x)^4}{4!}\left(\frac{\partial^4 u}{\partial x^4}\right)_i + \cdots \tag{4.17}$$

$$u_{i-1} = u_i - \Delta x \left(\frac{\partial u}{\partial x}\right)_i + \frac{(\Delta x)^2}{2!}\left(\frac{\partial^2 u}{\partial x^2}\right)_i - \frac{(\Delta x)^3}{3!}\left(\frac{\partial^3 u}{\partial x^3}\right)_i + \frac{(\Delta x)^4}{4!}\left(\frac{\partial^4 u}{\partial x^4}\right)_i + \cdots \tag{4.18}$$

At this stage, we see that there are three different ways for defining the partial derivatives. First one can be obtained from eq. (4.17), second one from eq. (4.18) and the third one by subtracting one from the other. The consequent formulas namely forward difference, backward difference and central difference formulas are obtained, as shown in Moczo *et al.* (2007) with following three expression (4.19-4.21);

$$\left(\frac{\partial u}{\partial x}\right)_i = \frac{u_{i+1} - u_i}{h} + \mathcal{O}(h) \tag{4.19}$$

$$\left(\frac{\partial u}{\partial x}\right)_i = \frac{u_i - u_{i-1}}{h} + \mathcal{O}(h) \tag{4.20}$$

$$\left(\frac{\partial u}{\partial x}\right)_i = \frac{u_{i+1} - u_{i-1}}{2h} + \mathcal{O}(h^2) \tag{4.21}$$

If the grid spacing is small, the higher-order terms can be ignored, only terms up to the first derivative remains. The power of the grid spacing appearing in the higher order term determines the truncation error which reflects the accuracy of finite difference approximation. In the first two expressions (Equations (4.19) and (4.20)), the approximations are first order accurate because of the first term in *(h)* is proportional to the grid interval, *h*. However, for the last expression (central difference formula, Equations (4.21)) the approximation is the second order (Moczo *et al.,* 2007).

Accordingly, for function *u(x)* the first derivative may be approximated in three different ways, using limits;

$$\left(\frac{\partial u}{\partial x}\right)_i = \lim_{\Delta x \to 0} \frac{u_{i+1} - u_i}{x_{i+1} - x_i} = \lim_{\Delta x \to 0} \frac{u_{i+1} - u_i}{\Delta x} = \lim_{\Delta x \to 0} \frac{u_{i+1} - u_i}{h}, \tag{4.22}$$

$$\left(\frac{\partial u}{\partial x}\right)_i = \lim_{\Delta x \to 0} \frac{u_i - u_{i-1}}{x_i - x_{i-1}} = \lim_{\Delta x \to 0} \frac{u_i - u_{i-1}}{\Delta x} = \lim_{\Delta x \to 0} \frac{u_i - u_{i-1}}{h}, \tag{4.23}$$

$$\left(\frac{\partial u}{\partial x}\right)_i = \lim_{\Delta x \to 0} \frac{u_{i+1} - u_{i-1}}{x_{i+1} - x_{i-1}} = \lim_{\Delta x \to 0} \frac{u_{i+1} - u_{i-1}}{2\Delta x} = \lim_{\Delta x \to 0} \frac{u_{i+1} - u_{i-1}}{2h} \tag{4.24}$$

Similar approaches can be applied to express higher order derivatives. As an example, the approximation of second-order derivatives in central difference scheme is given as,

$$\left(\frac{\partial^2 u}{\partial x^2}\right)_i = \frac{u_{i+1} - 2u_i + u_{i-1}}{(h)^2} + \mathcal{O}(h^2) \tag{4.25}$$

Expressions can be obtained for higher dimensional spaces. As an example, second order difference approximation in 2D is given by,

$$\left(\frac{\partial^2 u}{\partial x \partial y}\right)_{i,j} = \frac{u_{i+1,j+1} - u_{i+1,j-1} - u_{i-1,j+1} + u_{i-1,j-1}}{4\Delta x \Delta y} + \mathcal{O}\left[(\Delta x)^2, (\Delta y)^2\right] \tag{4.26}$$

The procedure in FD method is applicable in the 3D, as well as in the 4D space-time domain. The expressions in those cases become even more complex. In WPP method derivatives are approximated by operators with centered differences, choosing averaging tools for improving efficiency. The expressions are highly complex and are omitted in this thesis (Nilsson *et al.,* 2007).

4.2.4. Analysis of the FD model

The basic aim of the finite difference method for solving partial differential equation (PDE) is to transform the equations into a finite difference equation or a system of FDE (Moczo *et al.,* 2004). In the analysis of the FD model, it is necessary to mention about some significant properties of FDE, such as consistency, stability and convergence which need to be satisfied in order to transform the differential into difference equations. Moczo *et al.* (2004) defined these properties as follows:

Consistency: If the difference between FDE and PDE (the truncation error) disappears according as the size of time step and grid spacing go to zero independently, a finite difference equation is consistent with PDE .That statement can be written briefly as,

$$lim_{\Delta t \to 0, \ h \to 0} |PDE - FDE| \to 0 \tag{4.27}$$

Convergence: Next, we consider the second property namely the convergence. Convergence is obtained if the solution of FDE comes close to the exact solution of the PDE as long as the size of time step and grid spacing go to zero independently. That statement can be written briefly as,

$$lim_{\Delta t \to 0, \ h \to 0}\left(U_{I,J,K}^m - u_{I,J,K}^m\right) = 0 \tag{4.28}$$

Stability: The last important property of FDE is the stability. Stability is controlled by the relation between the exact solution of PDE and its numerical solution. A FDE is stable if it generates a confined solution when the exact solution is confined independently of grid spacing (Moczo *et al.,* 2007). The stability analysis can be practiced for linear PDE, otherwise nonlinear PDE must be linearized (Moczo *et al.,* 2004). It is well known the von Neumann method which investigates local stability is the most common used and simplest method for stability analysis. This method test the stability by making the Fourier analysis of the numerical error in the FDE application. It is only applicable to linear problems. It was first proposed by Crank and Nicholson (1947) then developed at Los Alamos Laboratory. A more detailed description was made by Charney *et al.* (1950). The method is based on checking the variation of error spectrum at consecutive time steps and testing whether the energy is seen to decay at each time step.

It should be noted that consistency describes is the property of the FDE whereas the stability and convergence are the properties of the numerical solution of FDE (Moczo *et al.,* 2004).

4.3. WPP method: General Properties

WPP is the 3-D finite difference tool used in this thesis for wave propagation simulation. Various properties of this method are presented in the following sections. We start by describing the second order formulation of elastic wave equation in WPP. In this part of this thesis, Nilsson *et al.* (2007) is mainly referred.

 For seismic wave propagation we take into account the elastic wave equation for heterogeneous materials in 3-D domain in, Ω:

$$\rho \frac{\partial^2 \boldsymbol{u}}{\partial t^2} = \nabla \xi + \boldsymbol{f}(x, t) \ x\epsilon\Omega, t \geq 0 \tag{4.30}$$

The stress tensor is given by:

$$\xi = (\nabla. \boldsymbol{u})I + \mu(\nabla. \boldsymbol{u} + \nabla. \boldsymbol{u}^T) \tag{4.31}$$

Here, ρ is the density, ξ is the stress tensor, $u = u(\boldsymbol{x}, t)$ is the displacement vector with Cartesian components $u = (u, v, w)^T$.

where $\boldsymbol{x} = (x, y, z)^T$ is the location, t is time, $\boldsymbol{f}$ is the external (volume) force and material properties are described by the density $\rho(x) > 0$ and Lame parameters $\lambda(x) > 0$ and $\mu(x) \geq 0$ (Nilsson *et al.*, 2007).

The following represent the initial conditions:

$$u(x, 0) = U_0(x), \ \boldsymbol{u}_t(x, 0) = U_1(x), \ x\epsilon\Omega \tag{4.32}$$

General boundary conditions which include Dirichlet condition (specification of the value of the solution on the boundary) for $\boldsymbol{u}$ or a normal stress condition is given as;

$$\xi. \boldsymbol{n} = \lambda(\nabla. \boldsymbol{u})\boldsymbol{n} + \mu(\nabla. \boldsymbol{u} + \nabla. \boldsymbol{u}^T)\boldsymbol{n} = \boldsymbol{g} \tag{4.33}$$

This definition describes the stress on a boundary with unit normal $\boldsymbol{n}$. When g=0, this condition is called as free surface or stress-free boundary condition (Nilsson *et al.,* 2007).

The elastic wave equation system (4.30) in Cartesian component form, is given as;

$$\rho u_{tt} = \frac{\partial}{\partial x}((2\mu + \lambda)u_x + \lambda v_y + \lambda w_z) + \frac{\partial}{\partial y}(\mu v_x + \mu u_y) + \frac{\partial}{\partial z}(\mu u_z + \mu w_x)$$
$$+ \boldsymbol{f}^{(x)} \tag{4.34}$$

$$\rho v_{tt} = \frac{\partial}{\partial x}\left(\mu v_x + \mu u_y\right) + \frac{\partial}{\partial y}\left((2\mu + \lambda)v_y + \lambda u_x + \lambda w_z\right) + \frac{\partial}{\partial z}\left(\mu v_z + \mu w_y\right)$$
$$+ \boldsymbol{f}^{(y)} \tag{4.35}$$

$$\rho w_{tt} = \frac{\partial}{\partial x}\left(\mu u_z + \mu w_x\right) + \frac{\partial}{\partial y}\left(\mu v_z + \mu w_y\right) + \frac{\partial}{\partial z}\left((2\mu + \lambda)w_z + \lambda u_x + \lambda v_y\right)$$
$$+ \boldsymbol{f}^{(z)} \tag{4.36}$$

Here Nilsson *et al.* (2007) conceive a box shaped computational domain $0 \le x \le a$, $0 \le y \le b$, $0 \le z \le c$ and introduce stress free boundary condition at flat surface $z = 0$.

The boundary condition (4.33) is given as following in the component form:

$$\mu u_z + \mu w_x = \boldsymbol{g}^{(x)} \tag{4.37}$$

$$\mu v_z + \mu w_y = \boldsymbol{g}^{(y)}, \ z = 0, \ 0 \le x \le a, \ 0 \le y \le b, \ t \ge 0 \tag{4.38}$$

$$(2\mu + \lambda)w_z + \lambda u_x + \lambda v_y = g^{(z)} \tag{4.39}$$

Homogeneous Dirichlet condition (Dirichlet condition is set to zero) at $z = c$ is imposed by Nilsson *et al.* (2007) for the purpose of discussing the stability properties of the method and given as following:

$$\boldsymbol{u}(x, y, c, t) = 0, 0 \le x \le a, 0 \le y \le b \tag{4.40}$$

Definition of the difference scheme for the three dimensional elastic wave equation, it is necessary to describe a 3-D grid with grid points (Nilsson *et al.*, 2007),

$$x_i = (i - 1)h, \ y_j = (j - 1)h, z_k = (k - 1)h \tag{4.41}$$

and

$$0 \le i \le N_x, \ 0 \le j \le N_y, 0 \le k \le N_z \tag{4.42}$$

where $h > 0$ is the grid size,

$$xN_x = a, \qquad yN_y = b, \qquad zN_z = c \qquad (4.43)$$

Time is discretized with time step $\delta_t > 0$ on a grid $t_n = n\delta_t$, $n =$0, 1, 2, and grid function is given by,

$$u^n_{i,j,k} = u(x_i, y_j, z_k, t_n) \qquad (4.44)$$

Second order accurate discretization of elastic wave equation in Eq. (4.34-4.36) is acquired discretizing the differential equation with centered differences by Nilsson *et al.* (2007). Furthermore, free surface boundary condition (4.37-4.39) and Dirichlet boundary condition (4.40) are discretized by centered differences along the boundary.

At this stage it is important to consider the grid spacing which is one of the most critical parameter to choose. It is important that we use sufficiently small grid size because of resolving the waves at high frequencies. On the other hand, we do not want to use an unnecessarily small grid size, because of increasing both the execution time and the memory requirements. Therefore an intelligent choice for the grid spacing is important. We choose the grid spacing in such a way that even the shortest wavelength in the computational domain can be represented efficiently by a sufficient number of grid points. We therefore start by determining what would be the shortest wavelength in our computational domain. Since the shear waves have the lower velocities and shorter wave length than the compressional waves, the shortest wave length L_{min} can be estimated by the following formula;

$$L_{min} = \frac{minV_s}{f_{max}} \qquad (4.45)$$

where V_s is the shear velocity of the material and f_{max} is the largest significant frequency in the time function. Number of grid points per shortest wavelength is an indication of how well a wave is resolved on the computational grid. It is therefore expressed as in the following:

$$P = \frac{L_{min}}{h} \qquad (4.46)$$

Combining the formula (4.45) and (4.46), the number of grid points per shortest wavelength is finally written as:

$$P = \frac{minV_s}{h\,f_{max}} \tag{4.47}$$

Here, we should note that grid size needs to be made small enough in order to maintain the value of P sufficiently high over the whole computational domain, even if either Vs is decreased or the frequency is increased. Many trials and experiences show that WPP gives accurate results for $P \geq 15$. This is the value recommended in the manual of the software package.

4.3.1. Stability, Bounding Energy, Summation by part (SBP) method

There are many different ways of using the finite difference method to discretize the same partial differential equation. However, the most critical issue is the stability. Some FD discretization, especially for early methods, suffered from instability issues when free surface boundary condition was implemented, and the Poisson's ratio became larger excessively (Nilsson *et al.*, 2007).

$$v = \frac{V_p}{V_s} \tag{4.48}$$

In seismic applications, the physical properties of the propagation medium can change rapidly on the computational domain. In other words, the material parameters, ρ, μ and λ may change on a length scale which is markedly smaller than the wavelength of the elastic waves which may easily lead to instability. In order to make sure the stability, it is requirable to enhance a numerical method which satisfies an energy estimate defined for the purpose (Nilsson *et al.*, 2007).

The WPP code achieve this by a new approach, by introducing a second order accurate summation by parts (SBP) method which is stable for all ratios of V_P/V_S. Summation by parts operators are a particular kind of FD stencils that generalize the energy method to bounded domains. The basic idea is to construct special FD operators that mimic the

integration by parts rules, and allow an energy estimate to be derived for some PDEs in bounded domains. Therefore, energy stability can be guaranteed for the overall discretization.

As a result, both the stability of the time-stepping procedure and energy estimation with grid interfaces can be performed by the method which uses summation by parts property. The stability holds for various critical cases, such as heterogeneous material models on both Cartesian and curvilinear grids, for free surface boundary conditions, and for mesh refinement interfaces with hanging nodes. Nilsson *et al.* (2007) stated that the common scheme is a second order accurate approximation of the continuous equation (4.34-4.36) subject to the boundary conditions (4.37-4.40) which is required to satisfy an energy estimate which has to be bounded. More detailed explanations can be found in the paper by Nilsson *et al. (*2007).

4.3.2. Grid (Mesh) Refinement Method

In normal situation, the grid spacing is fixed throughout the computational domain. However it is well known that the velocities in the Earth generally increase with depth. Therefore uniform grid spacing near the surface based on small wavelengths at slowest layers, will result in unnecessary accuracy at depth. In that case, number of grid points in uniform grid is exceedingly large as seen in expression (4.47).

To overcome that over-resolution problem, finite difference scheme is adapted to work on composite grid where grid spacing is increased with depth. In other words, a set of structured rectangular grids of different spacing are applied to the domain (Figure 4.4). To maintain a constant resolution, the grid size should be adjusted such that ratio V_s/h from equation (4.47) becomes approximately constant over the whole computational domain, in particular going down in depth.

Consider a computational domain which is divided into two sub-domains in vertical direction where fine grid of grid size h meets a coarse grid of grid size *2h* as illustrated in Figure 4.4. As it is clear from Figure 4.5, grid point on the coarse grid is co-located with grid point on the fine grid.
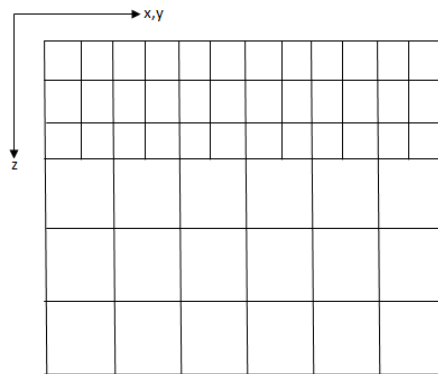
Figure 4.4. 2-D cross-section of the 3-D computational domain with grid refinements.

The particular importance of this composite grid technique is the treatment of the solution at the hanging nodes which leads coupling of the conditions at interfaces. In this case, at refinement interfaces, transitions are handled by assuming ghost point where SBP technique provide stable coupling conditions. When we consider, advancing the solution in time, finite difference scheme is used to update the solution at interior points of both fine and coarse grid. Then, it is followed by assigning solution values to the ghost points through interpolation from the neighboring grid (Petersson and Sjögreen, 2010). Furthermore, in the case of more than two refinements, the interpolation technique applies separately at each interfaces.
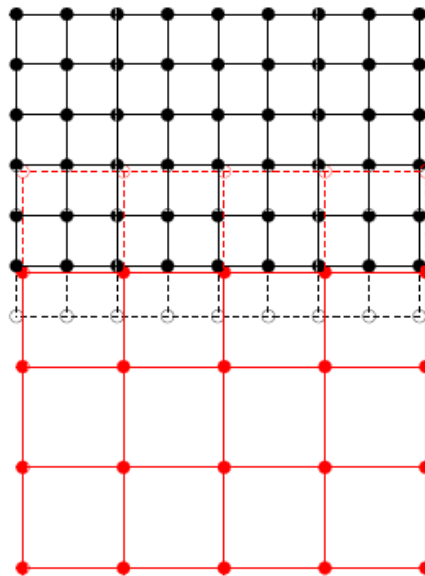
Figure 4.5. Grid configuration at refinement interface. İnterior points are drawn with filled circles and ghost points are drawn with open circles.

As a result, this new approach allows us to express the velocity structure of the propagation medium efficiently by gradually coarsening the computational mesh at depth. Therefore, we have a chance to make finer mesh close the surface where more resolution is desired to resolve short wavelengths in the solution where the wave speed is small, such as in sedimentary basins (http://computation.llnl.gov/project/serpentine/software.html).

Let's consider the example of covering 56kmx43kmx35km computational domain. We use two refinement level that is a refined grid size of 35 m in the top layer (0<z<1000 m) and 70 m in the middle layer (1000 m < z < 6000 m) and finally 140 m for the deep part (z>6000). For comparison, we also simulated the problem on a uniform grid with grid size of 35 fixed throughout the medium. The computational requirements of these two different computational approaches are summarized in Table 4.1. Not surprisingly the uniform grid calculations require more than nine times the number of grid points of the mesh refinement case. It therefore needs much larger computational time on a given cluster. The conservative composite grid case requires 3952 time steps to get total time t=15 while the uniform grid approach has to use 6612 time steps. The total CPU time for uniform grid case is therefore 3 times longer than the conservative composite grid case.

Table 4.1. Comparison of CPU times for composite vs uniform grid.

Grid Type	Grid points	Grid size (m)	Time step	Core	Wall clock (s)	Total CPU(s)
Composite	1.2×10^8	140/70/35	3952	16	36412	6.03×10^5
Uniform	1.3×10^9	35	6612	16	113088	1.809×10^6

Derivation of the energy conserving grid refinement procedure and proof of some theorems related to the procedure will not be expressed here. For more detailed information, see the paper by Petersson and Sjögreen (2010).

4.3.3. Non-reflecting Boundary Conditions

Reflecting waves coming from boundaries of computational domain is one of the most important problems in modelling seismic wave propagation. It is necessary to minimize these

artificial reflections in order to get accurate solution in modelling. Therefore, several definition for boundary conditions in finite difference scheme such as absorbing or non-reflecting and perfectly matching techniques have been suggested in literature. WPP methodology uses the first order nonreflecting boundary conditions which is developed by Clayton and Engquist (1977) at the sides and the bottom of the domain. The physical point of view for these condition shows implementing a differential equation on the boundary which provides wave propagation with chance to move only in one (outward) direction (Nilsson *et al.,* 2007).

For boundaries with, $x = const.$ the boundary conditions are;

$$u_t = \pm V_p u_x \, , \;\; v_t = \pm V_s v_x \, , \;\; w_t = \pm V_s w_x \tag{4.49}$$

where positive signs are considered for lower boundary $x = 0$ and negative signs for the upper boundary $x = a$. Similar equations are applied at boundaries $y = const.$ and $z = const.$ by Nilsson *et al.* (2007).

The discretization of boundary condition works well without the edges in the computational domain. Clayton and Engquist (1977) proposed implementing the nonreflecting boundary condition in a diagonal direction at the edges of the computational domain for example where two nonreflecting boundaries face with each other. However, Nilsson *et al.* (2007) found that implementing some compability conditions along the edges causes a more robust method and it is also easier to impose.

4.3.4. Source terms and source time functions

The source term is generally applied at a point, throughout a line or over a surface in three-dimensional space in seismic wave propagation. Nilsson *et al.* (2007) expressed that sources along lines or surfaces are widely decomposed into a number of point sources distributed along the relating line or surfaces in the application stage.

In seismic applications, two types of point sources occur. First type of point source is the point force, $\boldsymbol{f}_r^{(F)}$. This type of sources are used to model internal forcing based on volcanic eruptions or external forcing performed to the free surface. It is given as,

$$\boldsymbol{f}_r^{(F)}(\boldsymbol{x}, t) = g_r(t) F_r \delta(\boldsymbol{x} - \boldsymbol{x}_r), \qquad F_r = \begin{pmatrix} F_x \\ F_y \\ F_z \end{pmatrix} \qquad (4.50)$$

where $\boldsymbol{x}_r = (x_r, y_r, z_r)$ is the location of point source in space, $g_r(t)$ is the time function, F_r is a constant vector with three component and $\delta(x)$ is the Dirac distribution (Nilsson *et al.*, 2007).

The point moment (general moment tensor or double couple) is the second type of point source and it is expressed by $\boldsymbol{f}_r^{(M)}$. For modelling earthquakes and explosions, point moments are used commonly.

The form is given by Nilsson *et al.* (2007) as following:

$$\boldsymbol{f}_r^{(M)}(\boldsymbol{x}, t) = g_r(t) \mathfrak{M}_r \nabla \delta(\boldsymbol{x} - \boldsymbol{x}_r), \qquad \mathfrak{M}_r = \begin{pmatrix} M_{xx} & M_{xy} & M_{xz} \\ M_{xy} & M_{yy} & M_{yz} \\ M_{xz} & M_{yz} & M_{zz} \end{pmatrix} \qquad (4.51)$$

where and $\mathfrak{M}_r$ is a constant symmetric tensor and $\nabla \delta(x)$ is the gradient of Dirac distribution.

Each term in equation (4.50-4.51) is implemented at the location (x_r, y_r, z_r) and it is preferred to make that location free of grid (Nilsson *et al.*, 2007). It means that it is not necessary to place the sources exactly on grid points. Therefore, discretization of the source term can be as accurate as possible for any location within the computational domain and no artifacts are generated by point source along the line or surface for any location in three dimensional domain.

In WPP, the source time function $g_r(t)$ or $g(t, t_0, w)$ with offset time t_0 and frequency parameter w can be selected from many types of functions. Gaussian function is defined by,

$$g(t, t_0, w) = \frac{w}{\sqrt{2\pi}} e^{-w^2(t-t_0)^2 2}$$ (4.52)

GaussianInt which is the time-integral of Gaussian and often used in earthquake modelling. Ricker function is defined as,

$$g(t, t_0, w) = (2\pi^2 w^2(t - t_0)^2 - 1)e^{-\pi^2 w^2(t-t_0)^2}$$ (4.53)

RickerInt which is the time-integral of Ricker function is sometimes used in seismic exploration simulations. There are other source time functions used in WPP such as Brune, Liu, Triangle, Sawtooth, Ramp and Smoothwave (see WPP Users Guide).

WPP calculates both displacements and velocities. There are different ways for indicating which option is desired. For example if you prefer to get velocities of motion instead of displacement, Gaussian function can be selected for source function. The other approach for obtaining 'velocity' output is to choose GaussianInt as source and selecting the velocity option in output. We preferred using second approach in order to get three component velocity of motion in our WPP simulations.

4.4. Verification of WPP Code

We have made experiment to verify the result of the finite difference code in 3D with those of 1-D simulations. We have compared the seismograms from WPP using a horizantally layered 1D model to seismograms computed with the discrete wave number method (DWNM) by Bouchon (1981). The discrete wave number method computes wave propagation for a double couple source, with a chosen focal mechanism and source time function. The actual Fortran code used for DWNM application is the one described by Bouchon (2003). The comparisons of the two methods were done using a simple crustal model with horizontally layered velocity structure as given by Karabulut *et al*. (2002) for the Eastern Marmara. This model is shown Table 4.2. The waveforms to be compared are the ones that are recorded at the locations corresponding to the stations of the Rapid Response network, as shown in Chapter 5.

The common seismic source used for the comparison was chosen to be the Çınarcık Earthquake of 29 September, 2004 (Ml=4.1). The accurate location and focal mechanism are estimated in detail and will be shown in the next chapter. The parameters for this events are given in Table 4.3. The input parameters for both methods (WPP and DWNM) are slightly different but closely connected. The parameters used for both methods are listed in detail in Table 4.4. The input parameter for the WPP is seismic moment whereas for DWNM it is the area and the slip. Therefore a rigidity value need to be assumed (rigidity value of $\mu=5 \times 10^{10}$ dyn/cm^2). We calculated the seismic moment as 1×10^{22} dyn.cm corresponding to the fault area of 1 km^2 and a slip of 20 cm on the average. We selected a rupture velocity of 3.2 km/s from the kinematic model of the Izmit earthquake (Bouchon, 1981; Pulido *et al.,* 2004). This roughly corresponds to a source pulse duration of 0.3125 s for the 1-D modelling. For the 3-D modelling (WPP), we have chosen the Gaussian pulse shape and selected an angular frequency of 2.5 Hz which roughly corresponds to a similar pulse duration (Table 4.4).

Table 4.2. Velocity model used for 1D Synthetic Seismograms

Thickness (km)	P-Velocity (km/s)	S-Velocity (km/s)	Density (kg/m^3)
1.0	2.25	1.31	2.4
5.0	5.70	3.31	2.5
14.0	6.10	3.55	2.8
13.0	6.80	3.95	2.9
0.0	8.00	4.65	3.0

Table 4.3. Source parameters for Çınarcık Earthquake of 29 September, 2004 (Ml=4.1)

Parameters	Values
Lattitude (deg.)	40.795
Longitude (deg.)	29.051
Hypocentral Depth (km)	9.6
Strike-Dip-Rake (deg.)	112-90-108
Magnitude	4.1

Table 4.4. Input parameters used for DWNM and WPP

DWNM		WPP	
Fault Area (km^2)	1.0	Seismic Moment (dyn.cm)	10^{22}
Slip amp.(m)	0.02	Source type	GaussianInt
Rupture Vel. (km/s)	3.2	Freq (Hz)	2.5

Figure 4.6 represent three component seismograms computed with WPP and DWN methods, for two different stations. R76 station has distance of 16.21km and azimuth of 31.78 deg. while distance and azimuth of the station R36 is 21.9km and 22 deg., respectively. Both synthetics are low pass filtered at 1.6 Hz by a second order Butterworth filter, applied one way. It is clearly observed that amplitude and waveform shapes are very much similar in each method. There is also no apparent bias in the arrival times of energy between WPP and Bouchon's synthetics. Note that this comparison is valid for the distances and event characteristics that corresponds to the local scale. This setting coincide exactly to our working range at the Eastern Marmara. It is natural to think that at other scales, such as regional or very near field comparisons, the above comparison may not be valid.
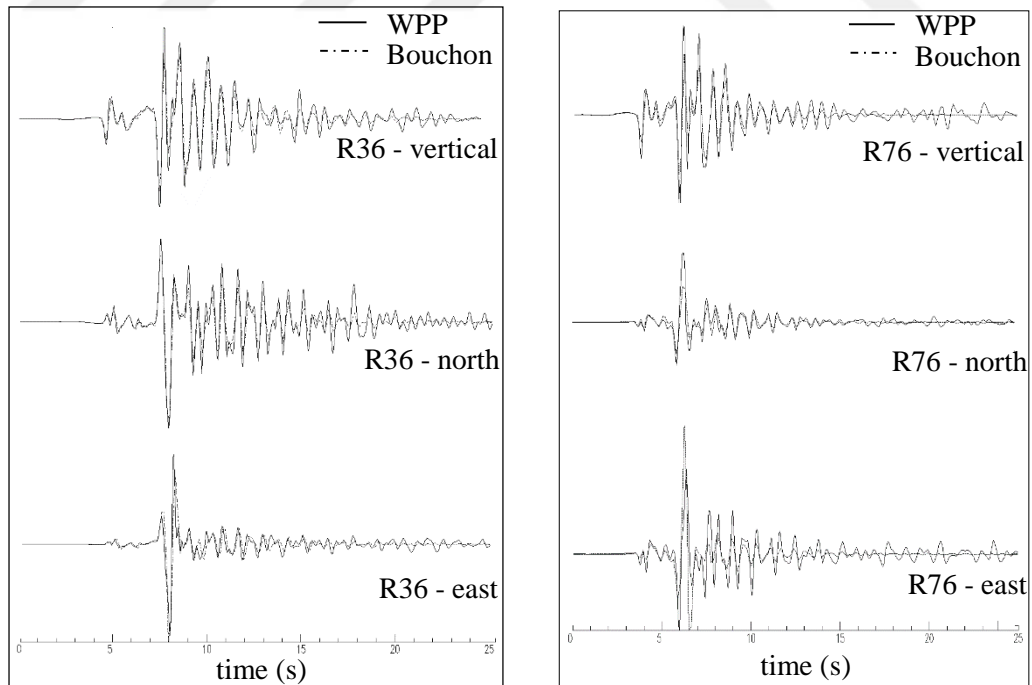
Figure 4.6. Comparison of synthetic seismogram computed with the WPP (solid line) and Bouchon (dashed line) codes at stations R36 (left) and R76 (right). Synthetics are shown with same amplitude and time scales for three components.

4.5. Computational Resources

The information about the computer program we have used for seismic wave propagation (WPP), is referred from the website of center for applied scientific computing of LLNL (http://computation.llnl.gov/project/serpentine/software.html). The computer program carries out important abilities for 3-D modeling such as a fully 3-D heterogeneous material model indication, output of synthetic waveforms in the SAC format and output of GMT scripts marking the simulation results on a map. However the most important property is that it has the capability to run on parallel processing environment.

The code is written mostly with C++ along with some C and Fortran. A distributed memory programming model that is practiced with the MPI library is also used. Therefore, MPI library must be available in order to compile the code for parallel processing. That provides support for message passing on parallel machines. WPP can be built on GNU, operation on Intel or IBM based laptops or desktops running LINUX and OSX using coherent versions of C++ and Fortran 77 compilers.

We have built the code on two different high performance computers, namely the large Linux clusters at İstanbul Technical University National Center for High Performance Computing (ITU-UYBHM) and the TUBITAK Turkish academic network and information Center (TUBITAK-ULAKBIM) systems. WPP code has been installed and compiled on both centers and it is fully operational today. More detailed information about these centers and their systems are given separately, below.

TUBITAK-ULAKBIM CENTER: High-performance computing, data intensive computing, scientific data warehouses services are provided by an infrastructure which is operated by TÜBİTAK ULAKBİM and called as TR-Grid until the end of 2010, and as of 2011 called as TRUBA. TRUBA is the national e-Infrastructure supporting nearly 1000 researchers from 50 different universities for their scientific research. Two cluster, called Levrek and Mercan were both used in our computational work. Technical specifications of these clusters are presented in Table 4.5. As seen in Figure 4.7 the host is connected to ethernet switching system and 128 parallelized PC.

Table 4.5. Technical specifications of Levrek and Mercan Clusters

	Levrek Cluster	**Mercan Cluster**
Processor type	Intel E-5 2690 2.90GHz	Opteron 6176 2.30GHz
Number of Node	128	192
Number of Core	128 x 8 x 2CPU = 2048	192 x 12 x 2CPU = 4608
Architecture of memory	Distributed	Distributed
Memory	256GB per node	128GB per node
Operating system	Centos 6.5 Linux	Centos 6.5 Linux
Job queue system	PBS (Portable Batch System) Scratch file system	PBS (Portable Batch System) Scratch file system

Figure 4.7 Levrek Cluster in TÜBİTAK-ULAKBİM Center

ITU UYBHM Center: UHEM provides high performance computing (HPC) and storage infrastructure services for academic, industrial, public and private projects, both at national and international level. UYBHM provides with more than 30 million core-hours for

academic research projects since 2006. Our WPP code is running on Anadolu cluster which the technical specifications presented in Table 4.6.

Table 4.6. Technical specifications of Anadolu Cluster

	Anadolu Cluster	
Processor type	Intel Xeon 2.33 GHz	
Number of Node	192	
Number of Core	1004	
Architecture of memory	Distributed	
Memory	8GB (for 2 core nodes) 16 GB (for 4 core nodes)	
Operating system	CentOS 5.4 x86_64	
Job queue system	LSF (Load share facility)	

4.6. Details of Parallel Computations

In parallel computing, one of the critical step is to determine the optimal number of processors that are required to run the code efficiently. The efficiency is a factor which depends on the size and the complexity of the problem, the memory usage, the disk usage, etc. In practice, a typical code configuration is tested with increasing number of processors. The total CPU time is found in each case and compared. In a stable applications, one finds that the CPU time reaches a steady state level above a given number of processors. In other words, for a given problem size, using extra processors does not lead to a significant improvement. It is then logical to execute the code with the minimal number of processors. This process is called the scaling test. When testing with Tübitak parallel system, we found the WPP in our application has good scaling after 16 processors. Therefore, the program was mostly run with 16 processors (see Figure 4.8).

The operation of the WPP is totally determined by the setting of the user selected input parameters required by the code. These parameters are most of the time determined by the physical conditions set by the problem at hand such as the size of the domain, the range of

seismic velocities, the frequency of interest, the duration of the signal, etc. The user has to adapt these input values according to his own needs. On the other hand, there are also some parameters that are automatically chosen by the code itself. The sampling frequency is one of such parameters that are automatically determined by the code, but based on the user input parameters.
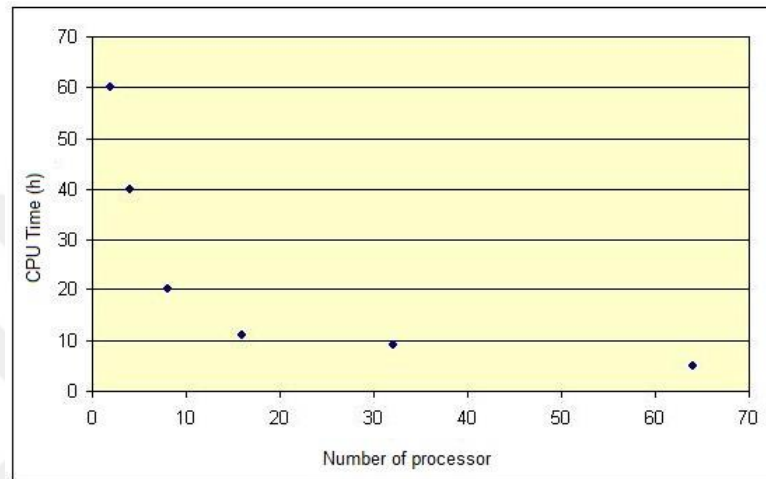
Figure 4.8. WPP Scaling on LEVREK cluster at ULAKBIM

The computational time, in particular the total CPU time, (i.e. excluding waiting queue, disk I/O, etc.) is expected to be a function of the total number of grid points in space and the total number of sample point in time. We have made some tests to develop an empirical function which estimate the total CPU time for a given set of input parameters. This function will naturally depend on the particular system and the particular number of processor. However the dependency of the CPU time on the input parameters will basically remain the same. In order to establish this relation we have performed some empirical tests whose outcomes are summarized in Table 4.7 and 4.8.

The number of grid points in space and time are the primary parameter which determine the computational time. We represent the number of grid points in space is by N_{grid} and the number of sample points in time by N_{samp}. N_{grid} depends on the total volume of the domain (*Length x Width x Depth*) and the grid spacing (*h*), which are values determined

by the user. These parameters are given in the first and second columns in Table 4.7. Number of grid points in space is defined as,

$$N_{grid} = \frac{L}{h} x \frac{W}{h} x \frac{D}{h} = \frac{Volume\ (V)}{h^3} \tag{4.54}$$

Note that grid spacing, h comes into effect as power of 3.

The second parameter, namely the number of sample points in time (N_{samp}), in other words time steps, depends on both the signal duration (T_{total}) and the sampling time dt. The number of sample points, can be defined as,

$$N_{sample} = \frac{T_{total}}{dt_{true}} \tag{4.55}$$

The signal duration, seen in the eleventh column of table 4.8 is also given by user. However the sampling time is automatically determined by the program itself where user cannot intervene. The calculation of the time step in WPP is performed in the subroutine named, computeDT(). The simplest case occurs for a purely elastic material in Cartesian coordinates. All grid points are scanned to find the largest value of the velocity:

$$v = max\left(\sqrt{\left(\frac{(4\mu + \lambda)}{\rho}\right)}\right) \tag{4.56}$$

$$dt_{limit} = \frac{h}{v} \tag{4.57}$$

The sampling time is then calculated by,

$$dt_{true} = \frac{CFL * h}{v} = CFL * dt_{limit} \tag{4.58}$$

where is the v maximum wave speed encountered in the model, h is the grid size and CFL (Courant-Friedrichs-Lewy) is a stability factor (Courant *et al.*, 1956). In most of our

applications CFL took a value close to 0.6. In the case of using attenuation, the computation of v also involves the viscoelastic parameters. The automatically selected time step (named as true time step) is shown in nineteenth column of Table 4.8.

The total computation time is estimated to be proportional to the product of N_{grid} and N_{sample}. We have found a proportionality factor empirically through our tests which we have successfully used in our implementations. This empirical relation is given by;

$$Computational\ Factor_{etimated} = \frac{Volume\ (V)}{h^3}\ x\ \frac{T_{total}}{dt_{limit}} * \frac{1}{CFL} \tag{4.59}$$

In order to clarify the interpretation of parameters, we can take an example s which is presented in the Table 4.7. One of them shows that the computational domain is covered by the area of 20x20x20km, in other words the volume of volume $8x10^{12}$ .The source time function in this problem is a Gaussian. Note that the source time duration (σ) is 0.4sec corresponds to freq parameter of 2.5Hz in the input file. The center frequency, f_o can be calculated as 0.63 Hz. Since we are using a Gaussian time-function, we estimate the maximum frequency (upper power frequency) to be $fmax \approx 2.5xf_0 = 2.5x0.63$. Therefore, we can find the maximum frequency to be ~1.57Hz. For this same example, the material model has a minimum velocity of 2300 m/s and a maximum velocity of 6000m/s and the grid size is h =100m for a uniform grid. By using formulas (4.43)-(4.45), we can calculate the number of points per wave length for this simulation,

$$P = \frac{2300}{100x1.57} = 14.6$$

Sampling time read in SAC file after simulation is 0.0101sec and limit dt value is found out as 0.01667sec from eq. (4.57). The uniform grid requires 1475 true time steps to get total time t=15 while estimated time step is calculated as 1475 using eq. (4.55) and (4.58). Finally, using an average value for CLF (0.6), the CPU time is estimated as 472 sec while the true CPU time from WPP output is given as 481.

Table 4.7. Computational experiments

Vol. (m^3)	h (m)	N$_{grid}$	Grid Type	min Vs (m/s)	Max Vp (m/s)	w (Hz)	f$_o$ (Hz)	f$_{max}$ (Hz)	P
8,4x10^{13}	70	2,45x10^8	Unif.	2300	6000	2,5	0,63	1,57	20,92
8,4x10^{13}	61	3,70x10^8	Unif.	2300	6000	2,5	0,63	1,57	24,00
8,4x10^{13}	61	3,70x10^8	Unif.	2300	6000	2,5	0,63	1,57	24,00
8x10^{12}	100	8,00E+06	Unif.	2300	6000	2,5	0,63	1,57	14,64
8x10^{12}	150	2,37E+06	Unif.	2300	6000	5	0,80	1,99	7,71
8x10^{12}	60	3,70x10^7	Unif.	2300	6000	5	0,80	1,99	19,27
8x10^{12}	80	1,56x10^7	Unif.	2300	6000	5	0,80	1,99	14,45
8x10^{12}	60	3,70x10^7	Unif.	2300	6000	15	2,39	5,97	6,42
1,4x10^{13}	35	3,27x10^8	Unif.	1310	8000	15,0	2,39	5,97	6,27
1,4x10^{13}	35	2,51x10^7	Unif.	1310	8000	15,0	2,39	5,97	6,27
1,4x10^{13}	50	1,12x10^8	Unif.	1310	8000	15,0	2,39	5,97	4,39
1,4x10^{13}	100	1,40x10^7	Unif.	1310	8000	15,0	2,39	5,97	2,19
1,4x10^{13}	100	1,40x10^7	Unif.	1310	8000	15,0	2,39	5,97	2,19
8,42x10^{13}	35	1,20x10^8	Comp.	1310	8000	15,0	2,39	5,97	6,27
8,42x10^{13}	35	1,18x10^8	Comp.	300	8000	2,5	0,63	1,57	5,46
8,42x10^{13}	35	1,18x10^8	Comp.	300	8000	2,5	0,63	1,57	5,46
4,17x10^{13}	35	5,88x10^7	Comp.	300	6000	2,5	0,63	1,57	5,46
1,35x10^{13}	35	2,95x10^7	Comp.	1710	8000	2,5	0,40	0,99	49,12
3,48x10^{13}	35	7,61x10^7	Comp.	1710	8000	15,0	2,39	5,97	8,19
3,48x10^{13}	35	8,57x10^7	Comp.	1310	6000	2,5	0,63	1,57	23,83
3,96x10^{13}	35	8,65x10^7	Comp.	230	6000	2,5	0,63	1,57	4,18
4,648x1^{13}	25	2,31x10^8	Comp.	230	6000	2,5	0,63	1,57	5,86
1,4x10^{13}	100	1,40x10^7	Unif.	1800	8000	2,5	0,63	1,57	11,46
1,4x10^{13}	100	1,40x10^7	Unif.	1310	9500	2,5	0,63	1,57	8,34
1,4x10^{13}	100	1,40x10^7	Unif.	1310	7500	2,5	0,63	1,57	8,34
1,4x10^{13}	100	1,40x10^7	Unif.	1310	11000	2,5	0,63	1,57	8,34

Table 4.8. Computational experiments cont.

T_{total} (s)	True dt (s)	Limit dt (s)	CFL	True Time Steps	N_{sample}	Exp. Comp factor	STF	Est. CPU Time (s)	True CPU Time (s)
50	0,00712	0,01167	0,61003	7025	7024	$1,72x10^{12}$	Gauss	68809	25668
50	0,00620	0,01017	0,61002	8062	8061	$2,98x10^{12}$	Gauss	119322	105958
15	0,00620	0,01017	0,61002	2419	2418	$8,95x10^{11}$	Gauss	35797	41058
15	0,01017	0,01667	0,61016	1475	1475	$1,18x10^{10}$	Gauss	472	481
15	0,01526	0,02500	0,61038	983	983	$2,33x10^{9}$	Gauss	93	79
15	0,00610	0,01000	0,61000	2459	2459	$9,11x10^{10}$	Gauss	3642	1871
15	0,00813	0,01333	0,61005	1844	1844	$2,88x10^{10}$	Gauss	1152	1871
15	0,00813	0,01000	0,81340	1844	1220	$4,52x10^{10}$	Gauss	1808	1871
15	0,00270	0,00438	0,61714	5556	5619	$1,83x10^{12}$	Gauss	73397	113196
15	0,00379	0,00438	0,86629	3958	5619	$1,41x10^{11}$	Gauss	5631	5871
15	0,00386	0,00625	0,61808	3883	3934	$4,41x10^{11}$	Gauss	17623	20112
15	0,00772	0,01250	0,61760	1943	1967	$2,75x10^{10}$	Gauss	1101	809
15	0,00772	0,01250	0,61760	1943	1967	$2,75x10^{10}$	G.int	1101	863
15	0,00380	0,00438	0,86766	3952	5619	$6,75x10^{11}$	Gauss	27018	38443
15	0,00380	0,00438	0,86766	3952	5619	$6,64x10^{11}$	G.int	26575	31563
30	0,00380	0,00438	0,86766	7903	11239	$1,33x10^{12}$	G.int	53151	56378
30	0,00379	0,00583	0,64971	7916	8429	$4,96x10^{11}$	G.int	19828	27338
40	0,00408	0,00438	0,93257	9804	9804	$2,89x10^{11}$	G.int	11568	11040
30	0,00408	0,00438	0,93257	7353	7353	$5,60x10^{11}$	G.int	22385	20400
30	0,00379	0,00583	0,64971	7916	8429	$7,23x10^{11}$	G.int	28904	45454
30	0,00455	0,00583	0,77946	6598	6598	$5,71x10^{11}$	G.int	22835	21600
30	0,00324	0,00417	0,77754	9260	11801	$2,72x10^{12}$	G.int	108915	108360
15	0,00772	0,01250	0,61760	1943	1967	$2,75x10^{10}$	Gauss	1101	532
15	0,00693	0,01053	0,65789	2166	2336	$3,27x10^{10}$	Gauss	1308	595
15	0,00802	0,01333	0,60160	1870	1844	$2,58x10^{10}$	Gauss	1033	513
15	0,00624	0,00909	0,68693	2402	2704	$3,79x10^{10}$	Gauss	1514	667

5. OPTIMAL SOURCE PARAMETERS

The main motivation of this chapter is to achieve a higher accuracy in comparing the observed and the synthetic waveforms in seismic wave propagation application. Increasing earthquake location quality and determining optimal source parameters such as origin time, magnitude and especially focal mechanism parameters have prominent role for developing realistic and detailed crustal models. Therefore, the source parameters are recalculated for selected reference events using strong motion instruments of the Rapid Response (RR) Network as well as the broad seismic network. In this chapter, data availability for the reference earthquakes is examined first. Then, hypocenter location procedure is modified and adapted for the particular geometry of the strong motion network, which provides a dense set of arrival times in a relatively narrow angle of azimuth coverage. In a similar fashion the fault plane solution procedure is adapted to take into account the amplitude information provided by the dense network of strong motion instruments. First, the conventional method of first motion polarity is used to determine the fault plane solution. A waveform based method using the amplitude of the first arrival is applied at the second step in order to have a more accurate estimate. Results concerning the source parameters for the reference event are summarized at the last part of this chapter.

5.1. Data and Network availability

Standard location and source analysis procedure were carried out using data acquired by 18 permanent broadband stations, which are operated by BDTIM (Regional Earthquake–Tsunami Monitoring Center). In our situation, an additional data source is also available, namely the RR stations installed both in the European and the Anatolian part of the Istanbul Metropolitan area. These stations are installed in the content of the Istanbul Earthquake Early Warning and Rapid Response (IEEWRR) system and consist of 100 strong motion stations operated by KOERI. Installation of the RR system is an important attempt to implement earthquake risk mitigation efforts for city of Istanbul (Erdik *et. al*., 2003a). The system, if triggered, has the potential of providing significant data for the study of close events (Erdik *et al*., 2003b). Since its installation, the RR system has not recorded too much earthquakes

which have magnitude greater than 4.0. Broadband station distribution in Marmara region and strong motion stations in İstanbul metropolitan is shown in Figure 5.1 respectively.
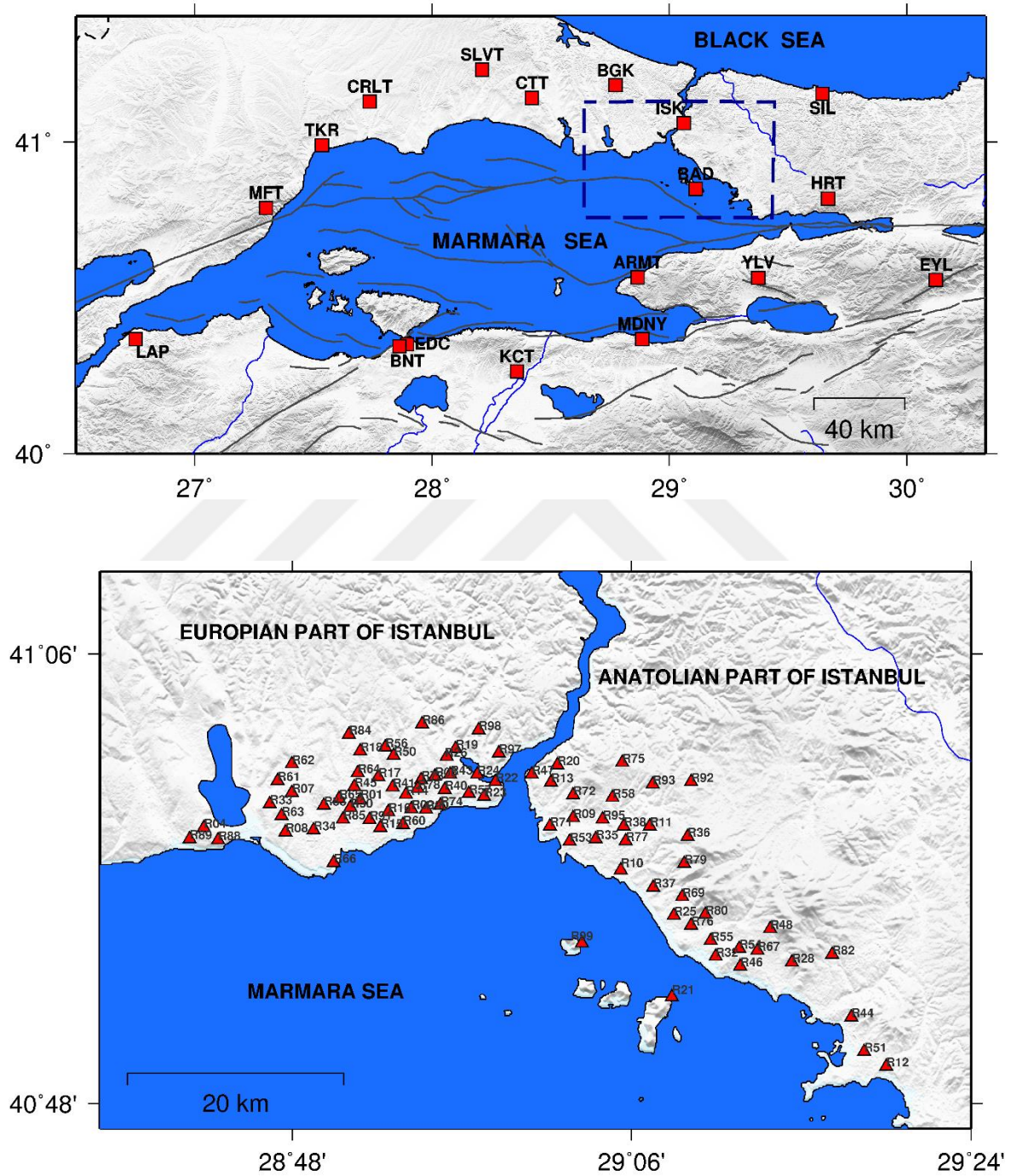
Figure 5.1. KOERI seismic network around Marmara (top), rapid response stations around Istanbul (bottom).

The use of the recorded ground motions at the RR System station sites in Istanbul is the critical step for the development of our 3D wave propagation simulation. For this purpose, moderate size earthquakes that occurred on May 16, 2004 (Mw=4.2), on September 29, 2004 (Mw=4.1) and on March 12, 2008 (Mw=4.8), are selected as test events for the simulation of wave propagation. These events were the only close events which triggered and therefore recorded by the RR System, at the time this study started.

Location and fault plane solution of these reference earthquakes are shown in Figure 5.2. Note that these are the final solutions determined by our detailed analysis on location and focal mechanism. As we see, earthquakes on May 16, 2004 and September 29, 2004 are located on Northern boundary of Çınarcık Basin, along the North Anatolian Fault. Source parameters of these events after analysis are also presented in Table 5.1. The earthquake of September 29, 2004 with magnitude 4.1, occurred in Çınarcık Basin, south of Prince's Islands is analyzed first. This event is chosen as the primary event for model testing because it provided the major part real data to be compared with the synthetics. This earthquake is recorded by 86 strong motion stations. Reasons of choosing that earthquake as the prime target for the study is the fact that the RR records have high S/N ratio and a very dense azimuthal coverage related to its close epicenter location.
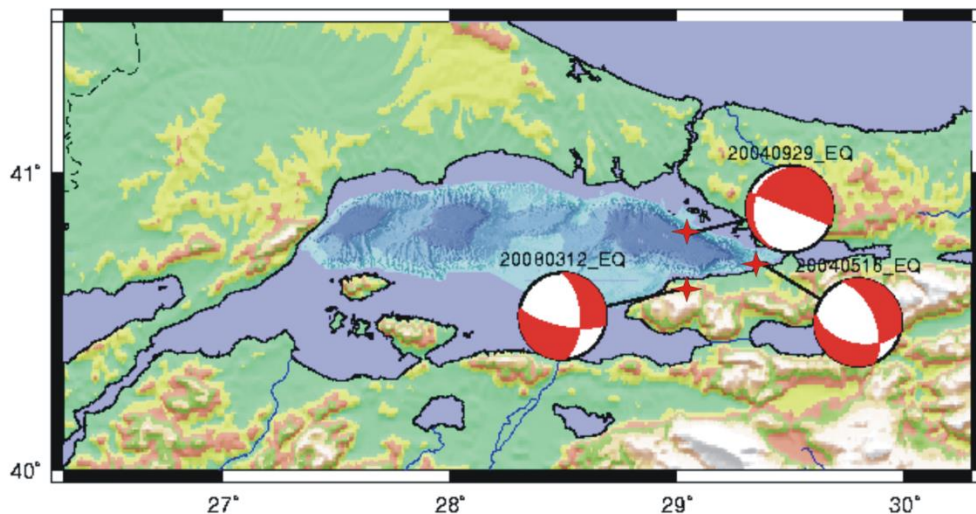
Figure 5.2. Reference events and their fault plane solutions determined by our analysis.

Table 5.1. Source parameters of reference events.

Event ID	Origin time	Lat. (deg.)	Long. (deg.)	Depth (km)	Mag	Strike (deg.)	Dip (deg.)	Rake (deg.)
20040929	154208.5	40.795	29.051	9.6	4.1	112.00	90.00	108.00
200404.25 16	033049.4	40.709	29.353	8.6	4.2	337.71	56.97	-50.80
20080312	185331.9	40.614	29.040	11.5	4.8	358.21	56.17	-22.76

5.2. Pre-Processing of Data

Before the analysis, some pre-processing steps are applied to the seismograms. Firstly, format conversion from GSR to SAC was applied to all strong motion data using GeoDAS 2.21 (GeoSIG Data Acquisition System) program. All acceleration records were converted to velocity and displacement recordings. Also, each velocity seismogram is rotated from N-S and E-W component to radial and transverse component in order to determine SH phase clearly due to the fact that it predominantly contains the transverse component. After that, we applied baseline correction to the velocity data. There is also another way that is a direct approach to apply baseline correction to the acceleration data and then integrating the waveform to velocity data. After that step, P and S phase picking was carried out manually on velocity seismograms. After picking body wave phases the amplitude of the P-arrival is estimated. This is done by windowing P phase and finding the maximum amplitude automatically. Pre-processing steps are summarized in Figure 5.3. Some examples of data preparation are also shown in Figure 5.4 and Figure 5.5. Acceleration, velocity and displacement data are presented for station R41 in Figure 5.4. Velocity data without baseline correction and after baseline correction for the same station (station R41) is presented in Figure 5.5.
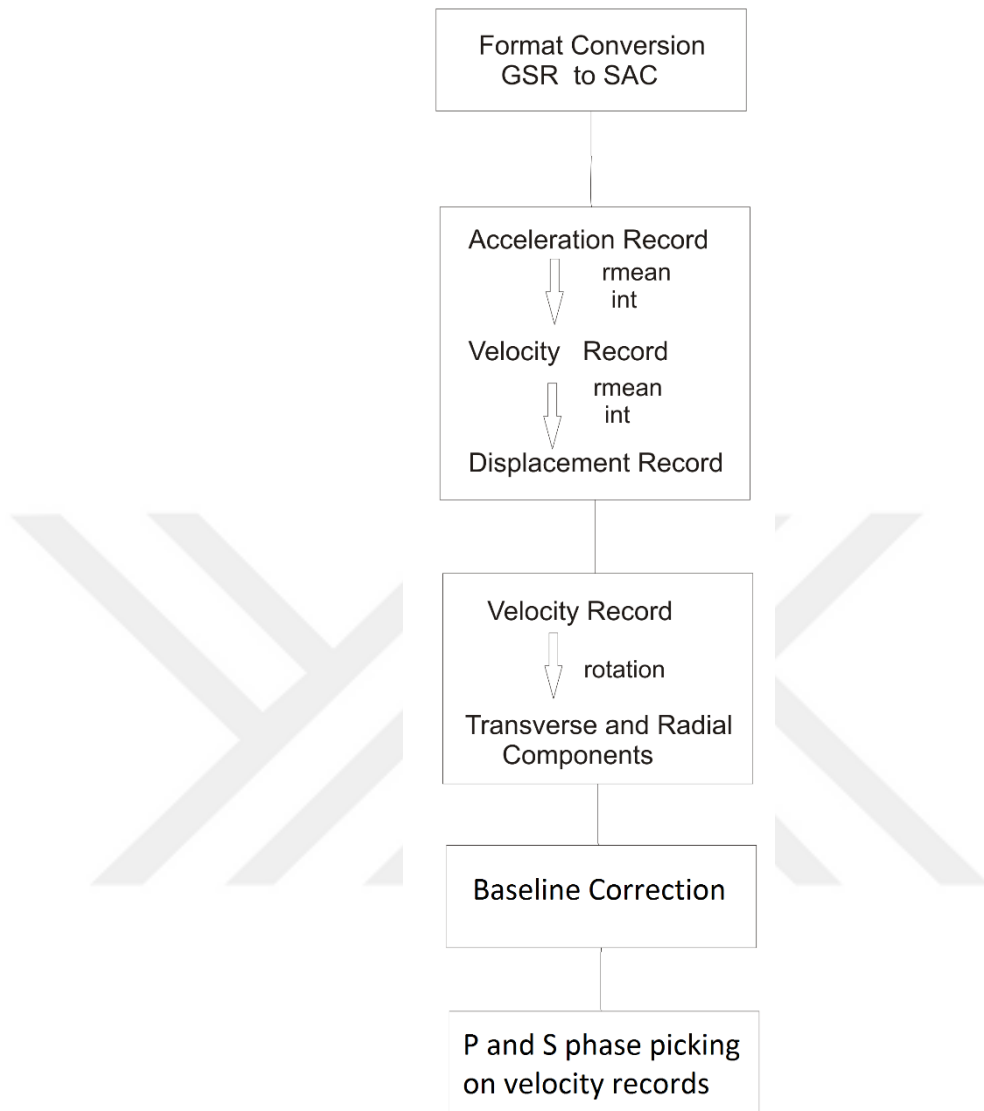
Figure 5.3. Flow chart for data preprocessing.
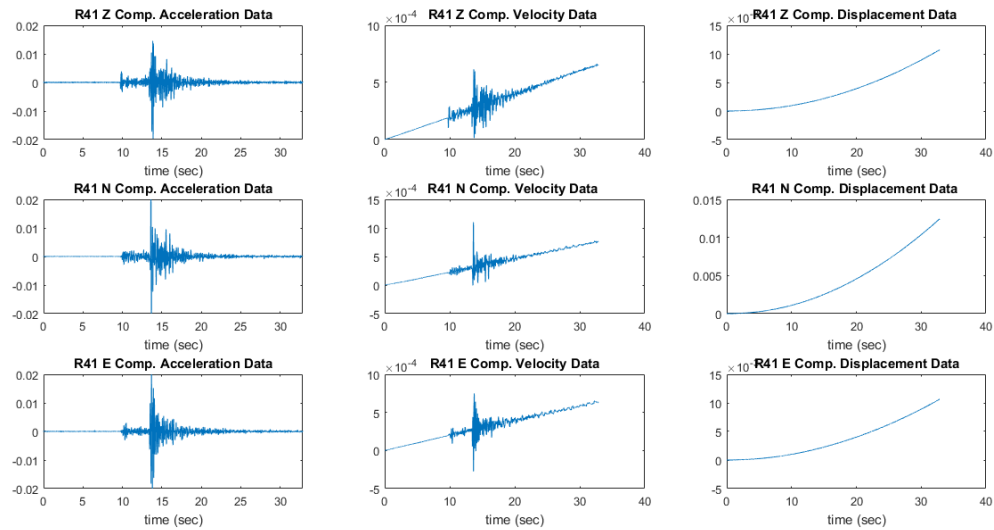
Figure 5.4. Acceleration, velocity and displacement waveforms for station R41.
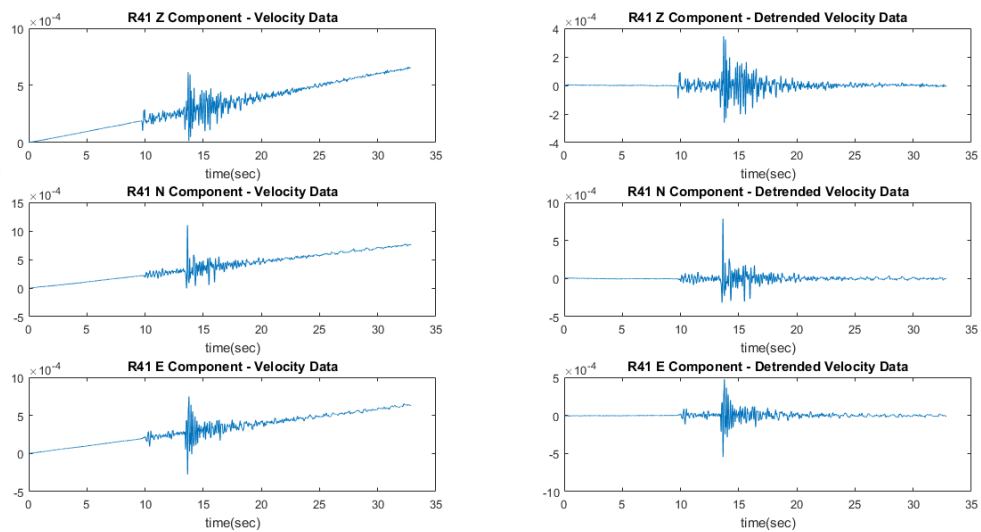
Figure 5.5. Velocity data obtained after baseline correction for station R41.

5.3. Source Location of Reference Event (September 29, 2004)

We relocated events in order to find out the optimal location that fits all the phase readings that come from both from weak and strong motion instruments. We have repeated the relocation for the all different velocity models that were proposed in the literature for the same area and estimated the uncertainty in each case. Namely we used models from the

BDTİM, Karabulut *et al.* (2002) and Bulut *et al.* (2007) which are given in Table 5.2. The first one is the crustal model used for online location for the whole Turkey and therefore is too simplistic model to reflect the details of the Eastern Marmara. Therefore we have retained only the latter two.

Table 5.2. Comparison of different velocity models

		Depth (km)	P wave Velocity (km/s)
From Karabulut *et al.* (2002)		0.0	2.25
		1.0	5.70
		6.0	6.10
		20.0	6.80
		33.0	8.00
From BDTİM		0.0	4.50
		5.4	5.90
		31.6	7.80
		89.2	8.30
From Bulut *et al.* (2007)		0.0	2.9
		1.0	4.7
		7.0	5.3
		11.0	6.06
		15.0	6.88
		35.0	8.06

HYPO71 (Lee & Lahr 1975) and SEISAN (Haskov and Ottemöller, 1999) codes are applied to locate the event. P and S phase were picked manually from the broadband and the short period permanent stations as well as the 86 RR stations, all operated by KOERI. A total of 115 P and 81 S phase reading were used. Only stations with distance less than 100km were kept for the final analysis.

When we locate the event, if nothing fixed, the source depth converge to 13.4 km and the residual error in terms of root mean square (RMS) is 0.4. If the depth is fixed to 8 km, RMS is 0.5 and if it is fixed to 5 km RMS is 0.6. We see that as the depth become shallower the RMS value increases, which means that time residual increases for the majority of the stations. However one must note that the azimuthal coverage is unbalanced and therefore the stations on the north, which have the majority determine the RMS totally, while the ones on the south although being critical do not influence the final location. In fact the station such

as YLVX, which is located on the south of the epicenter, behaves oppositely to the ones on the north and gives a smaller error for shallower source. It is clear that the use of 1-D crustal structure fails to provide a satisfactory location in this example. We have therefore adjusted the final location not only for minimizing the RMS but also providing a good fit to the southern stations. One last remark is that a shallower depth (8-9 km) put the hypocenter exactly on the fault plane while the depth of 13.4km moves it south of the main fault plane determined by Armijo *et al.* (2002).

In order to improve the relocation we also had to perform some modifications for the crustal velocity models. We have plotted the travel time against distance curves for the two models studied. For both the case of Bulut *et al.* (2007) crustal model (upper left of the Figure 5.6) and that of Karabulut *et al.* (2002) (upper right of the Figure 5.6), we see that the observed and the calculated arrival are consistent especially for P waves at the distance range between 15-35 km. For the case of Karabulut *et al.* (2002) model, we can see the consistency also extends to closer stations (< 15 km). However, for S arrivals, we observe that there is a scattering for both models, above a certain distance (>20 km). In both models the S-wave velocity are directly determined from the P-wave velocity. When we reduce the Vp/Vs ratio from 1.78 to 1.72 in the velocity model of Karabulut *et al.* (2002), we see that calculated S arrival times are coincide well observed ones (lower left of the Figure 5.6). As we mentioned before it should be noted that the solution with the minimum error gives a high error for both YLVX and ARMT permanent stations in all models. Furthermore YLVX and ARMT also differ significantly with each other. For our final decision we choose YLVX as the more reliable one because it seems to be more in line with the S travel time of other neighboring stations. Finally, we adjust the depth to 9.6 km, which gives more consistency for the observed and the calculated time for YLVX station, while keeping the overall rms error at an acceptable level (lower right of the Figure 5.6).
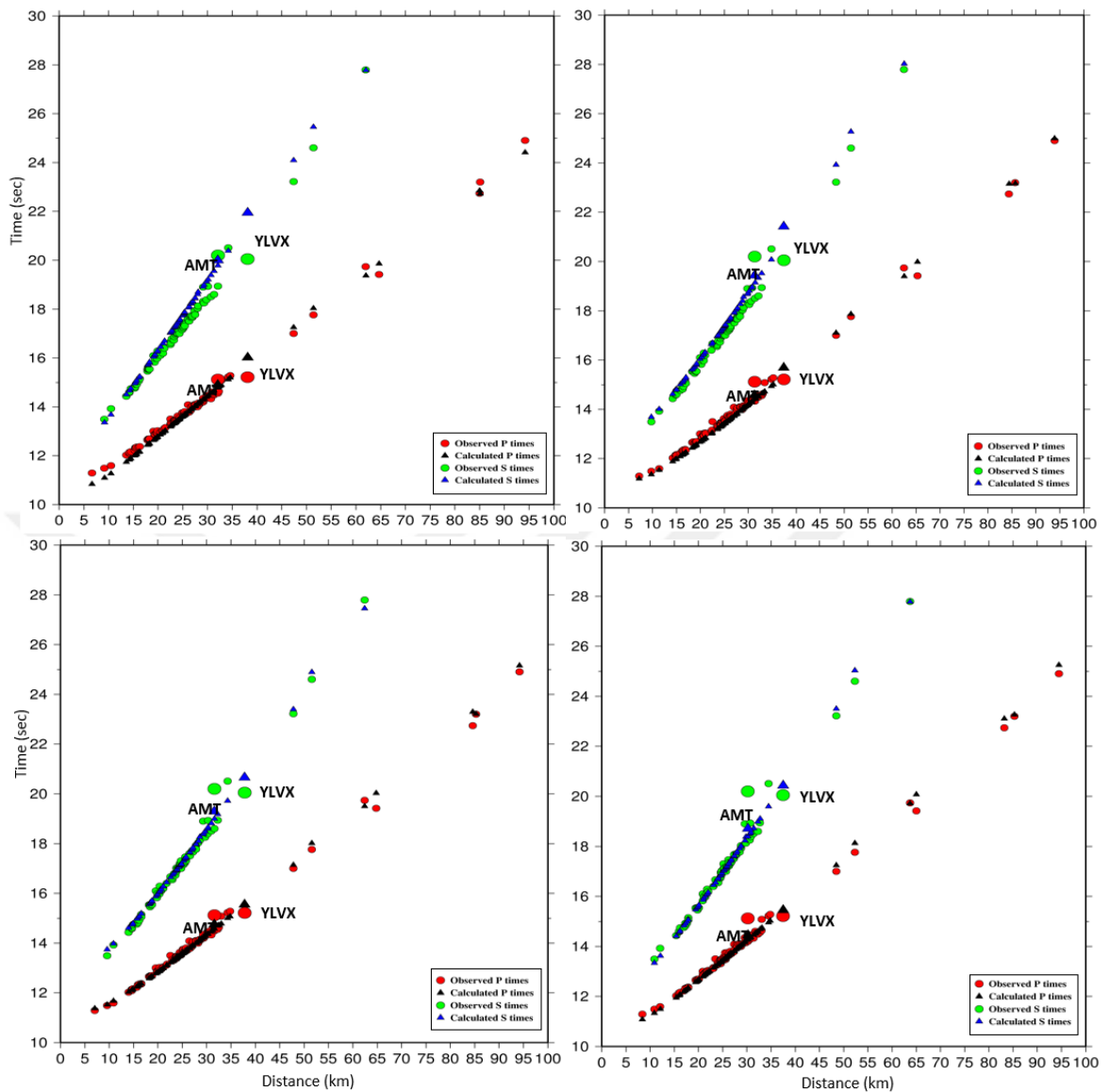
Figure 5.6. Arrival time vs distance curve for P and S waves from four different velocity models. Model of Bulut *et al.* (2007) is shown in the upper left, model of Karabulut *et al.* (2002) is shown in upper right, our velocity model is given in lower left and our velocity model of with depth is fixed 9.6km is given in lower right of the figure.

The hypocenter parameters of our location and that of the BDTİM (Table 5.3) are shown in Figure 5.7.

Table 5.3. Hypocenter parameters of the event from BDTİM and our study.

Event ID	Origin time	Lat (deg.)	Long (deg.)	Depth (km)	Number of Stations	Reference
20040929	154208.5	40.795	29.051	9.6	104	This study
20040929	154207.0	40.784	29.036	14.0	29	BDTİM
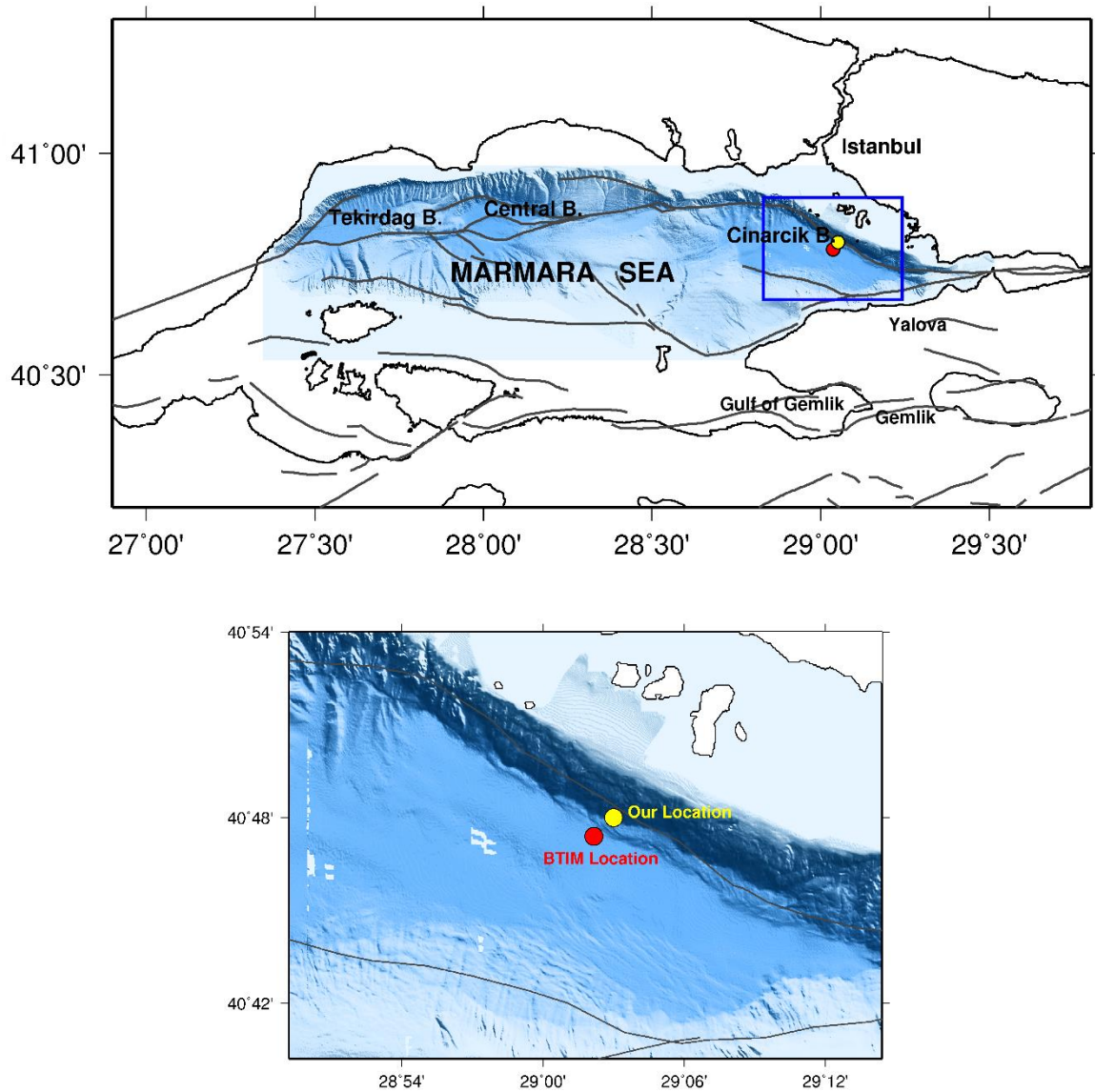
Figure 5.7. Event location, yellow circle (from this study) and red circle (from BDTİM)

5.4. Fault Plane Solution of Reference Event

5.4.1. Conventional Approach (First Motion Method)

Focal mechanism of an earthquake can be found with accuracy if it is recorded by a sufficient number of seismic stations at various distances and azimuths. Focal mechanism solution provides two nodal planes where only one corresponds to the true fault plane. There exist in general an ambiguity to know which one corresponds to the real fault plane. It is important to identify correct fault planes to constrain the regional geodynamic models and stress fields (Zahradnik *et. al.,* 2008). Fault plane solution for our reference event is performed using SEISAN (Haskov and Ottemöller, 1999) software package. Azimuth of seismic stations which recorded the earthquake varies in a wide range, between $2°$ -$359°$, and the take-off angles between $99°$ -$126°$. A total of 103 P polarity readings are obtained from both KOERI national network and the RR stations. First arrival polarization was difficult to identify, especially when the station is located close to the nodal plane. According to the obtained focal mechanism solution (Figure 5.8) based on polarities only, this earthquake represents right lateral strike slip motion with a significant component of reverse faulting (strike 105°, dip 74.19°, rake 98.31° for Fault Plane1 and strike 256.44°, dip 17.84°, rake 62.98° for Fault Plane2).
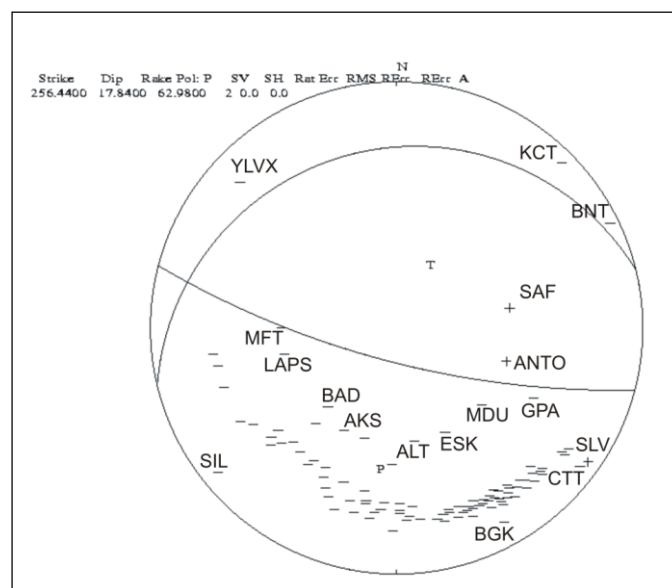
Figure 5.8. Conventional focal mechanism solution.

5.4.2. Amplitude based Method

In addition to conventional methods based on the determination of first motion of P, a more detailed analysis is performed using the amplitude. This method is based on analysing body wave radiation patterns not only in terms of polarity and but also using amplitude information. In the following we explain the procedure that helps to determine the amplitudes for P and S arrivals.

We first determine the time duration of time window, which corresponds to the source time function of the event. A clear impulsive waveform is observed nearly for all arrivals at station closer than 100 km. The time duration of this impulse is 0.3 s and corresponds well to the source time function of the event. We also note that this duration corresponds well to an event of size Ml=4.1. Since the arrival times are already picked, we select a time window of 0.4 sec corresponding phase arrival. We filter the higher frequencies and read the amplitude. We use the vertical component for the P-wave amplitude and the transverse component for the SH wave amplitude.

We then apply an exhaustive search approach to find the optimal fault plane parameters which best fit the P and SH waves polarity and amplitudes. We do this in two steps: first we narrow the search range by searching for solutions that only fit the polarities, at second step we then do a finer search in this restricted range using this time the amplitude values. The P wave vertical component records have downward first motion for all the azimuth range covered by the RRS network, whereas SH wave transverse component records have downward first motion at the azimuth between 288°-359° and upward first motion at the azimuth between 359°-71°. We find the best fitting radiation pattern by scanning all possible values of the fault parameters, namely in the range of -180°-180° for strike, 0°-90° for the dip, 0°-360° for the rake angle. We first tried to obtain possible fault plane parameters in terms of polarity consistency between for both P and SH phases. We therefore obtain a set of possible FPS ranges, which satisfy the polarity criteria only, which are displayed in Table 5.4.

Table 5.4.Focal mechanism parameters

Slip angle (º)	Dip angle (º)	Strike angle (º)
-16	15	190
-30	17	180
0	15	200
108	90	112
135	5	305
145	5	310
175	10	330
180	5	340

Next, we carry out a finer search about this set of range, this time taking into account not only polarity but also the true amplitude values. In this step, the radiation pattern is calculated theoretically and optimal fault plane parameters are searched comparing the real and the theoretic values of the amplitudes. At that stage, we make use of the P and S_H radiation pattern relations given in (Lay and Wallace, 1995) following equations:

$$
\begin{aligned}
R^P = & \left[\cos\lambda \, \sin\delta \, \sin^2 i_\xi \, \sin2(\phi - \phi_s)\right] - \left[\cos\lambda \, \cos\delta \, \sin2i_\xi \, \cos(\phi - \phi_s)\right] \\
& + \left[\sin\lambda \, \sin2\delta \left(\cos^2 i_\xi - \sin^2 i_\xi \, \sin^2(\phi - \phi_s)\right)\right] \\
& + \left[\sin\lambda \, \cos2\delta \, \sin2i_\xi \, \sin(\phi - \phi_s)\right]
\end{aligned}
\tag{5.1}
$$

$$
\begin{aligned}
R^{SH} = & \left[\cos\lambda \, \cos\delta \, \cos i_\xi \, \sin(\phi - \phi_s)\right] + \left[\cos\lambda \, \sin\delta \, \sin i_\xi \, \cos2(\phi - \phi_s)\right] \\
& + \left[\sin\lambda \, \cos2\delta \cos i_\xi \cos(\phi - \phi_s)\right] \\
& - \left[1/2\sin\lambda \, \sin2\delta \, \sin i_\xi \, \sin2(\phi - \phi_s)\right]
\end{aligned}
\tag{5.2}
$$

where strike ϕ_s, dip δ, rake λ, take off angle i_ξ and azimuth ϕ from the source to each receiver are the variables to be scanned for finding the optimal FPS. The strike, dip and rake are scanned between the ranges given in Table 5.4. The azimuth and take off angle are the two parameters that identify the ray path. The takeoff angle is the angle, which the ray makes with the vertical line when leaving the source. Each azimuth-takeoff angle combination prescribes a unique path connecting each source receiver pair, and therefore need to be determined independently for each station.

In general, both azimuth and takeoff angle for each station can be taken directly from the hypo71 output files. However we have used a more elaborate approach for achieving a higher accuracy. In our case, the azimuth is well constrained as often the case when there is a good coverage of station around the source. On the other hand the takeoff angle is more dubious because it has a higher sensitivity to the event depth and to the velocity model, which are both loosely constrained. Furthermore, the discrete nature of the velocity structure leads to a takeoff angle which have only a limited set of values. In our situation where all the RR stations are located within a distance range of 15-35 km, all take off angles will assume only one of two possible values, which we think is too simplistic to reflect the reality. We therefore reestimate the takeoff angle using a smoothed version of the angle-distance relationship. An empirical relation is obtained by fitting a second order polynomial to the distance and takeoff angle values given by the relocation procedure. This polynomial is given below:

$$i_\xi = 0.041(distance^2) - 2.9(distance) + 150 \qquad (5.3)$$

Figure 5.9 illustrates the angle-distance pairs together with the curve representing the polynomial fitting.
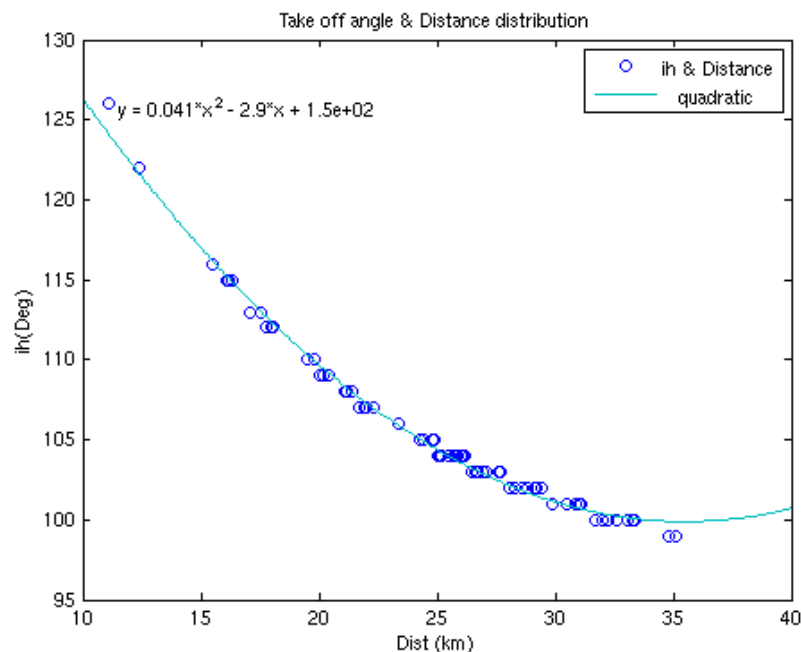
Figure 5.9. Takeoff angle-Distance Distribution.

In the context of expressing amplitudes on a focal sphere; stereographic projection is used to project the focal sphere onto the equatorial plane. In stereographic projection, the distance to the center of the equatorial circle is expressed by tan $(1/2i_\xi)$, where i_ξ is takeoff angle. In the case of i_ξ is greater than 90°, which means that rays is oriented upward and intersects the upper hemisphere of the focal sphere, these should be projected onto the lower sphere. This is done by adding 180° to station azimuth (Figure 5.10). Meantime, takeoff angle correction should also be done by subtracting i_ξ values from 180°. We had to perform both azimuth and takeoff angle correction in our analysis because take of angles were greater than 90° for most stations, varying between 99°-126°.

Figure 5.10 and 5.11 represents the amplitude distribution of RR network only, for the P-wave and SH wave respectively. The top-left box in both figure shows the location of the station in blue colored cross signs. We observe that for this particular event, which is close to the RRS network, the stations show a very dense azimuthal distribution and cover nearly the total lower part of the equatorial plane. Accordingly, P and SH wave amplitudes distribution in terms of azimuth is observed with a very high detail. The box on top-right shows the real P wave amplitudes, which have negative (downward) polarity. The box on the bottom-right of Figure 5.10 shows theoretical P wave amplitudes. They have also negative –downward polarity. Lastly, the consistency of normalized real and theoretical P wave amplitudes are presented in the box on the bottom-left. In a similar way, the SH wave amplitudes obtained directly from real data are shown in the box on top-right of Figure 5.11. The box on the bottom-right shows theoretical SH wave amplitudes. Real and theoretical SH wave amplitudes have both positive–upward and negative- downward polarities depending on the azimuth. At a certain azimuthal range, their polarities is flipped and this corresponds to either the fault plane or the auxiliary plane. Lastly, the box on the bottom-left shows the consistency of real and theoretical SH wave amplitudes. Note that in all these representations the amplitudes are normalized before minimizing the misfit error.

Scanning all values of the strike-dip-rake within the coarsely determined interval in the first step, we find the solution which best fits the data in least square sense. The solution is shown in Figure 5.12 and gives a right lateral strike slip in agreement with the NAF (strike 112°, dip 90°, and rake 108° for Fault Plane1 and strike 200°, dip 18°, rake 0° for Fault Plane2). We also observe that for this improved solution the strike direction (strike 112^oN)

is also in agreement with the strike of the NAF, which locally follows the northern boundary of the Çınarcık basin. In remaining part of this thesis we use this improved version of the FPS.

Observe that this new improved solution is significantly different from the FPS obtained by conventional method (first motion approach) shown in Figure 5.13. The main difference is the addition of a reverse component in the conventional one. However the misfit of the SH amplitude for the conventional method is clearly not negligible. The Figure 5.14 shows the amplitude distribution for the solution obtained by BDTİM solution. One can clearly see that this last solution has a total misfit in terms of both P and SH wave amplitudes.
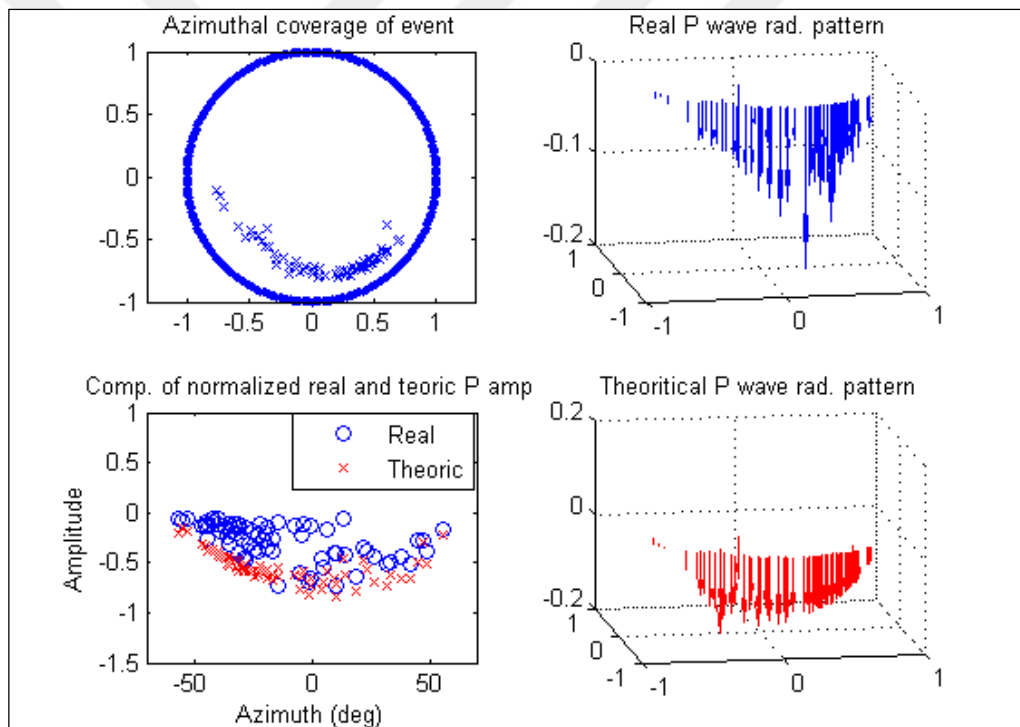
Figure 5.10. Comparison of P wave radiation amplitude patterns.
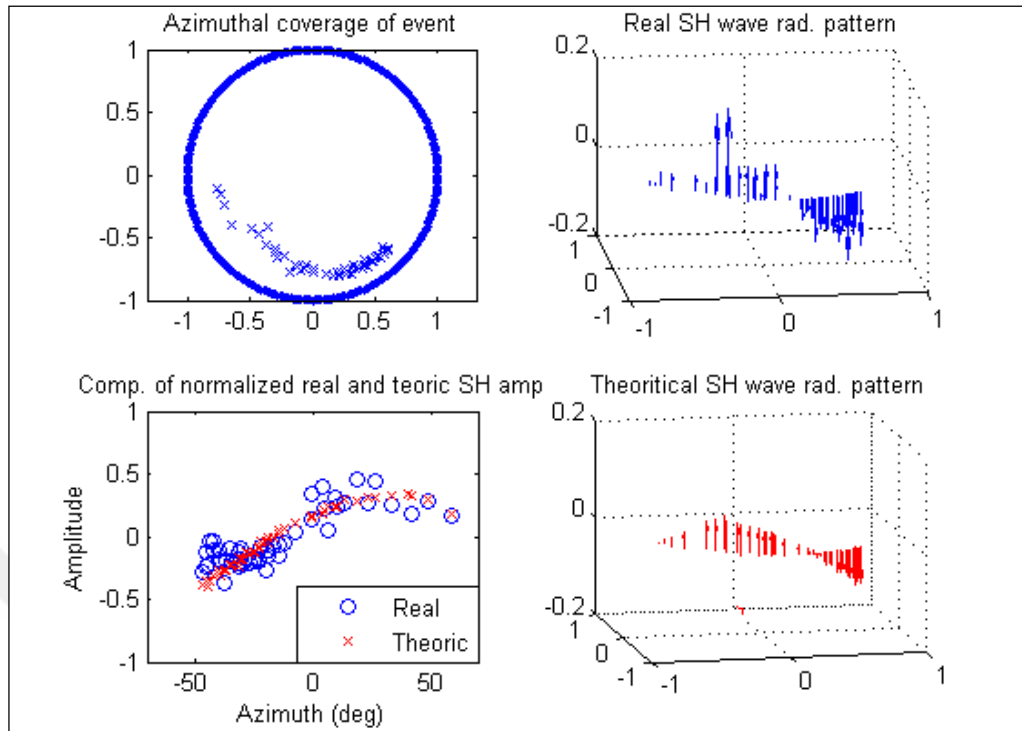
Figure 5.11. Comparison of SH wave radiation amplitude patterns.
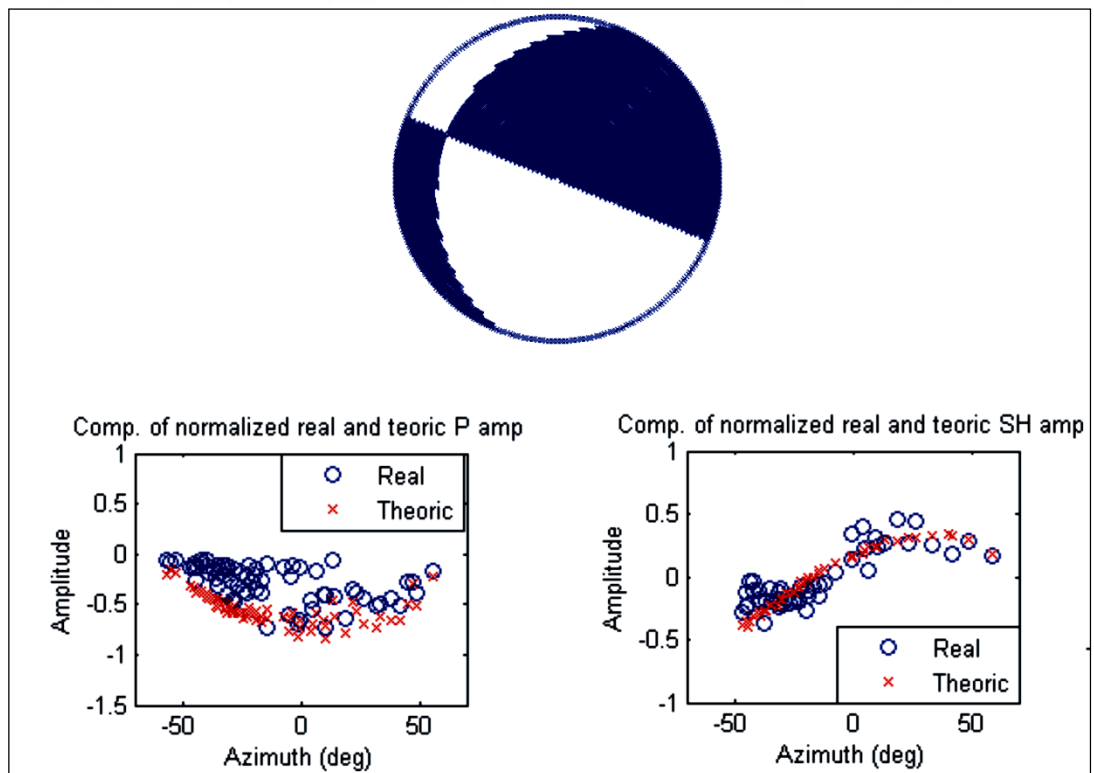
Figure 5.12. Optimal focal mechanism solution.
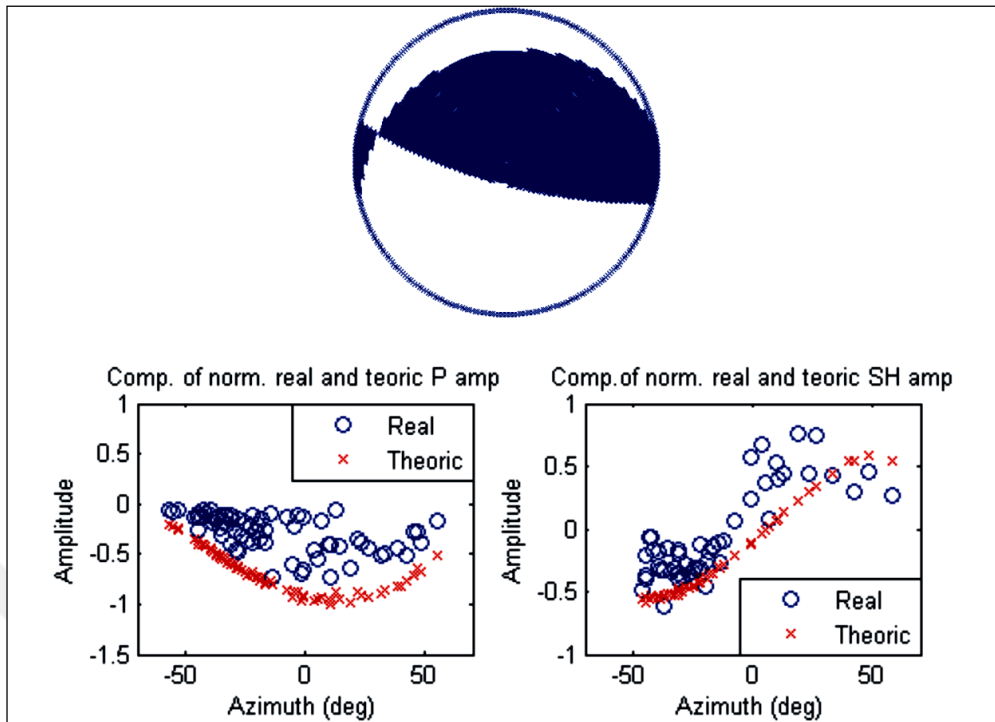
Figure 5.13. Conventional focal mechanism solution.
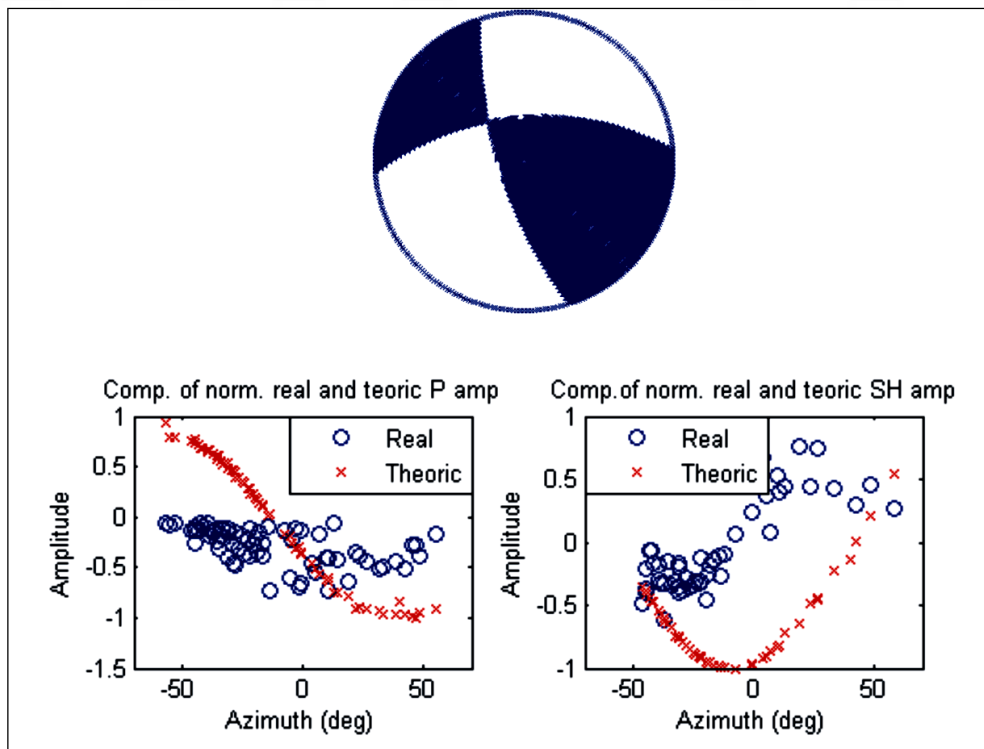
Figure 5.14. Focal mechanism solution from BDTİM.

6. RESULTS FROM 3D MODELLING OF 29, SEPTEMBER 2004 EARTHQUAKE

Simulations of seismic waves from a local earthquake and comparison with true seismograms form the second part of the thesis. The main focus is to investigate first how well the 3D velocity model predicts the observed waveforms and second how much improvement is achieved over the 1D model. The tests provide a validation for the 3D velocity model proposed in this thesis. It also serves to identify parts of the model that may be improved in the future. As mentioned earlier in the thesis, accurate source parameters, reliable crustal model and available algorithm are the critical issues to improve the resolution of modeling for the seismic wave propagation.

Throughout the study, we applied the finite difference method and WPP algorithm outlined in Chapter 3, to our 3-D velocity model, which is introduced in Chapter 5. We simulate the seismic wave propagation for the case of the Cinarcik earthquake of 29, September 2004. The source parameters (location, depth, seismic moment, strike, dip and rake) of this earthquake were obtained reliably using methods explained in Chapter 4. In this chapter the real and the simulated data are compared in detail, and using both qualitative and quantitative criteria. The results in general give a clear evidence both for the accuracy of the numerical method, and also the crustal model that we have developed. We also show that the improvement in waveform fit achieved by 3-D model with respect to 1D model is quite significant.

6.1. Computational Model Parameters

Cinarcik earthquake of 29 September 2004 was used as the seismic source. Simulations were done with the WPP code. Simulations were performed on parallel computers operated by ITU High performance computing center. We simulated wave propagation in a total volume of 63.5 x 36.6 x 20 km, with a grid spacing of 100m, which allowed us to resolve frequencies up to 1.57 Hz without any loss of quality. Our experience showed however that the frequency rendition went to much higher frequency possibly to as

much as 10 Hz. Mesh refinement property of WPP code is also used to achieve finer resolution at the surface where the wave speed is small, while keeping the computation load at an acceptable level. We have chosen two a refinement interfaces, $z_1=1000m$ and $z_2=3000m$ (Figure 6.1).
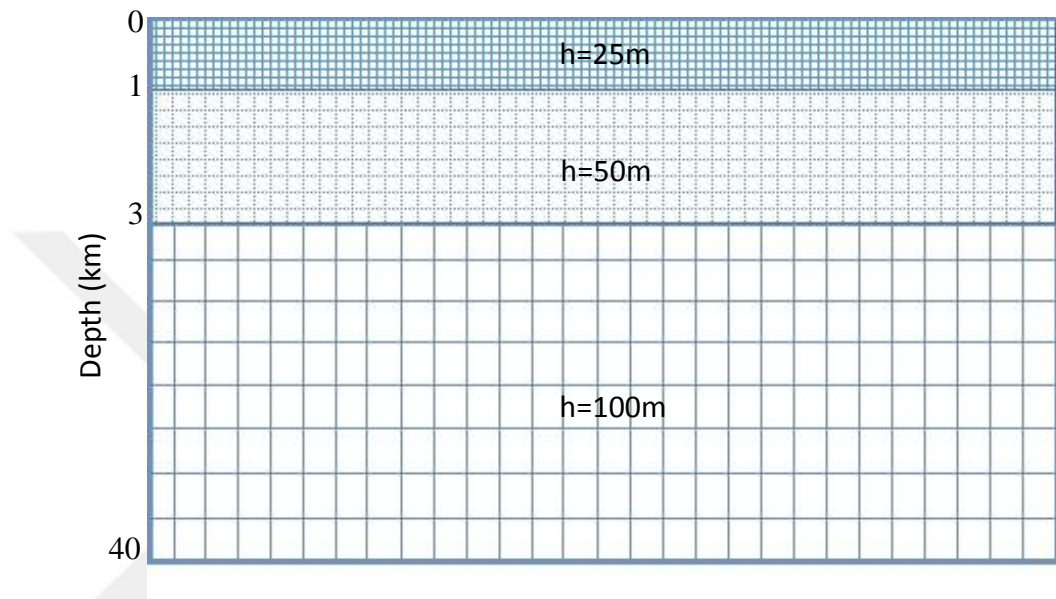
Figure 6.1. Cartesian component grids with two mesh refinement interfaces.

As explained in earlier chapters, the grid refinement consists of reducing the grid size at specific levels, as we go shallower into slower layers. The coarsest grid size (also called base grid) is chosen as 100m and covers the bottom of the computational domain between 3000-40000m. The next grid size is half of the base grid (50m) and covers the depth between 1000 and 3000m. The finest grid size is chosen by reducing by another factor of two giving h=25m. This covers the shallowest structures of the computational domain, between 0-1000 m, where the velocities are the lowest. All computational parameters used in the simulations are summarized in Table.6.1. Velocity model and computational domains are illustrated in Figure 6.2. Note that our computational domain (dashed box in Fig. 6.2) has nearly reached the size of the velocity model (black box in Fig. 6.2).

Table 6.1. Parameters for the Finite Difference Simulations.

Parameter	Value		
Minimum S-wave velocity	222 m/sec		
Minimum P-wave velocity	424 m/sec		
Base grid spacing	100 m		
Mesh refinement properties	2 interfaces with 1000m and 3000m		
Dimensions of domain (km)	63,5 by 36,6 by 20 km		
Dimensions (grid points)	h=100	636 by 367 by 171	
	h=50	1271 by 733 by 41	
	h=25	2541 by 1465 by 41	
Total number of grid points	2.30736×10^8		
Total time of simulation	30 sec		
Time step	0.00323974 sec		
Total number of time steps	9260		

6.2. Comparison of synthetic and real data

In this section we report the comparisons of the observed three-component waveforms with synthetic seismograms computed using the new 3D model. The waveforms were all low pass-filtered at 1.4 Hz cut-off using 2-poles Butterworth filters, with one-pass operation. Comparisons are performed in two ways. First one is the direct waveform comparison in terms of amplitudes, waveform shapes and delay times for the stations located in both European and Anatolian parts of the İstanbul. This approach is applied for stations that are located on hard rock sites and therefore provides single pulse waveforms with no oscillations. The second approach is mainly applied to the stations which are located on soft sediments. These are characterized by sustained oscillations of the shallow layers and therefore a direct comparison in time domain is not practical. In this situation, we find that the spectral comparison is more useful. We therefore show the spectrum of the seismograms together with the time domain signal. In this case, the comparison of spectral behavior is based mainly on comparing the spectral peaks, which essentially represent the effect of the

oscillating layers. In these cases, we pay special attention to the frequency and amplitude of the spectral peaks.
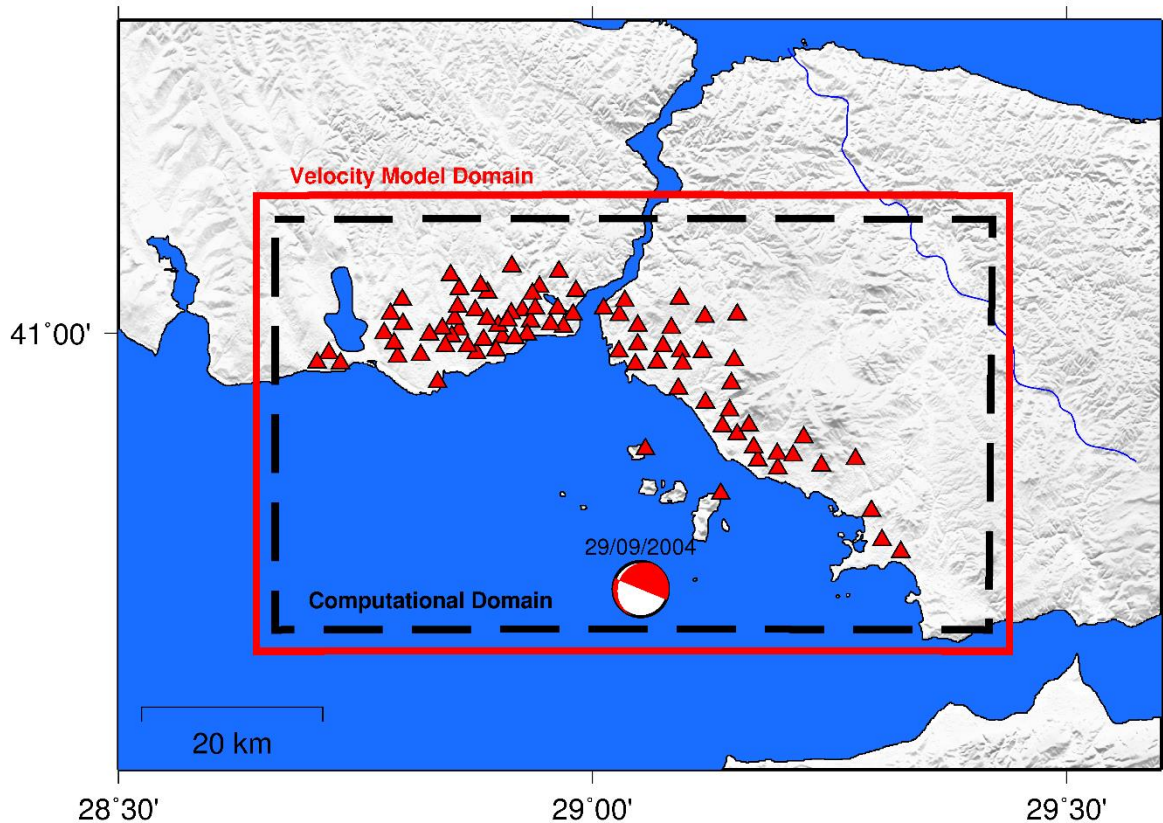
Figure 6.2. Velocity model (red rectangle) and computational (black rectangle) domain using in finite difference simulations.

6.2.1. Direct Waveform comparison

The main focus of this section is to evaluate how much the 3D synthetic fits the real data. However, when evaluating the effectiveness of 3D model, we also found it useful to compare it not only with the real data but also with the 1D counterpart. The 1D model used is the modified version of Karabulut *et al.* (2002), which is explained in earlier chapters. The same finite difference code (WPP) was used to generate both the 1D and the 3D synthetics. The results of the comparisons are presented in Figure 6.3-6.7. In each case, the vertical, NS and EW components of the seismograms are shown, for both the real and the synthetic

waveforms. In all figures, amplitudes are always normalized to a unique scale on a station basis.

When we compare the 1D and 3D synthetics, we can see that they are quite different in terms of waveform shape and amplitudes, especially for the late arriving phases. However, polarities of first arrivals always show good agreement for both 1D and 3D synthetics. It should be noted that in 1D case we observe higher amplitudes for S and later phases than the 3D case for some stations located in the Anatolian part (R25, R53, R69, R79 and R80). It arises from inserting high velocity structure showing hard rock characteristics into 3D model for this region generally.

The amplitudes and the shape of the main pulse in 3D shows better fit to real data for many stations (R04, R07, R09, R11, R25, R45, R63, R64, R69, R79, R80, R88, R89, R91, R92, etc.) as compared to 1D synthetics. Note that we observe a moderately good fit even for some waveforms, which show complex shapes and large amplitudes for S and later phases (R03, R07, R26, R45, R63, R64, R88, R89, and R91). There are cases where 3D synthetic amplitudes do not fit well to real data, although arrivals are well predicted (R01, R02, R08, and R15).

A general inspection of the real and 3D synthetic waveforms shows that the phase arrivals have better timing compared to 1D synthetics, in particular for the S-waves. The error in P and S arrivals generally does not exceed 0.1 and 0.15 s, respectively, as will be analysed in more detail later in this chapter. We find that the 3D synthetic predicts quite efficiently the late arrivals in the Bakırköy Formation in the European part (R07, R45, R50, R64, R91, etc.) thanks to the low velocities at shallow zones. We also observe some early arrivals relative to real data for some stations in the Anatolian part (R53, R79, R80 and R92) and also in Avcılar distinct in the European part (R04, R88, R89). This early arrivals originates from high velocities in 3D model for these regions and indicate the need of more low velocity layers in the model.

The real data at stations R19, R23, R24, R43, R86 and R98, on the European part, show some different characteristics from the other stations. We observe that there are no oscillations in these waveforms. We observe a similar behavior in nearly all of the stations

located in Anatolian part. The main explanation of this is the fact those stations are located on hard materials consisting of sandstone (greywacke), siltstone or claystone of Paleozoic Age. This is in agreement with Birgören *et.al.* (2008), who mapped the distribution of sedimentary cover thickness and found that hard rock sites are common in most part of Anatolian part and Golden Horn. Accordingly the 3D model includes very small or even no low velocity shallow layers in these locations. As a consequence the 1D and the 3D synthetics are quite close to each other.

The stations that are outside this hard rock zones are mostly clustered on the western European part extending from Yedikule to Avcılar. The real data provide oscillatory signals which points to deep sedimentary cover. A time domain comparison of these oscillatory signals is not practical, we therefore prefer to look at them in frequency domain. These stations with oscillatory character are analyzed in the next section.
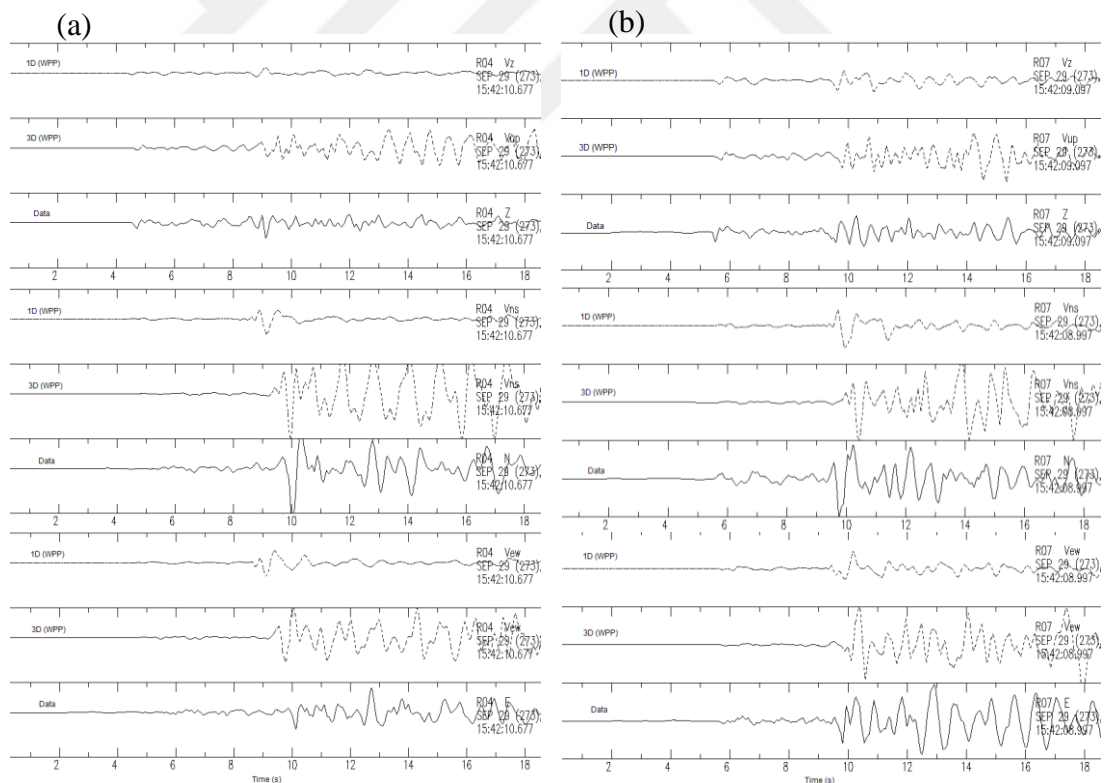
Figure 6.3. Comparison of three component 1D and 3D synthetics with real data for 29 September 2009 earthquake at stations R04 (a) located in Avcılar and R07 (b) located in Sefaköy.

Figure 6.4. Comparison of three component 1D and 3D synthetics with real data for 29 September 2009 earthquake at stations R09 (a) located in Kadıköy, R11 (b) located in K.Bakkalköy, R19 (c) located in Fatih and R25 (d) located in Maltepe.
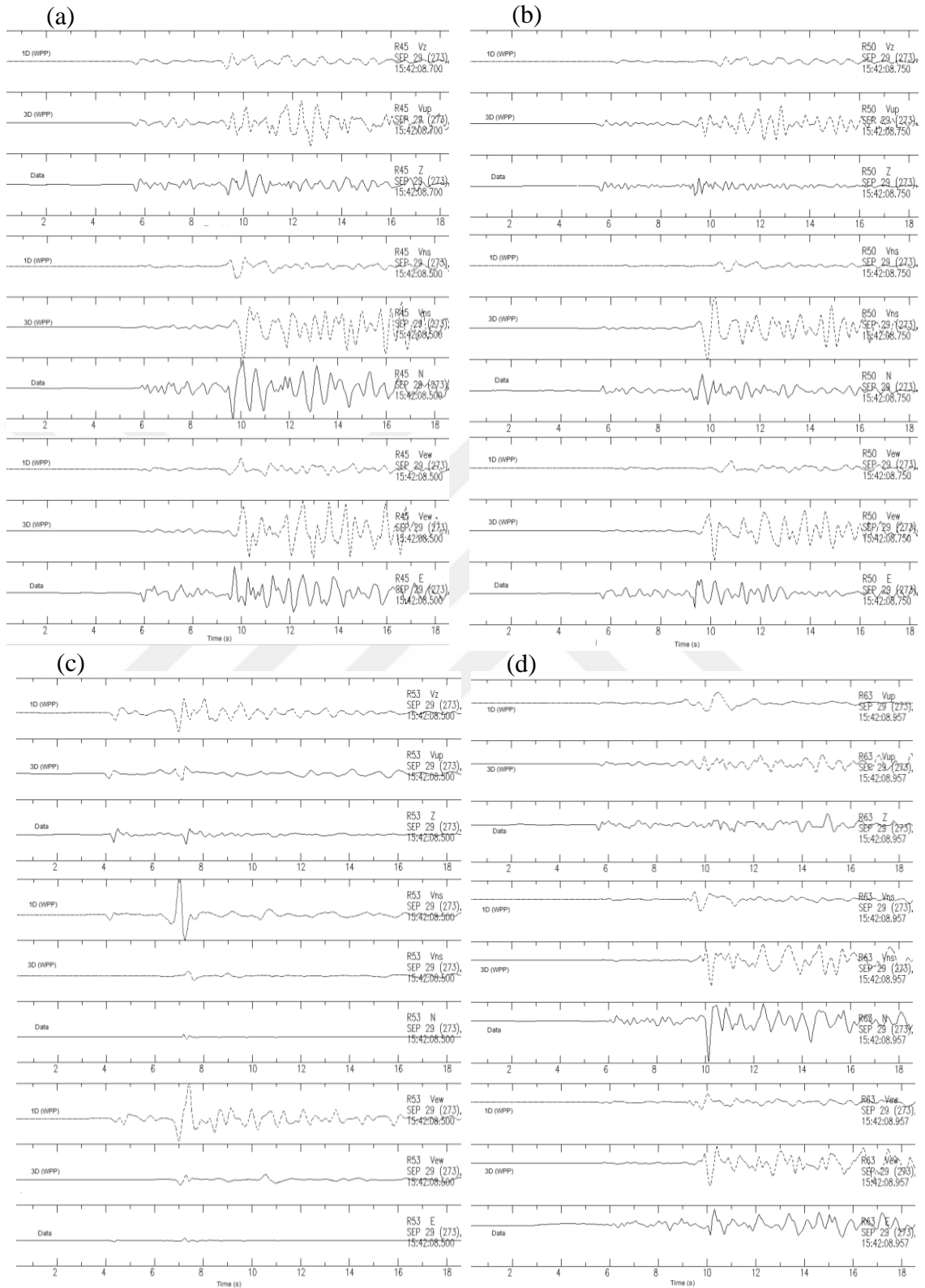
Figure 6.5. Comparison of three component 1D and 3D synthetics with real data for 29
September 2009 earthquake at stations R45 (a) located in B.evler, R50 (b) located in
Esenler, R53 (c) located in Kadıköy and R63 (d) located in K.Çekmece.
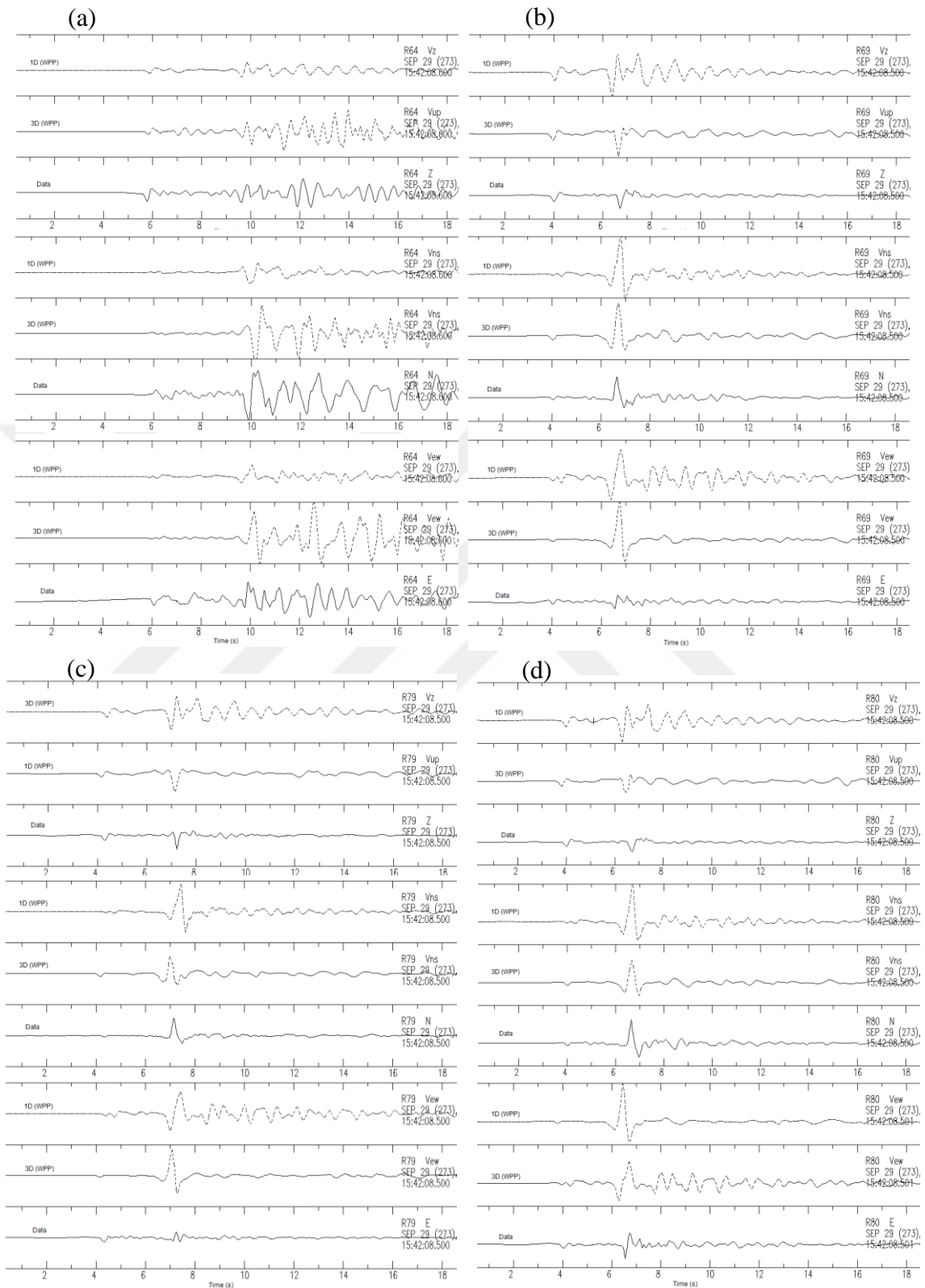
Figure 6.6. Comparison of three component 1D and 3D synthetics with real data for 29 September 2009 earthquake at stations R64 (a) located in Bağcılar, R69 (b), R79 (c) and R80 (d) located in Maltepe.
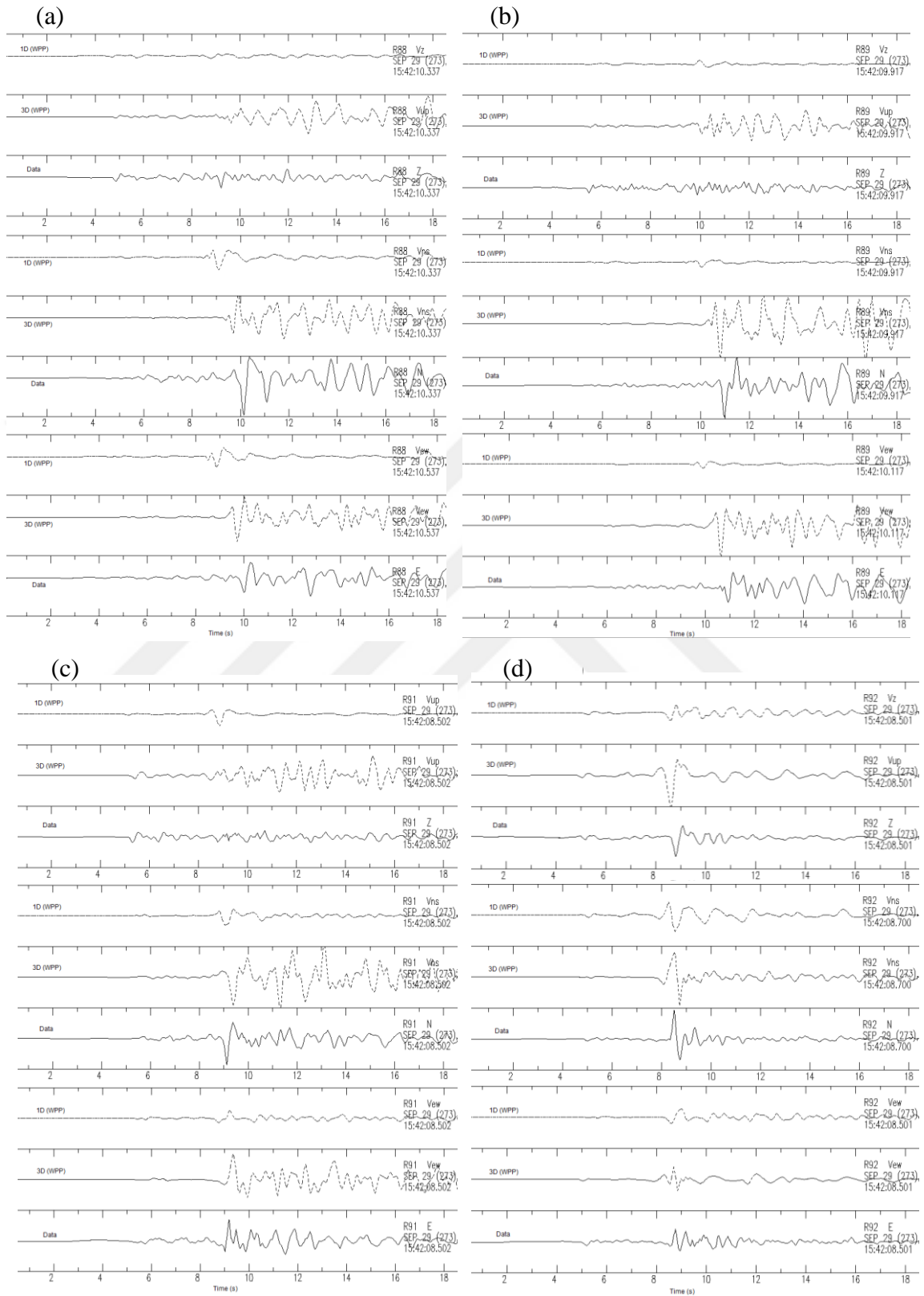
Figure 6.7. Comparison of three component 1D and 3D synthetics with real data for 29 September 2009 earthquake at stations R88 (a) and R89 (b) located in Avcılar, R91 (c) located in Bakırköy and R92 (d) located in Ümraniye.

6.2.2. Comparison of Amplitude Spectrums

Considering observed and synthetic waveforms obtained from the European site, it is clearly seen that there is high amplitudes oscillations after the S wave. This corresponds mostly to the oscillations of the shallow sedimentary cover, which has a low S-wave velocity. Therefore, it is more practical to compare synthetic seismograms with real ones in terms of their Fourier amplitude spectrums (FAS). As we know that soft sediments are seen generally in the western part of the city of İstanbul, which comprises alluvium to limestone or sandstone. Some of the RR stations cover this area. In the context of the FAS analysis, S-wave window of 5 second was individually extracted from each seismogram, and tapered. In the comparison of the figures, we have also included synthetic waveform from 1D model, which provides a reference for the non-oscillatory behavior.

Some examples of comparison of FAS are presented in figures 6.8-6.13. FAS of synthetic 1D, synthetic 3D and observed ones are given in blue, magenta and black color, respectively. In a general, it can be seen that the real and 3D synthetics have a considerable agreement for the maximum peak frequencies as well as the amplitudes.

In Figure 6.8, we see the FAS comparison of station R01 which is located in Bahçelievler district and Pliocene-Miocene aged Bakırköy formation. We observe that horizontal and vertical components of real and synthetic spectra are consistent to each other. 1D synthetic shows lower amplitudes in all components whereas 3D synthetic shows higher amplitude values. Maximum frequency appears at around 0.7-1.0 Hz for the horizontal components. According to study of Birgören *et al.* (2008), distribution of sediment cover thickness increases towards to Marmara Sea. Especially SW part of the city has thicker sediments (nearly 450m) compared to Asian part. Station R01 is located in a place where the cover thickness is high.
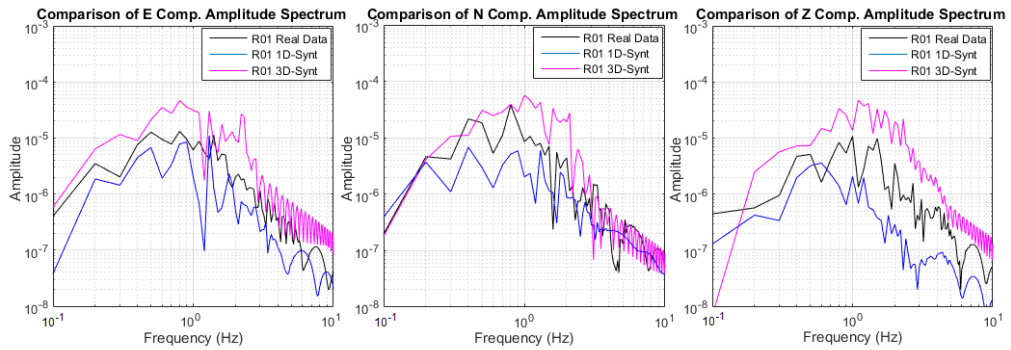
Figure 6.8. Comparison of Fourier amplitude spectra corresponding to horizontal and vertical velocity seismograms for station R01. Three panels represent the E, N and Z components.

In Figure 6.9, we see that the FAS comparison of station R03 which is located in Fatih distinct on Pliocene-Miocene aged Bakırköy formation. We can say that horizontal components of real and 3D synthetic spectra are more consistent compared to vertical component. 1D synthetic shows lower amplitudes in horizontal components whereas 3D synthetic shows higher amplitude values consistent with the real data. This station is placed on the eastern part of the European study region compared to other stations in European site of the city, therefore sedimentary cover thickness is lower (nearly 50-60m according to Birgören *et.al.*, 2008). Maximum frequency appears at around 0.6-0.7 Hz for the horizontal components.
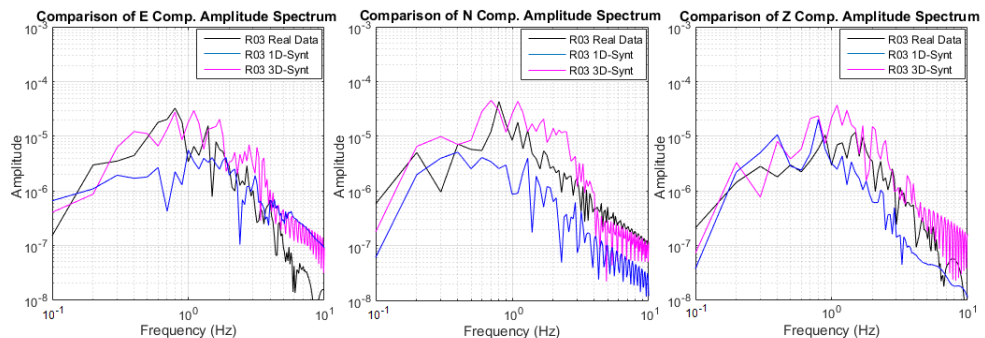
Figure 6.9. Comparison of Fourier amplitude spectra corresponding to horizontal and vertical velocity seismograms for station R03.

In Figure 6.10, we see the FAS comparison of station R41, which is located in Merter district on the Bakırköy formation of Pliocene-Miocene. Sedimentary cover thickness is nearly 150m here according to Birgören *et.al.* (2008). We observe that the real and synthetic spectra are consistent for all components of the 3D model. Maximum frequency appears at around 0.8 Hz for the horizontal components.

Figure 6.10. Comparison of Fourier amplitude spectra corresponding to velocity seismograms for station R41.

In Figure 6.11, we see that the comparison of station R45 which is located in Bahçelievler district on the Güngören formation of Pliocene-Miocene. This figure shows once again that real and 3D synthetic spectra are consistent for all components. 1D synthetic shows lower amplitudes than the 3D synthetics especially for horizontal components. Maximum frequency appears at around 1.0 Hz for the horizontal components.
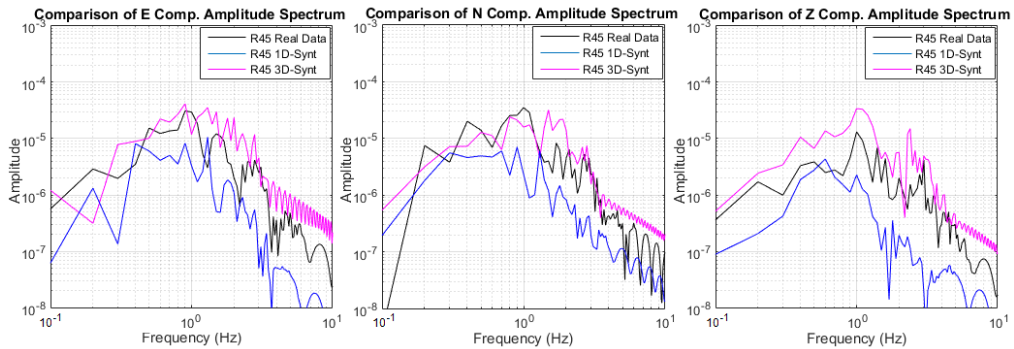
Figure 6.11. Comparison of Fourier amplitude spectra corresponding to velocity seismograms for station R43.

Figure 6.12, shows the comparison of station R63 which is located in Küçükçekmece district of Bakırköy formation. Therefore sedimentary cover thickness is high (nearly 250m according to Birgören *et al.*, 2008). We can say that North and Vertical components of real and 3D synthetic spectra are more consistent compared to East component. Maximum frequency appears around 0.7 Hz for this station at all components.
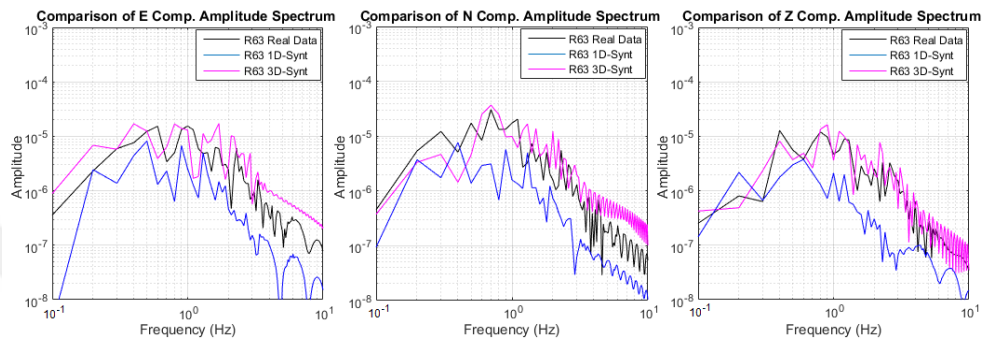
Figure 6.12. Comparison Fourier amplitude spectra corresponding to velocity seismograms for station R63.

Figure 6.13. presents the comparison for station R91, located in Bakırköy district on the Bakırköy formation. We can say that horizontal components of real and synthetic spectra are consistent generally for the real and 3D synthetics. 1D synthetic shows lower amplitudes in all components. Maximum frequency appears at around 0.7 Hz for this station.
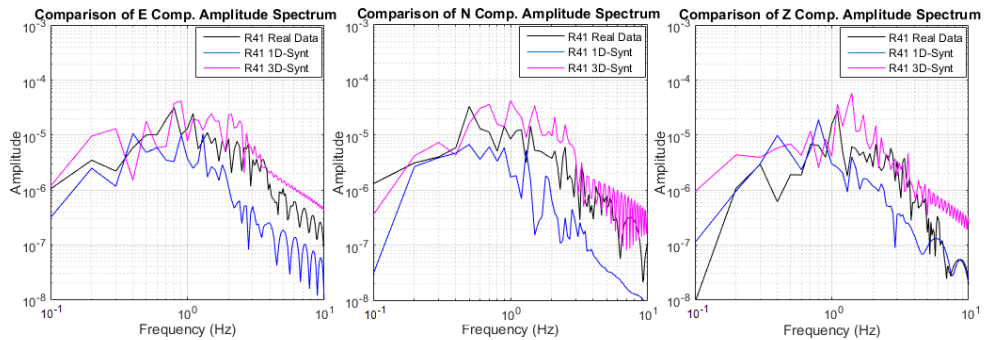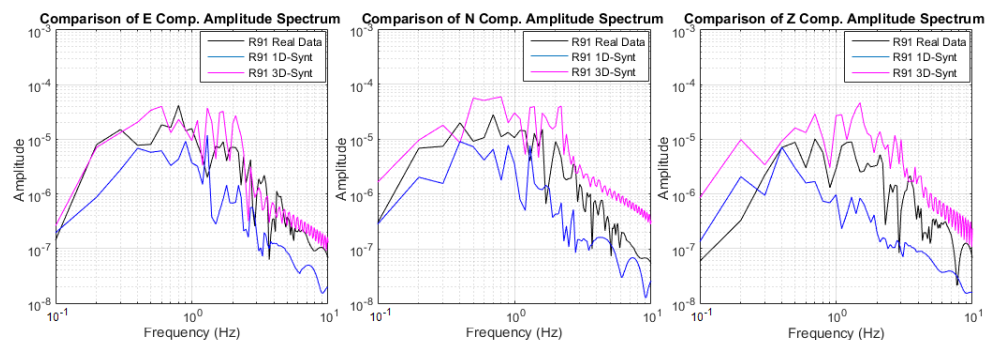

Figure 6.13. Comparison of Fourier amplitude spectra corresponding to velocity seismograms for station R91.

6.2.3. Numerical Comparison

We have also performed an automatic and quantitative comparison of 1D and 3D models, based on the amplitude and the arrival time deviations from the real data. For this purpose, we measured the misfit error between the real and the synthetic waveforms, both for the 1D and 3D models.

Both the real and the synthetic seismograms are band pass filtered before the quantitative comparison. As expected, we observe that lowering the cut-off frequency improves the degree of fitting. On the other hand, there is a limit for the lower cut-off frequency, below which the real data become meaningless, because it does contain enough energy. In other words, considering that the data was recorded mostly on accelerometers (rapid response network) and the earthquake had a magnitude of 4.1, the low frequency part has too small amplitudes to be recorded properly. We therefore do all the testing above this limit, which corresponds to about 0.3 Hz.

First we focus on amplitude differences, for the P-wave and the S-wave. The P-wave window is selected but cutting 0.3 sec before and 0.5 sec after the P-arrival time, from the vertical component of all three seismograms, namely the real, the 1D synthetic and the 3D synthetic. The maximum absolute amplitudes are read automatically from the data. Since in our case, all P-arrivals have downward polarity in the vertical component the maximum amplitudes all have negative values. We find the amplitude error by finding the difference between amplitude of the synthetics and the real wave. The procedure is repeated for 1D and 3D cases. We then compare the two errors. For the S wave amplitude comparison we repeated the same procedure for the P-wave, this time using the horizontal components. For S-wave the window size is selected to be slightly wider the P-wave, namely 0.5 s before and 0.7 s after the S-arrival. The original waveforms are low-pass filtered in the same way as before. The amplitude of the S-wave is found by taking the average of the maximum and the minimum amplitudes (negatively maximum) of the S-wave train. We processed the NS and the EW components separately, and therefore obtained two numerical values from the comparison.

The maximum P and S wave amplitude comparisons of real data and synthetics from vertical and horizontal components of velocity seismograms are presented in Figures 6.14-6.16. In these figures, the amplitude values are expressed in terms of color scale, for 1D, 3D synthetic and real data from top to bottom, respectively.

Additional evaluations are done to provide more quantitative comparison between real and synthetic data in terms of their amplitudes. In this case, the error between synthetic and real data amplitude is examined. We have used the absolute value of the logarithm of the ratio of the amplitudes as the measure of the error size. In this representation, if the real and synthetics fits perfectly each other, the error measure would be zero. Similarly, if one of the amplitude is twice the other, the error measure would give 0.3, regardless of which one is the larger. The distribution of this error measure (i.e. log of amplitude ratio) for P and S waves are given in Figure 6.17. Three figures corresponds to P on the vertical, S on the NS and S on the EW components, respectively. It is clearly seen that data is spread out in a wider range for 1D case with respect to the 3D case. We express this difference more quantitatively using the variance of the error measure. We observe that the error variance for 1D is nearly twice the variance of 3D for the Z-component (0.125 vs 0.053) and for the EW component (0.073 vs 0.039). Considering the logarithmic nature of the error measure, this indicates a significant improvement in amplitudes when using 3D instead of 1D model. The EW component in our case corresponds mostly to the SH arrival due to the geometry of the network with respect to the event location. On the other hand, the NS component corresponds to the SV component, which is often contaminated by P-wave coda, and thus we avoided using NS component in our analysis. In fact, the observation on the NS component did not provided any significant improvement for both amplitude and time errors comparison.
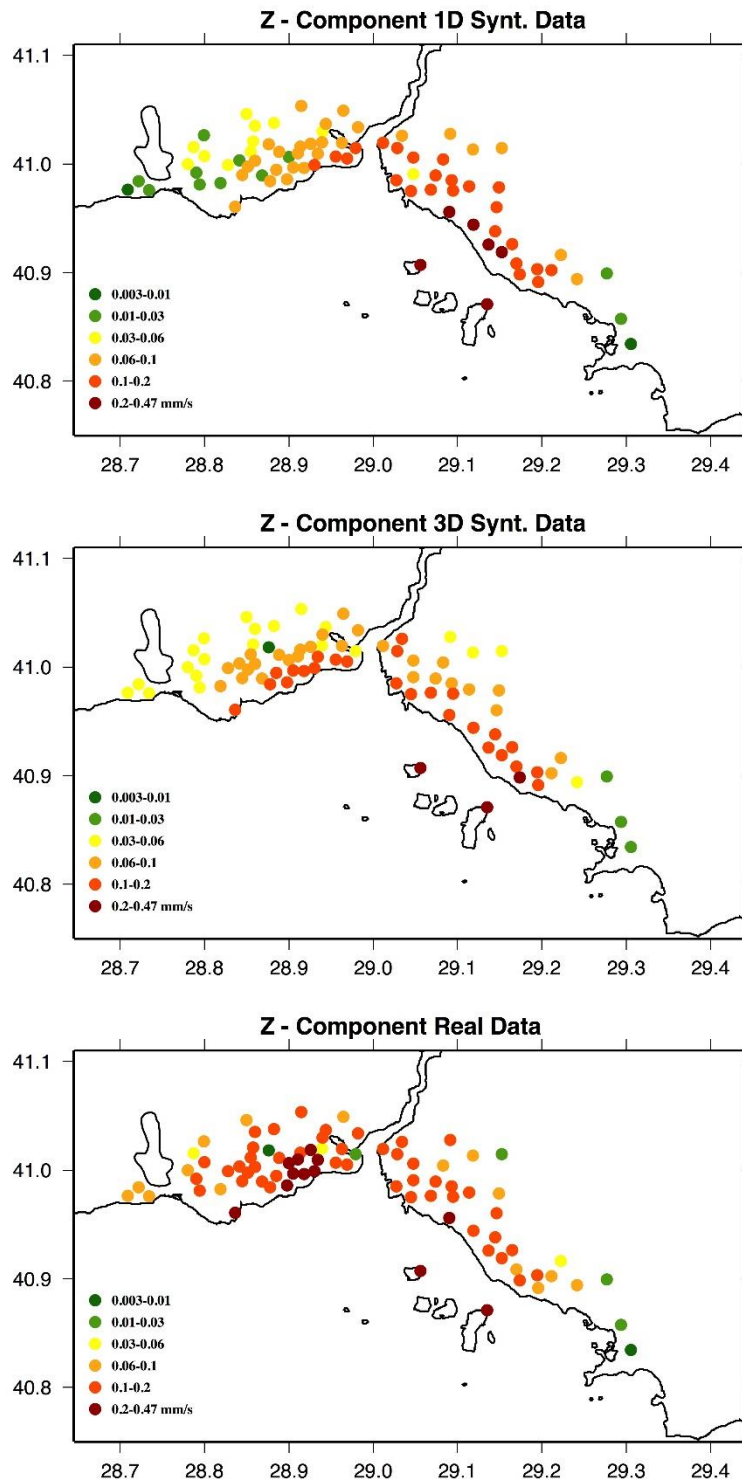
Figure 6.14. Comparison of P wave maximum amplitude values for 1D synthetic, 3D synthetic and real data from vertical component velocity waveforms.
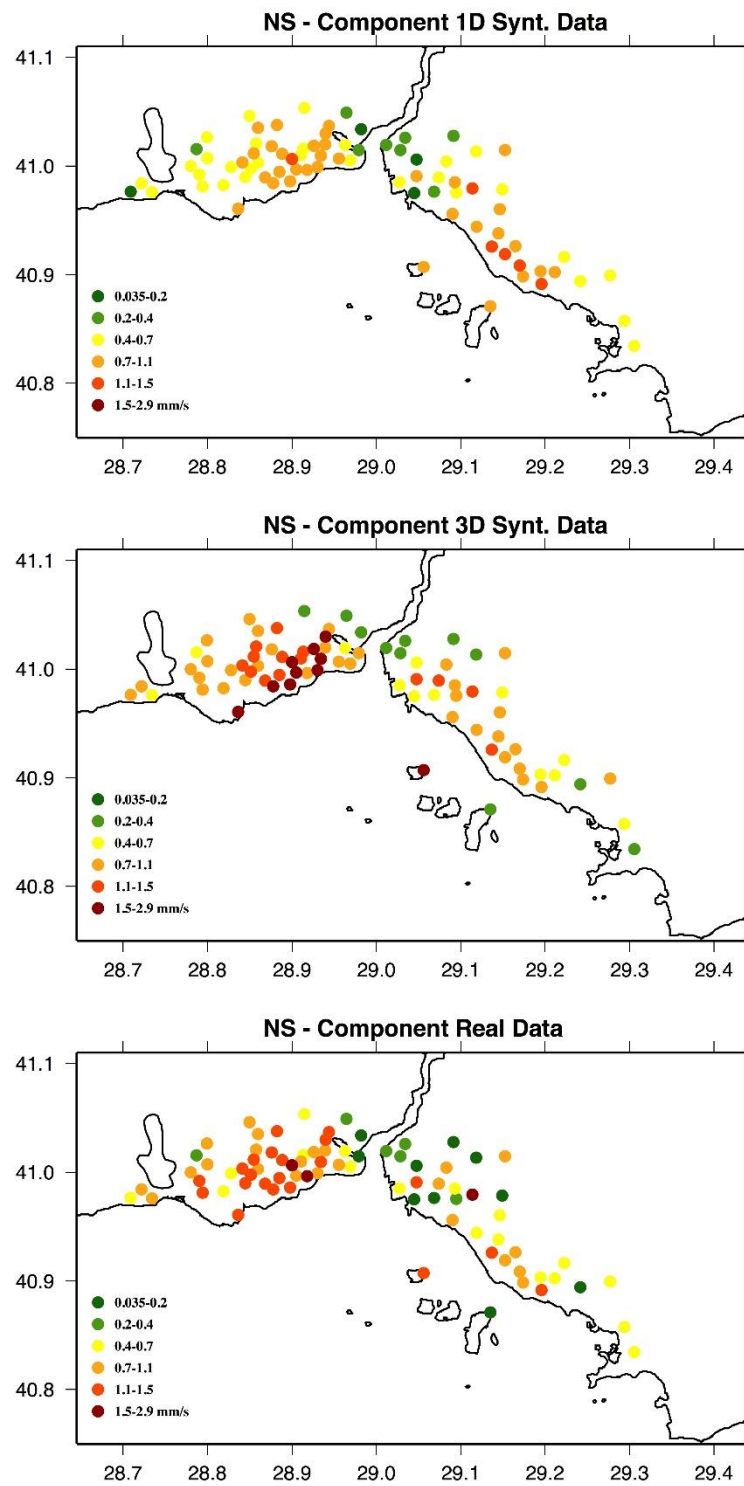
Figure 6.15. Comparison of S wave maximum amplitude values for 1D synthetic, 3D synthetic and real data from NS component velocity waveforms.
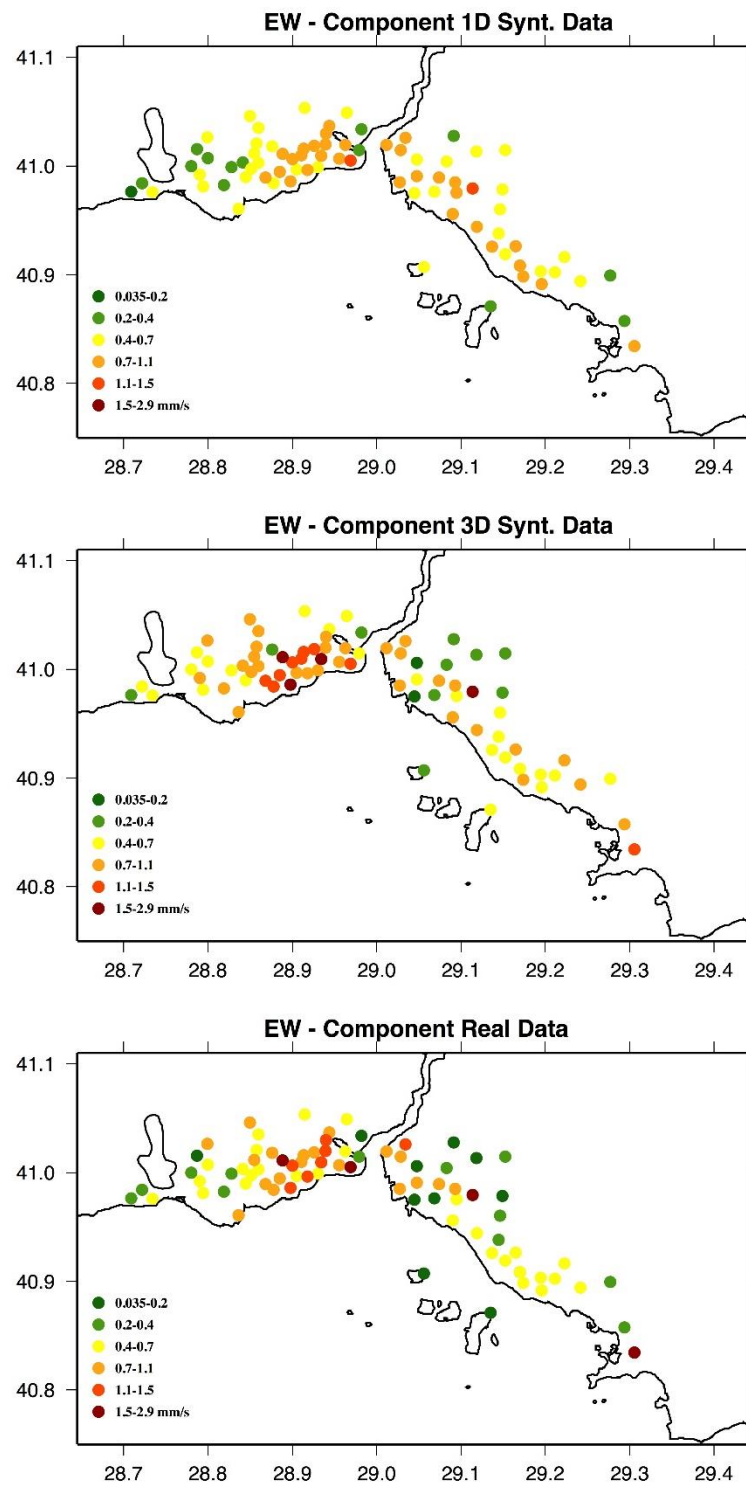
Figure 6.16. Comparison of S wave maximum amplitude values for 1D synthetic, 3D synthetic and real data from EW component velocity waveforms.
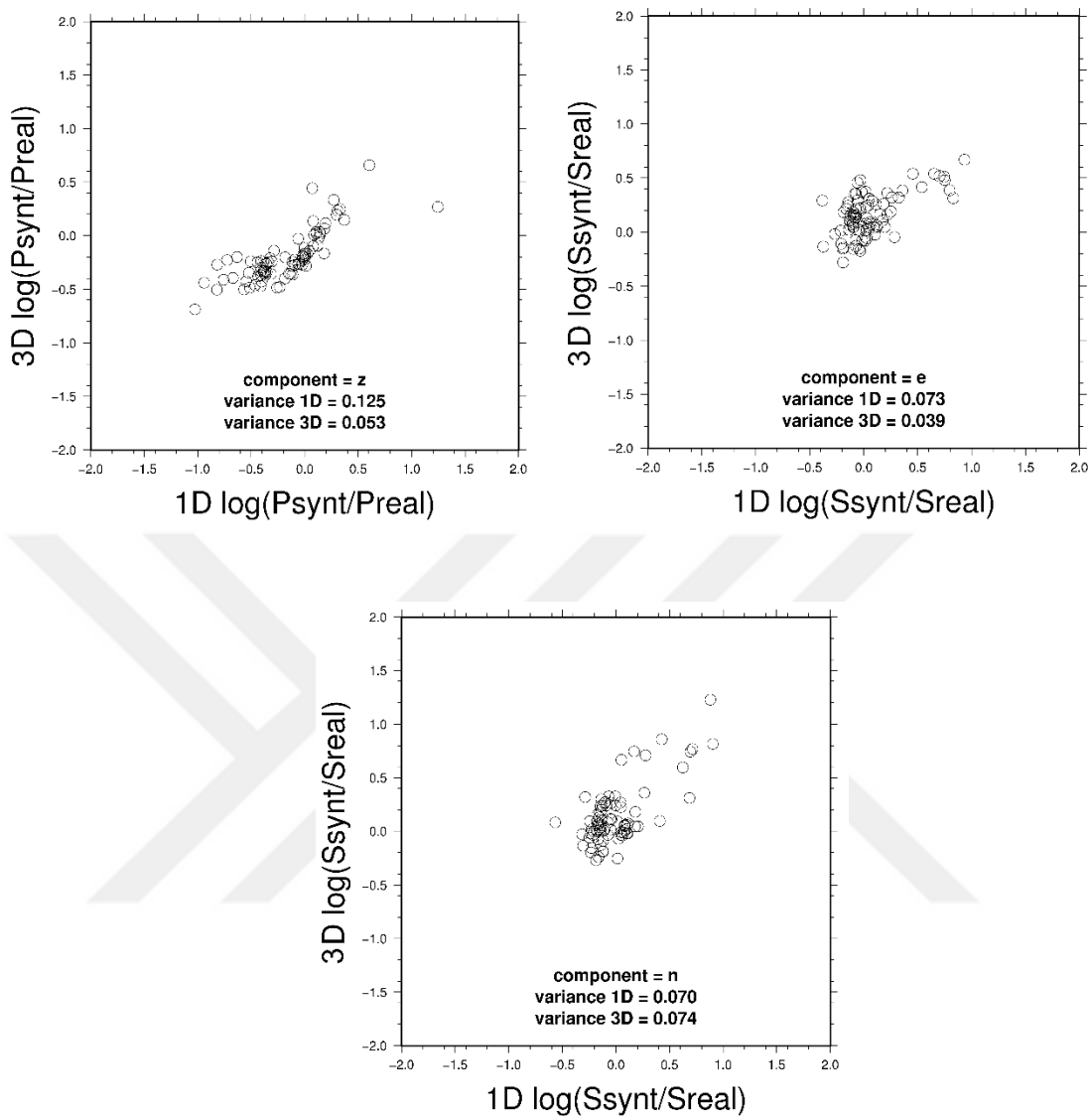
Figure 6.17. Variation of the amplitude ratio (synthetic/real) for 1D and 3D synthetic waveform from vertical and horizontal components.

A similar procedure to the amplitude comparison is applied for the arrival time comparison. As indicated earlier a Butterworth low pass filter of order 2 is first applied to the waveform with a cut-off 0f 1.4 Hz with one-pass. In order to obtain time differences between the observed and the synthetic waveforms, we have extracted 0.3 s before and 0.5 sec after P-arrival time on the vertical component, and 0.5 sec before and 0.7 sec after the S-arrival time on the horizontal components waveforms. The time difference between the real and the synthetic data is found by cross correlation. The same procedure is repeated for the 1D and 3D synthetics. The spatial distribution of the time arrival error is shown from Figures

6.18 to 6.20, corresponding to vertical, NS and EW components, respectively. In these figures, time residuals are represented in color given on the left bottom of each figure. The green-yellow range indicates low error, while red to brick corresponds to larger error. The top figure gives the error for 1D and the bottom figure for 3D, in each case. The comparison P-wave on vertical component indicates more error on the European side with 1D as compared to 3D. For the S-wave, significant improvement is observed with 3D model on the European side, and particularly with the EW component.
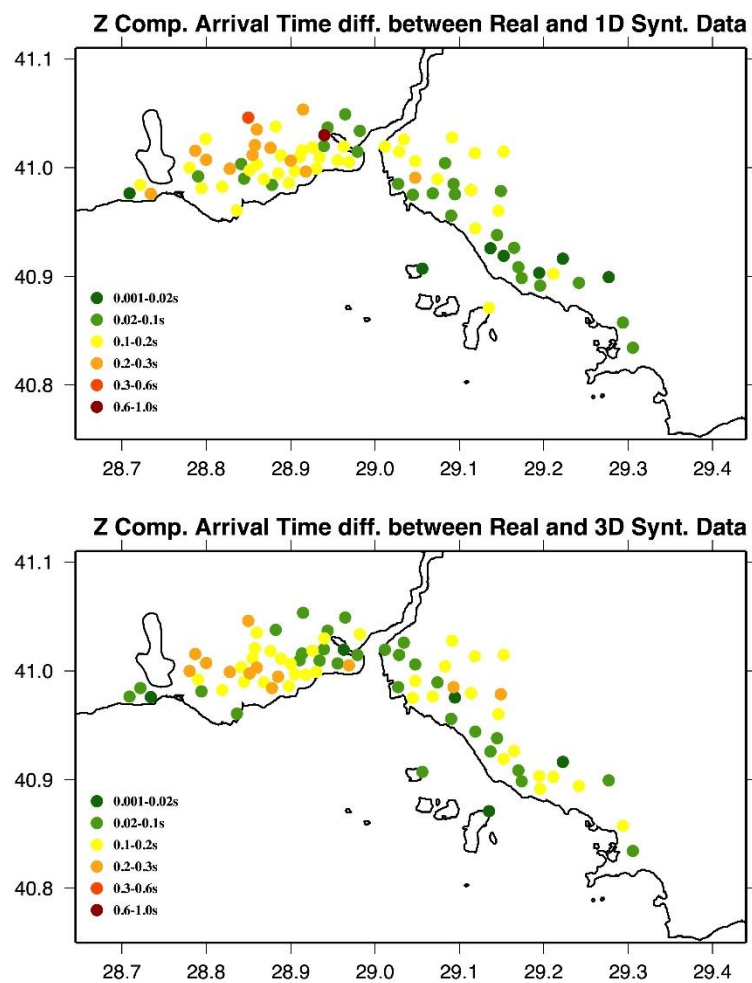
Figure 6.18. P wave time residuals for 1D synthetic to real data and 3D synthetic to real data from vertical component velocity waveforms shown from top to bottom.
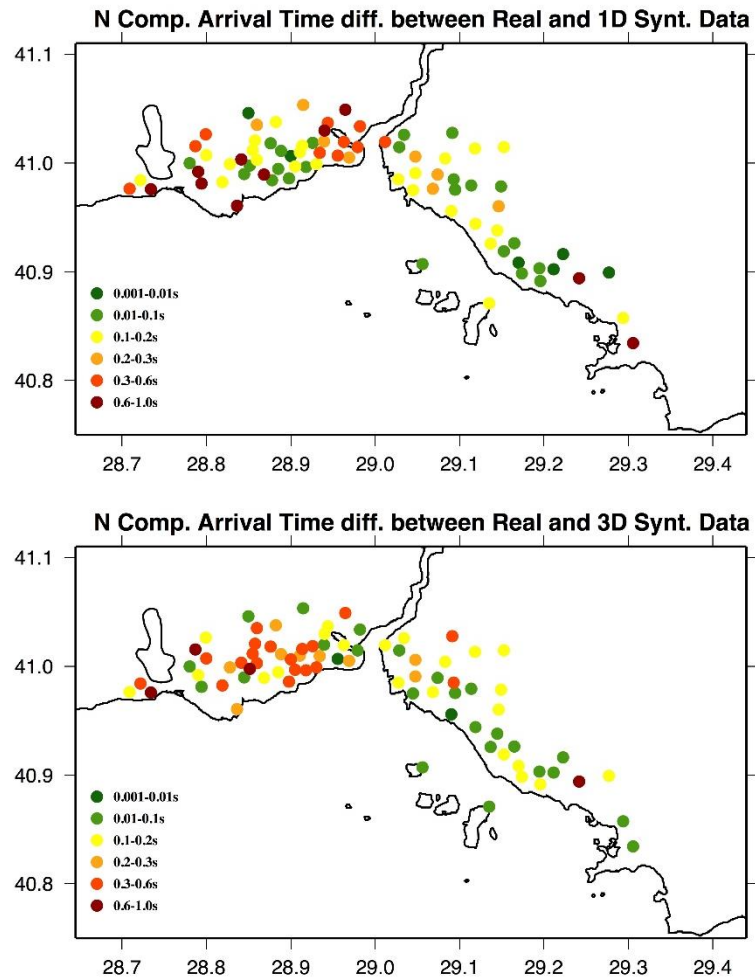
Figure 6.19. S wave time residuals for 1D synthetic to real data and 3D synthetic to real data from NS component velocity waveforms.
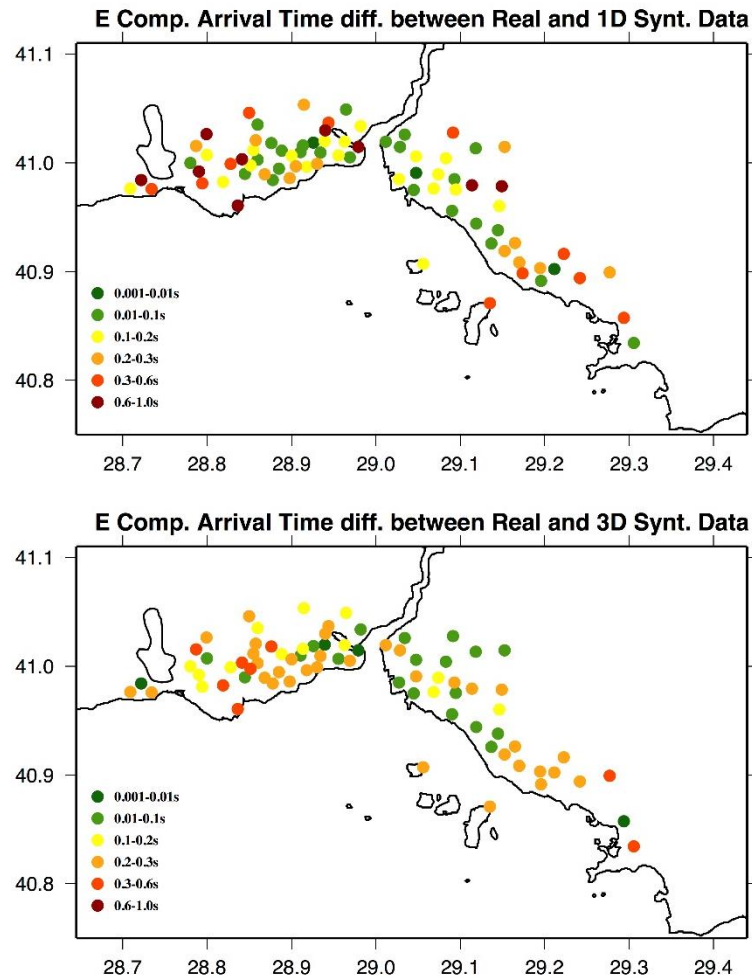
Figure 6.20. S wave time residuals for 1D synthetic to real data and 3D synthetic to real data from EW component velocity waveforms.

The time residuals for 1D are plotted against the residuals for 3D in Figure 6.21, for the vertical, EW and NS respectively. We observe more spreading for the 1D meaning larger errors, in particular for the vertical and EW components for the reasons explained above. To obtain a more quantitative comparison of the time residuals, variances are evaluated for 1D and 3D case. We observe that 3D case always gives a lower error variance with respect to 1D case. A reduction of 20% in error variance is seen in the vertical component and EW component, which is significant considering that we are concerned with timing error of the order of fractions of a second. As before, the reduction in timing error due to 3D is not much significant on the NS component.
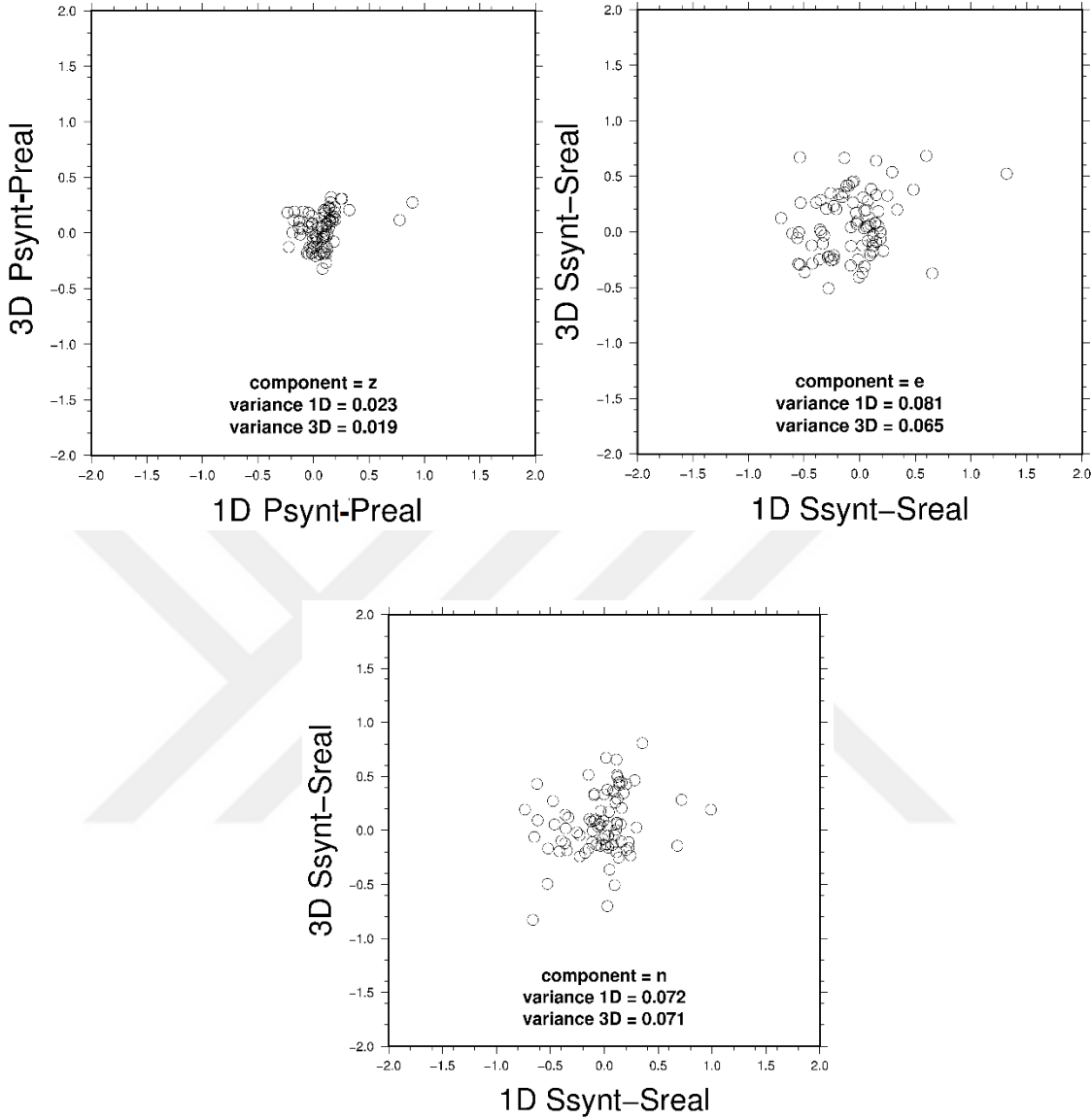
Figure 6.21. Variation of the time residuals (synthetic-real) for 1D and 3D synthetic waveform from vertical and horizontal components.

7. WAVE PROPAGATION AND AMPLIFICATION IN LOCAL BASINS IN ISTANBUL

7.1. Introduction

As mentioned in previous chapters, our study is applied to İstanbul metropolitan area and Çınarcık Basin in a scale covering few tens of kilometers. The study therefore ignores small structures with wavelength less than few hundred meters. However, many settlements are located on narrow dry riverbeds or small alluvial basins and therefore their seismic response are important. The sizes of most of these small-scale features are far below the resolution limit of our study. The other difficulty to include these features in the wave propagation models is the fact that their subsurface geometry is often totally unknown to us. Our purpose therefore is to investigate the seismic behavior of a typical case and expect that this will serve as a model for the others.

This part of the study is focused on one of the largest and the geometrically best known basins of the area, namely the Sabiha Gökçen Basin in Pendik (Figure 7.1). This is a shallow (depth 100-120 m) but relatively large (radius 6 km) basin and its subsurface topography is well documented by recent surveys of Istanbul Municipality. We make use this recent data to simulate the particularities of 3D wave propagation for known local events. Since there is no seismic station close to the Sabiha Gökçen Airport area, we have no chance of comparing synthetic seismograms with real ones. We therefore   investigate the seismic behavior of the basin based only on the synthetic data. A full detailed understanding of wave propagation in relation to the basin geometry is a complex problem and therefore is not the target of this chapter. However we make an attempt to detect the 3D effects of the seismic wave reverberation inside the basin in the context of site amplification. The key question here is to determine how much the simple 1D amplification is modified by the 3D structure of the basin. In conventional approaches, the site response is determined by using only the depth and 1D structure below the site, without taking into account the 3D reverberation. In other words the conventional site amplification at any point is directly a determined by the basin depth at that point. The 1D approach naturally leads to a basin response which one to one

identical to the basin topography. We use this concept for the comparison of 1D and 3D responses. Our approach is to generate synthetic signals in the 3D structure, simulating real earthquakes response, and we check how much the 3D amplification patterns deviates from the basin subsurface topography. We look at the synthetic data both in time and frequency domain, and comment about the amplification patterns that do or do not directly correlate with the geometry of the basin.
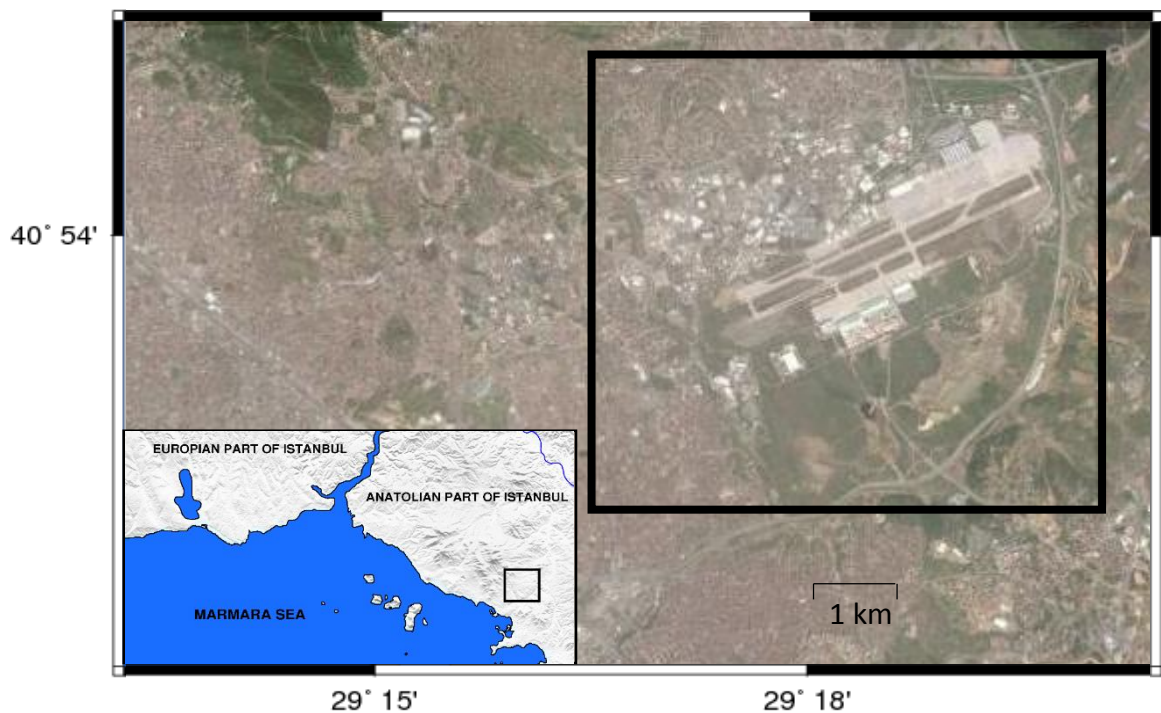
Figure 7.1. Dimension of Study Area.

The location and dimension of the study area are shown in Figure 7.1. We first introduce geological and structural properties. We than explain how the basin is modeled and how the computational model parameters are chosen. Results are given in terms of peak ground velocities and dominant frequencies, both in time and frequency domain. Contour maps are also included to present the spatial variation of the amplification.

7.2. Basin Structure and Computational Model

As indicated earlier, we have chosen the basin covering Sabiha Gökçen Airport area as a case study firstly because of its size and secondly for the availability of the detailed

subsurface geometry. The basin is filled by unconsolidated soft sediments, which show a large seismic contrast with the hosting rocks. The soft sediments are known as Sultanbeyli formation including alluvial funs, mud and debris flows, associated in general with very low shear velocities. The soft sediments are nested in the Istanbul Paleozoic formation, which locally includes mixture of limestone, sandstone and greywacke. Detailed information about Sultanbeyli formation and other young local deposits are given in the last part of Chapter 2.

The simulation of the 3D wave propagation is done using the same tools as the one in the earlier chapters, namely the finite difference code WPP. We have also used the same earthquake source of September 29, 2009 in Çınarcık, for the generation of synthetic seismograms. The basin geometry was obtained from the geophysical and geotechnical surveys carried out by the İstanbul Municipality Microzonation Project. The basin data has sufficient resolution to observe the frequency range that is of interest for the earthquake risk analysis. The critical point here is the correct modeling of the elastic waves that travels across zones with very high velocity contrast. It is well known fact that the finite difference approaches often suffer from instability when velocity contrast is very high. In our case, we have used a special tools offered by WPP which uses additional procedures to prevent divergence. In this special application, the seismic velocity inside the basin has to be assumed homogeneous and the surrounding hard rock has to be defined as a 1D layered structure. Only the geometry of the basin is taken into account and it is given in terms of a separation surface between the soft sediments and the hard rock. The depth values of this boundary surface are expressed over a regular grid, in a way similar to a bathymetric data. The whole information is inserted into a special file format called "i-file". It should also be noted that the grid for the basin geometry is totally independent of the computational grid and it is not even necessary that lattice in geographic coordinates should cover the horizontal extent of the computational domain. For the structure of the hosting hard rock, we have used for the modified version of the 1D model by Karabulut *et al*. (2002), which was described section 5.3.

The inspection of the basin geometry shows that the bottom is relatively flat for the most part, while the boundary is marked by steep slope. The shape is close to a cylinder. The basin fill is composed of erosional deposits down to nearly 120m as shown in Figure 7.2. The characteristics values for the Vp, Vs velocity and the density for the basin deposit are

taken as an average value of the values obtained from earlier geotechnical surveys, which include seismic experiments and borehole logs. Although the component of the sediments, silty-clays and clayed-silts have standard penetration resistance values somewhat higher than N50, their Vs30 velocities measured by PS logging method are around 300m/s revealing their semi-consolidated nature. The lowest P and S wave velocities used for the 3D simulation were 1500m/sec and 300m/sec, respectively.
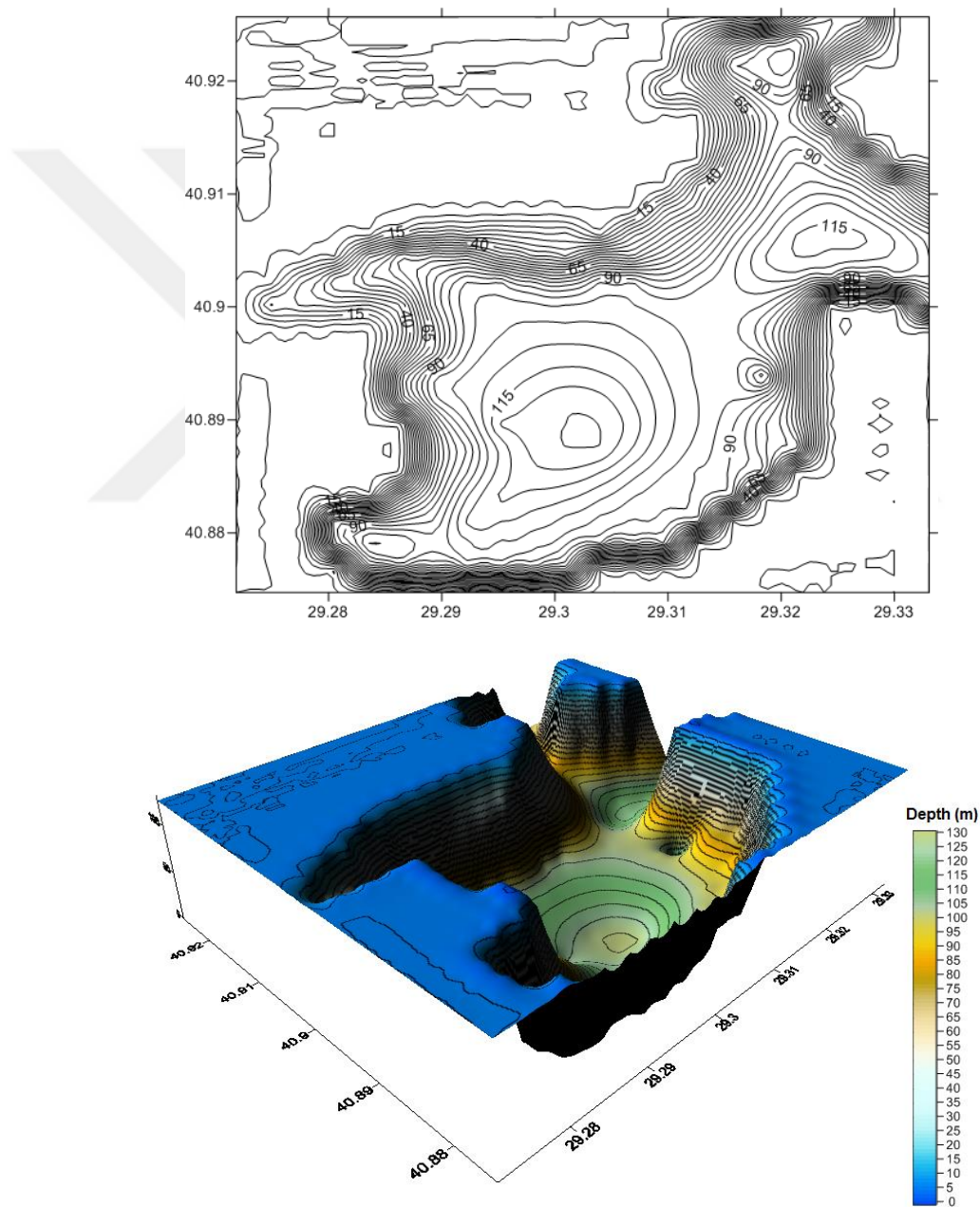
Figure 7.2. Contour maps of Sabiha Gökçen Airport region. Relief map of basin is shown upper and the 3D image of basin is shown in below.

Numerical simulations have been performed using the earthquake of 2004 September 29, Cinarcik, of which the location and the focal mechanism are shown in Figure 7.3. The computational domain covers a volume of 38000 × 31400 × 35000 m^3 which include both the source location and the basin itself. A very fine of grid spacing of 12 m is used for the waveform modeling. This allowed us to propagate S-wave in the basin up to frequencies of 2 Hz, corresponding to 12.5 grid points for the shortest wavelength. Although this is below the limit recommended for WPP, our forward tests showed results were stable. We observed the basin behavior by focusing to an area of size 5.10 x 5.5 km. We look at the waveforms over a grid points with 270m spacing, giving a total of 441 synthetic waveforms with three components (Figure 7.4). The location of the grid is shown in Figure 7.4 enclosed in a highlighted square overlying the aerial picture, which includes the Sabiha Gökçen airport. The surface topography is not included in the finite difference computation and we do not expect that to be critical since the surface relief is quite flat for most part of the area. The simulations were run on a 128-processor on Levrek cluster at TÜBİTAK-ULAKBİM. We simulated 30 second of wave propagation, which required a CPU time of about 12 hour for each run.
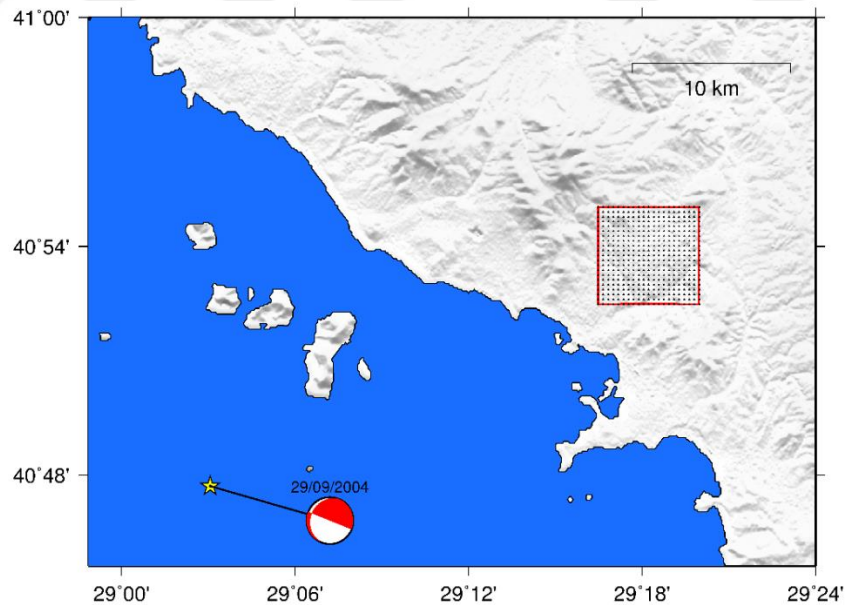
Figure 7.3. The computational domain used for the basin analysis. Earthquake location is shown by yellow star together with the focal mechanism used for the numerical simulation. The area, which includes the basin and where waveforms are analyzed, is defined with red square. Grid of receivers used in the study is shown by black dots. The background grey coloring shows the topography trough shading.

7.3. Results and Discussions

A selection of synthetic waveforms in time domain is shown from Figure 7.5 to 7.7. We show the waveforms on three profiles all in the EW direction. The middle one (G) crosses the deepest part and attains a depth of nearly 120m. The other two are chosen to cut a slice from the edge of the basin, D on the north and M on the south. We expect to see most of the basin related effects along the middle line G, in particular between 22-25 km distances from the source. The location of these three different profiles in the EW direction, are shown in Figure 7.4. In Figure 7.5 to 7.7, the time axis for the waveforms is plotted in the y-direction, while the grid points of the profiles are plotted in x-direction, from west to east. We present all waveforms in terms of vertical, radial and transversal components.

Note that the amplitudes of P-arrivals are too small to be seen in all figures. The large amplitudes arrivals that are observed correspond to the S-wave and the surface waves. This is followed by a coda, which constitutes the main characteristics of the grid points inside the basin. In fact, we observe that the coda for waveforms on the soft ground persist over a long time period, giving an evidence of the complex reflection patterns inside the basin. Conversely the observation points outside of the basin show only the passage of a transient wave front, which quickly attenuate after 3-4 seconds. We also observe that the coda in the transverse components is even shorter than the vertical and the radial components for theses hard rock locations. For the ones inside the basin, we do not observe any difference between the coda of various components. This shows that coda for points inside the basin collects reflections from every direction, and each components quickly loose its distinguishing character such as SV or SH. We also note that the high amplitude arrivals inside the basin are delayed with respect to the hard rock ones. In other words the impulsive S arrivals on hard rock turns into a delayed and tapered train of oscillatory waves on soft soil.
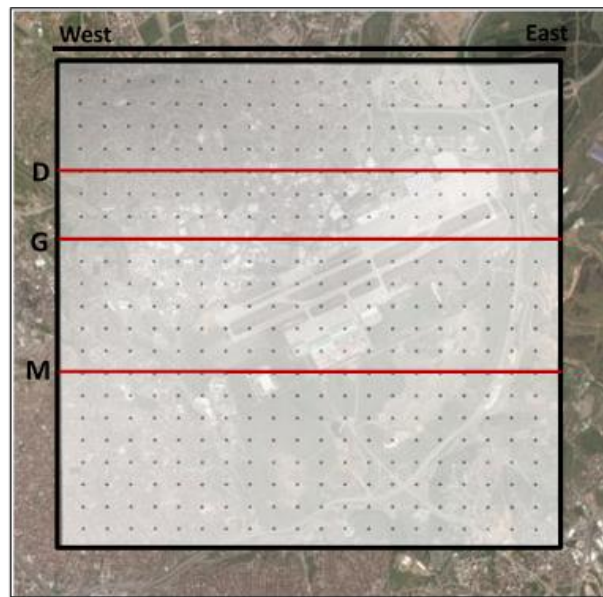
Figure 7.4. Grid area and locations of synthetic waveforms. Grid of receivers are shown by black dots. Red lines correspond to three cross-sections which are D, G and M, respectively.
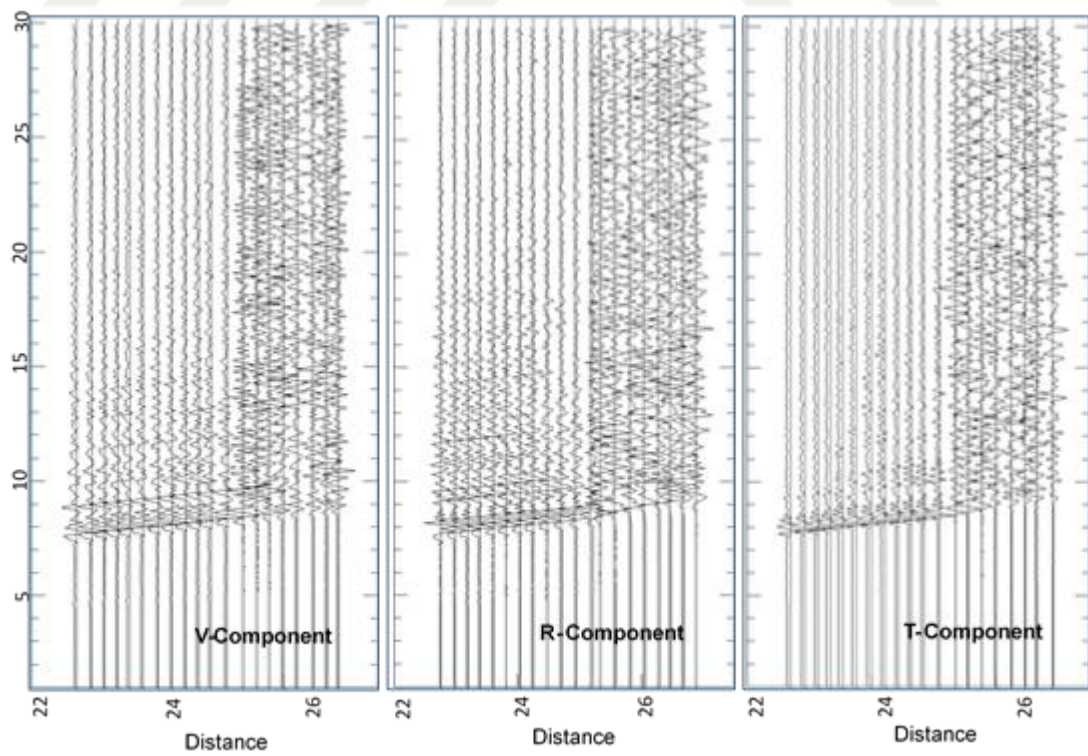
Figure 7.5. Vertical, Radial and Transverse components of the synthetic motions calculated along cross-section D.
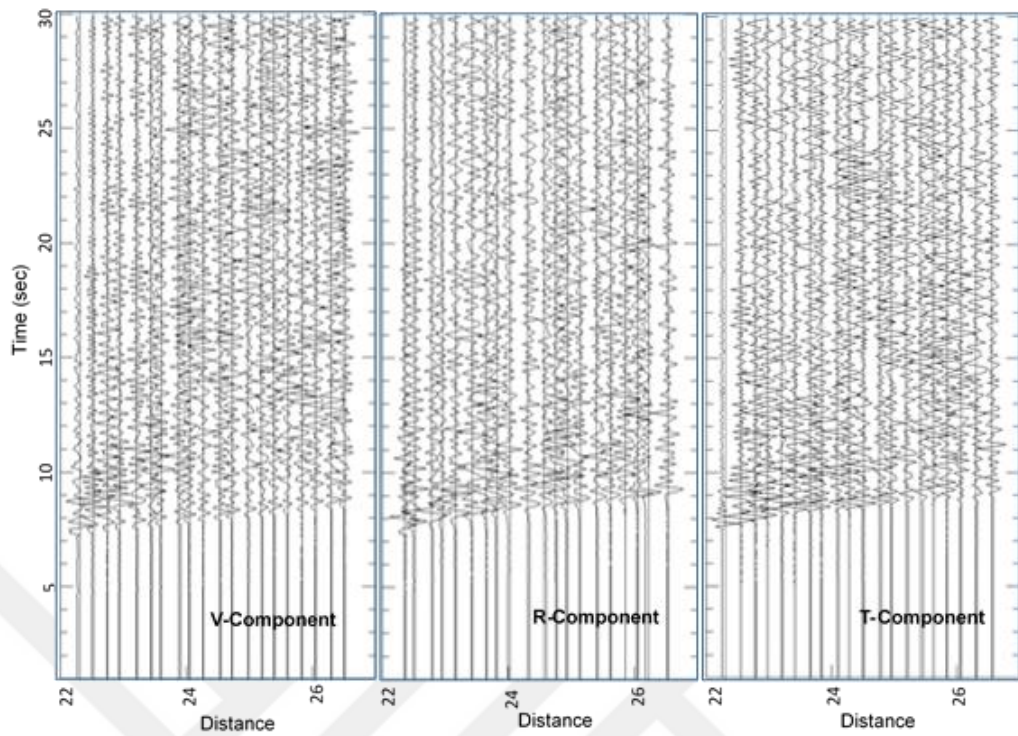
Figure 7.6. Vertical, Radial and Transverse components of the synthetic motions calculated along cross-section G.
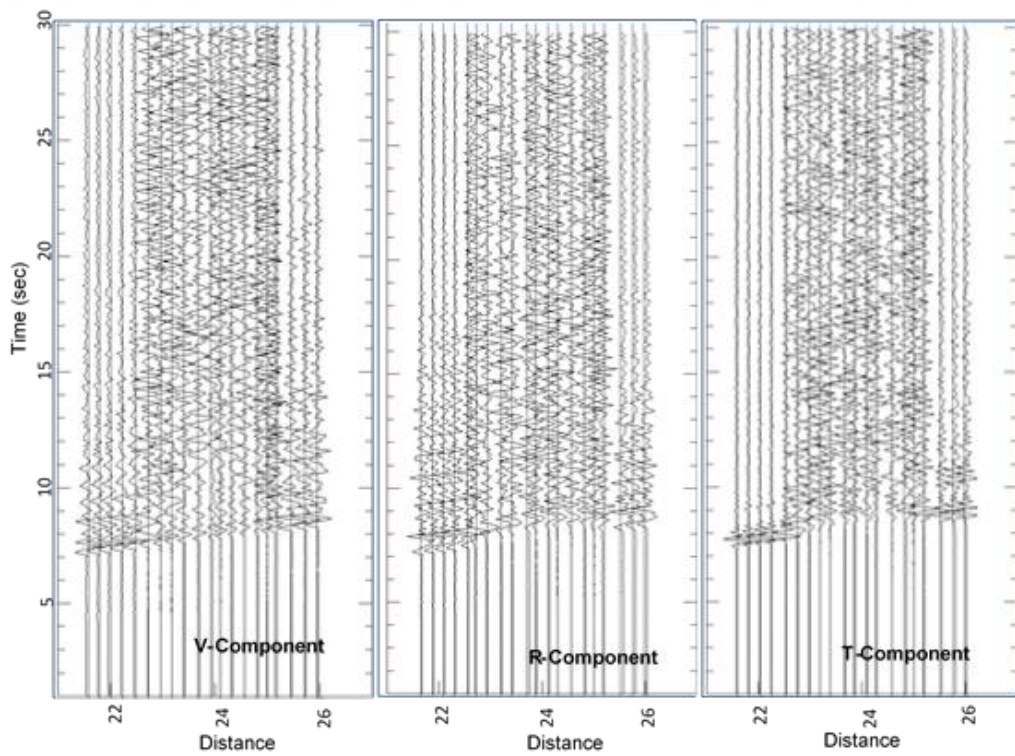
Figure 7.7. Vertical, Radial and Transverse components of the synthetic motions calculated along cross-section M.

We examine the peak ground velocity (PGV), which is accepted to be one of the most favorite measures for the specification of site response. In general PGV is assessed from the unfiltered waveform because the main contribution to the maximum amplitude often comes from the high frequency content. In this work, we have additionally looked at the PGV at various frequency bands. This helped us to determine which are the main frequency bands that are mostly affected by the 3D basin geometry. We have used three frequency ranges given by 0.5-1.0Hz, 1.0-2.0Hz and 2.0-4.0Hz, respectively. These range were selected to correspond to the ones that are often used in hazard studies (Skarlatoudis *et al.,* 2010). We start by comparing the PGV from a hard rock site with the one from the soft soil. We have selected two locations both located on the F profile, one outside (904645271) and the other inside (904645305) the basin. The locations of these points are shown in Figure 7.8.
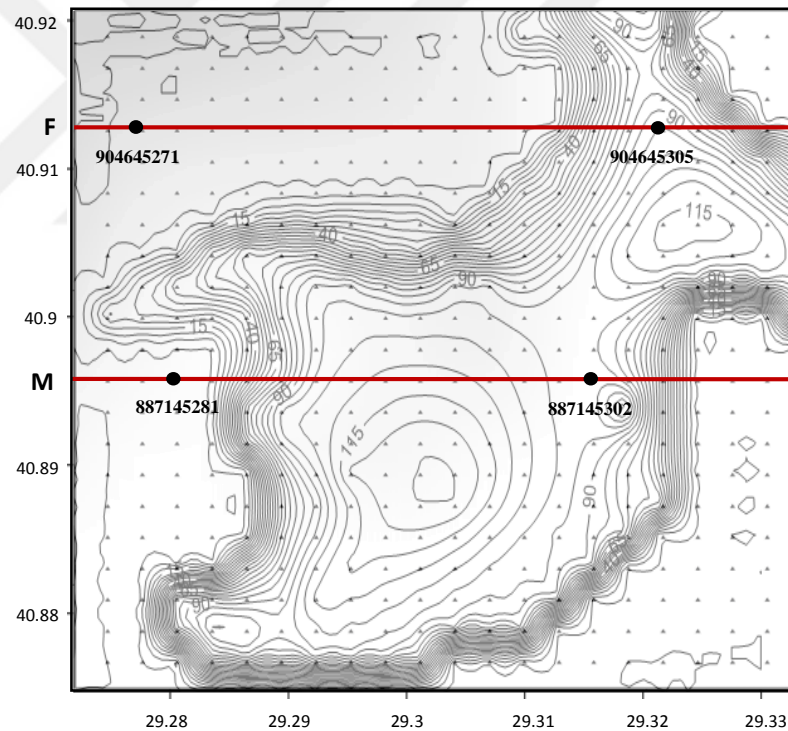
Figure 7.8. Locations of receivers placed outside and inside of the basin structure on cross-section F and M.

The waveforms from the two locations are given in Figure 7.9 with hard rock on the left and the soft soil on the right. The top waveform one shows the unfiltered raw data, while the remaining three show the filtered versions, with the pass-band values given above. Our

first observation is that the largest peak on the hard rock corresponds to the first arrivals, while on soft soil the larger amplitudes arrive later in the coda and are persistent. This shows that continuing and complex reverberation inside the basin may accumulate in time to create much larger amplitudes than the original waveforms. We also observe that, on hard rock the main contribution to PGV comes from the high frequency end as expected. This is however not true for the site located on soft soil where the maximum energy contribution shift towards the mid-frequency range. We conclude that, inside the basin, although reverberations continuously contribute to amplify the waveforms, the attenuation works the other way by gradually tapering off the energy at high frequency. A final remark concerning the basin effect is related to the question of which component contains the maximum PGV. In this case study, we have observed that, on hard rock site, the maximum PGV is on the vertical component, where else inside the basin it is on the transversal. This may be due to the fact that since high contrasting velocity is absent on hard rock we have no Love wave generation. On the other hand, since Rayleigh type surface wave does not require any velocity layering, it is efficiently generated and observed on the vertical component. Conversely inside of the basin, the shallow geometry of low velocity deposit creates an ideal channel for Love wave generation and that is why we can observe high amplitude PGV on the transverse component. There is no doubt that one would need more observations and certainly more elaborate physical investigations on this issue before making a general conclusion.

Figure 7.9. Vertical and transversal component motion from two location on hard rock (left) and soft soil (right).

We have also estimated the PGV for all of the 441 grid points covering the study region, as shown in Figure 7.8. These values are then used to obtain a contour map that illustrates clearly the spatial variation of the PGV, both inside and outside of the basin. The contour maps are plotted for PGV's related to 4 different frequency bands (unfiltered, 0.5-1.0Hz, 1.0-2.0 Hz and 2.0-4.0 Hz) and also for all of the three components (vertical, radial, transversal). Results are displayed in Figure 7.10, for all combinations of frequency and components in the form of a 4x3 matrix. Many properties of the PGV related to 3D basin effects can be seen from the contour maps. We first note that comparing the interior of the basin to the exterior, we see that the PGV is quite stable over the total area covered by hard rock. On the other hand, the area inside by the basin shows very complex PGV variation patterns that are not easily explained by simple wave propagation considerations. We next concentrate on the variation inside the basin and note that the horizontal and the vertical components behave in exactly opposite ways. The vertical component has its maximum at the center of the basin, where else the horizontal components reach their maximum on the boundaries of the basin. For the vertical component, the location of maximum PGV coincides exactly with the deepest part of the basin. In other words the vertical component follows closely the bathymetry of the basin, which is a sign that it is not much affected by 3D reverberations. Conversely, the maximum PGV on the horizontal component does not coincide with the deepest part of the basin, but follows the shallow boundaries. It looks that the 3D effect plays an essential role in amplifying the horizontal components. We may conclude that the conventional 1D site response studies may work for the vertical component, but will totally fail for the horizontal ones.

We have also observed that PGV values show frequency dependent properties. The two lower frequency bands (0.5-1.0Hz and 1.0-2.0 Hz) are quite identical and characterize well the observations explained above. The highest frequency band (2.0-4.0 Hz) however seems to display complex, even chaotic behavior. We could conclude that, up to a certain frequency limit, the general trend of the wave propagation patterns are controlled by the shape of the basin. Finally, we even may claim that there is a threshold frequency, above which the complexity suddenly dominates and no general trend can be defined for the wave behavior. The site amplification at high frequency is possibly connected with the interactions of complicated 3D wave paths within the small-scale irregularities of the basin geometry. In addition to the complexities already mentioned, we should also not ignore the fact that the

wave interactions are additionally controlled by directional characteristics of seismic source, namely the fault plane.
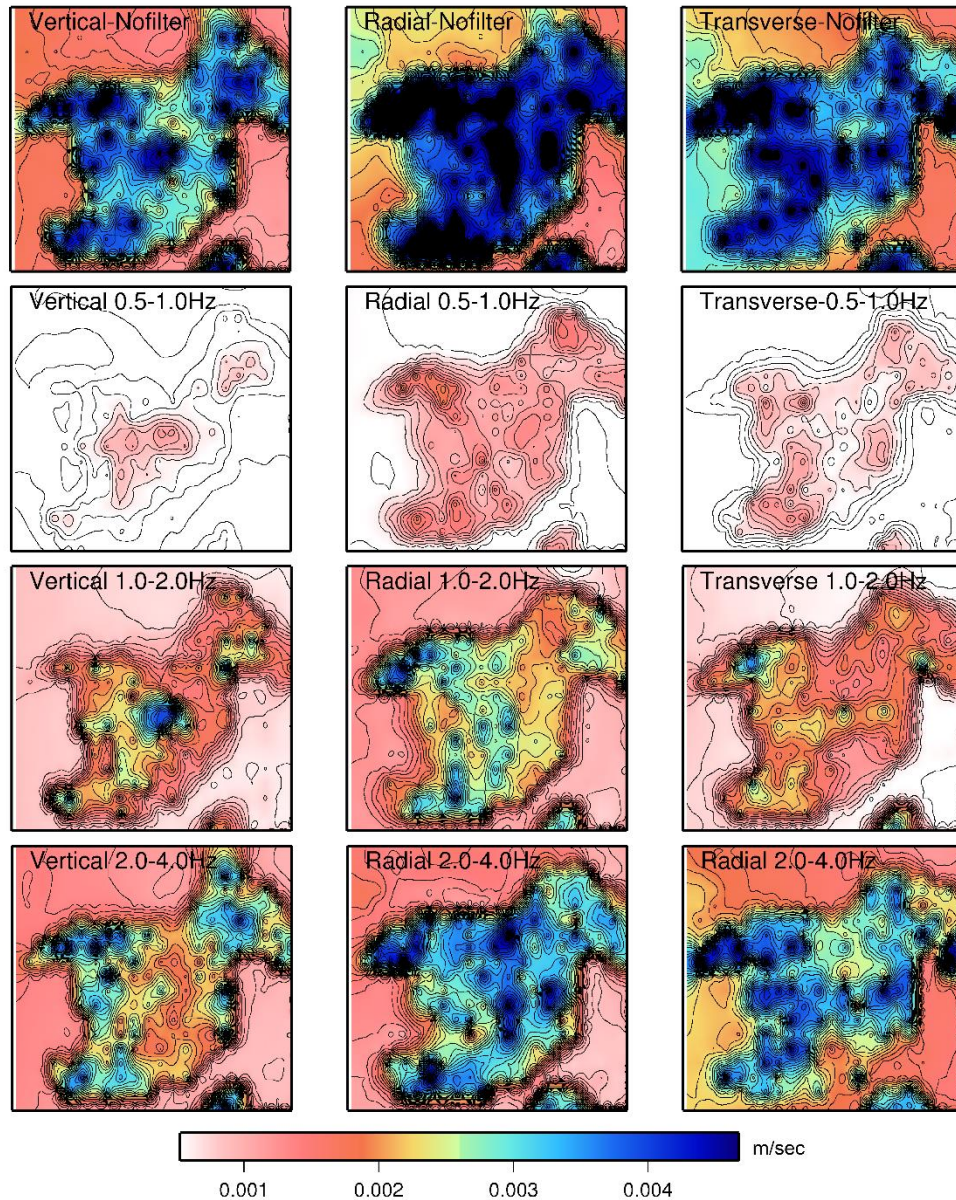
Figure 7.10. Spatial variation of PGV for different frequency bands.

As an additional measure, which can provide another significant evaluation of the site response, is to find the dominant frequency of the seismic reverberation. This is done by computing Fourier amplitude spectra and picking the frequency of the highest peak. We have applied this procedure for three different windows of the seismograms: first the full

waveform, second the S-wave segment and finally the coda train. The purpose of selecting different windows is to try to figure out if the oscillations of the coda train may have any link to the S-waves, to the more complex arrivals such as surface waves, or to any of them. Each window is individually extracted from the seismograms, tapered and Fourier amplitude spectrum is computed.

We have computed the spectral characteristics at two grid points, one outside the basin on hard rock (887145281) and the other inside the basin on the soft soil (887145302). Both points are located on the same EW profile M and their position relative to the basin geometry is shown in Figure 7.8. Figure 7.11 shows both the time waveforms and their associated Fourier spectra. The left column corresponds to the hard rock site and the right column to the one inside the basin. For each site the vertical component is given on top and the transversal on the bottom. The figure is arranged in the form of a 2x2 matrix, two sites as the columns and two components as the rows. Each element of the matrix comprises four plots, the one on the top is the time wave and the ones below are the 3 spectra. The 3 spectra correspond to the Fourier Transform of the full waveform, the S-wave window and the coda window respectively. Both the S-window and coda-window are shown by blue line on the time curve. We have used only the ending part of the coda in order to include only the most persistent components of the oscillations in the seismograms. Comparing the maximum value in the y-scale of the spectra on the left and right column, we first observe that spectral amplitudes are one order of magnitude smaller for the hard rock site. In hard rock site, both the vertical and the transversal components of the S-wave window do not seem do contain any surface wave arrival. For the case of the basin site however, there is a clear sign of surface wave generation. For the vertical component of the soft soil, possibly Rayleigh arrivals are partly included inside the S-wave time window. For the transversal component, the arrival of Love wave is clearly outside the S-wave window. For the hard rock site, the S-wave spectra strongly resemble the total waveform spectra, in both vertical and the transversal components. This means that it is the S-wave, which contributes to most part of the total spectra in both components. Again for the hard rock site, the spectral shape of the coda is significantly different from both the total wave spectra and the S-wave spectra. This means that the oscillatory character of the coda has either died out very quickly on the hard rock site, or else it is totally non-existent. The spectra on the soft ground are more difficult to interpret. All components from time windows seem to have large similarities. The contour

plot of the spatial variation of the dominant frequency provides more useful interpretation for this issue. For that purpose we pick the dominant frequency of oscillation from the seismogram corresponding to each individual grid point.
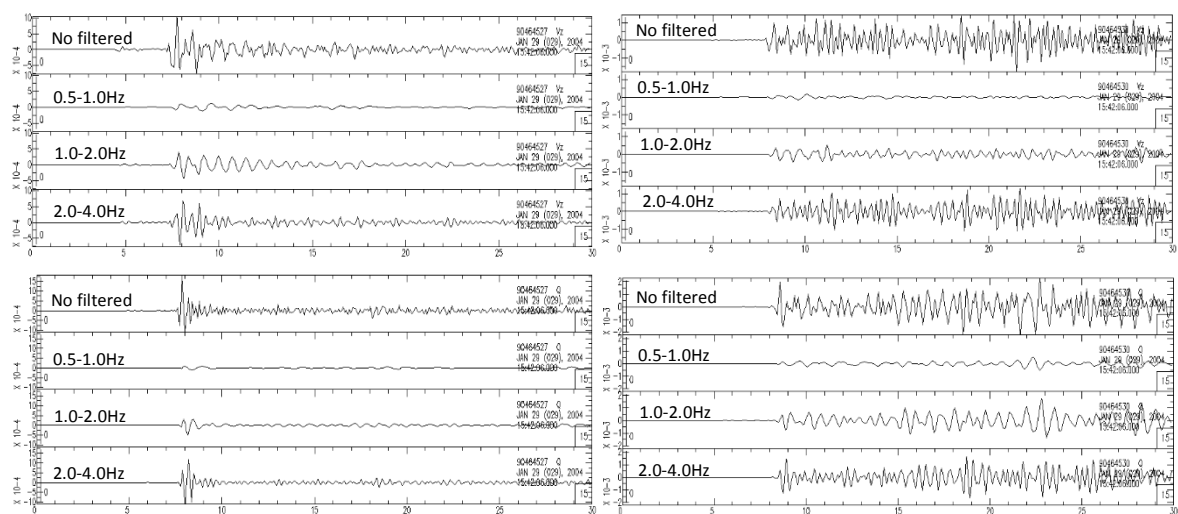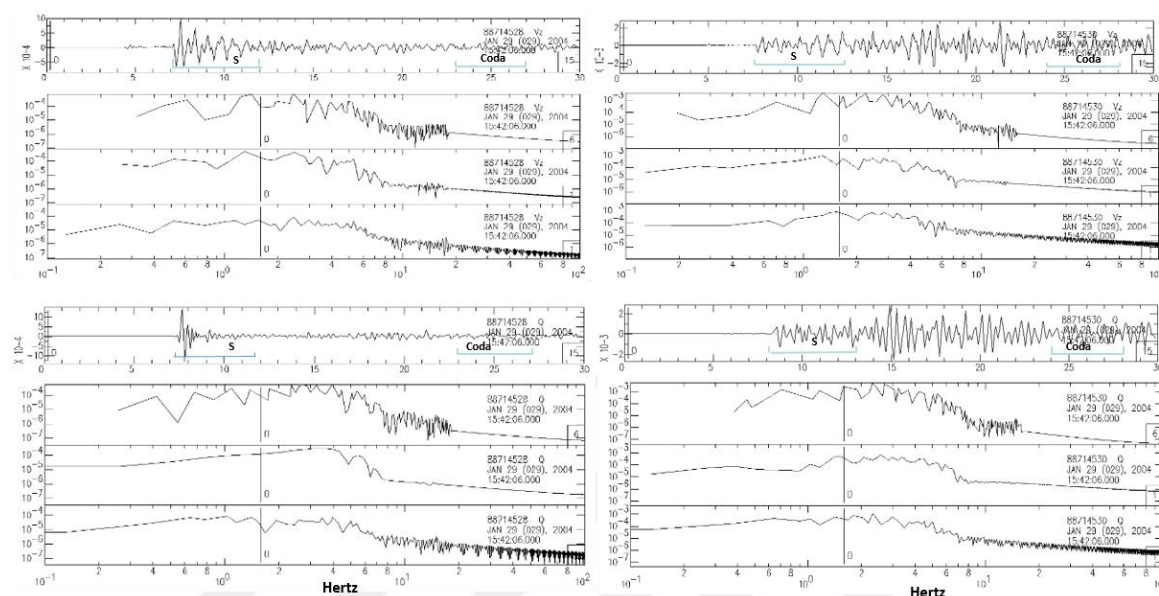

Figure 7.11. Vertical and transversal component from two location on hard rock (left) and soft soil (right) and their Fourier amplitude spectra of full waveform, S-wave and coda wave window.

The frequency values for all grid points are interpolated to give a contour plot of spatial variation. The analysis is applied for all three windows (total, S-wave, coda) and all three components. Figure 7.12 illustrates the spatial variation of the dominant frequency in 2x3 matrix form. The two rows correspond to the time window selection, namely the total waveform and the S-wave window. The three columns correspond to the component selection, namely vertical, radial and transversal. Interestingly we observe that the shape of the basin is clearly visible on the patterns of the transversal components, both on the total waveform and on the S-window. The interpretation would be that since the transverse component mostly includes trapped Love waves, this type of surface waves responsible for most part of the oscillations. There is also a sign that the SH component in the S-window is the component which provide the initial energy of the Love waves. This same argument is also supported with the Figure 7.13. In this figure the spatial distribution of the dominant frequency is shown for the transversal component for three different time windows

corresponding to S-wave, surface-wave and coda. We observe that the first two, namely the S-wave and the surface-wave, have strikingly similar distribution, which is strongly correlated with the basin geometry. The coda part, on the other hand, shows totally different patterns weakly correlated with the basin. This again shows that the SH arrivals and Love waves are the main source of the reverberations which continue to shake the basin for a time. Towards the fading part of the coda, the oscillations are still there, but their character has become too complex to be associated with any type of surface wave. Likewise, the end part of the coda is too complex to continue to reflect the geometry of the basin.
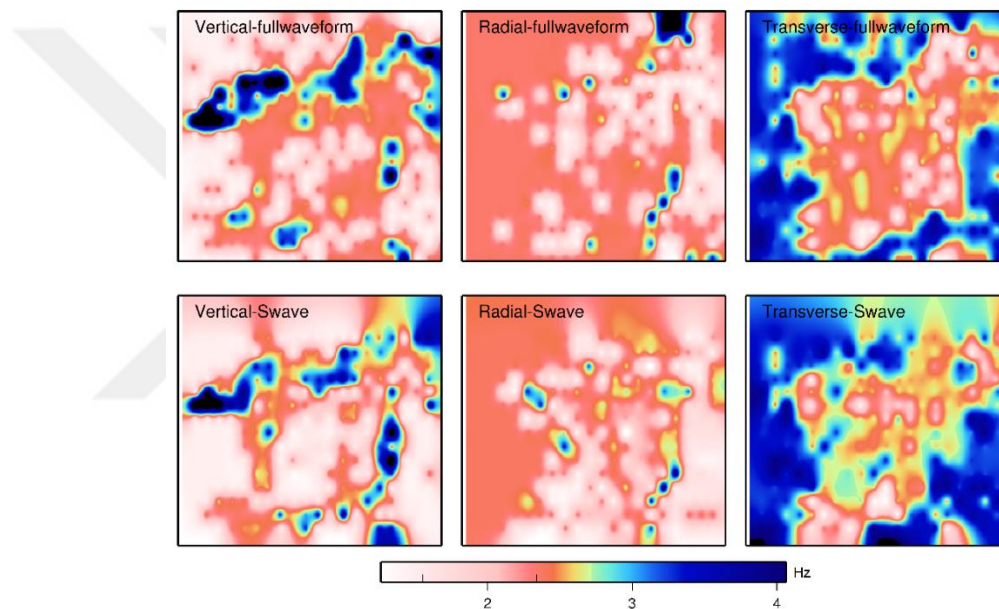
Figure 7.12. Spatial Distribution of Dominant Frequency. Top row is for the full waveform, bottom row for the S-wave window.
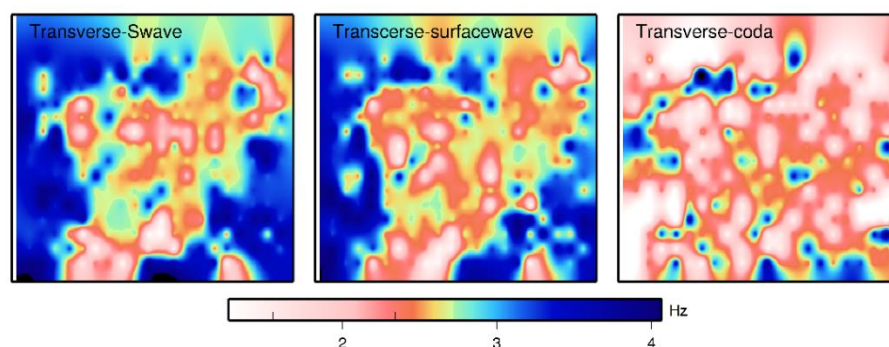
Figure 7.13. Spatial Distribution of Dominant Frequency for transverse component motion for S wave, Surface wave and coda window.

8. CONCLUSIONS

The main focus of this thesis is the implementation of the 3D seismic wave propagation in the east of the Marmara Sea, in particular around the city of Istanbul. The work includes three distinct stages: first a 3-D velocity model is constructed based on existing field data, second a finite-difference approach is implemented on parallel computers for the waveform propagation, and finally the model is tested using real earthquake data.

In terms of achievement, the thesis has produced the first 3D model for the metropolitan area of Istanbul, which is essential for hazard studies. A suitable parallel finite difference code is installed and tested on two national supercomputing centers. The code is adjusted for most efficient use of core configuration and the outcomes are calibrated using well-known 1D approaches. The 3D model is tested with real earthquake data and improvement due to 3D modeling is verified in a clear and quantitative way. The event used for the testing is analyzed using an unprecedently high number of stations and applying new improved techniques. The event analysis constitutes a typical case study, which can serve as a template for future events to occur in the area. Finally, 3D wave propagation is implemented for the local basins located inside the study area. The results are analyzed in order to detect the limits where the conventional 1D site response analysis techniques over the 3D techniques.

Before investigating the main outcomes of the thesis a short discussion will be useful for explaining the choice of the scale for the study area. In general 3D models are developed for areas of few hundred kilometer or more and therefore concerns frequency range below 0.5 Hz or lower. This is mainly due to the fact that going to higher frequencies requires a more detailed knowledge of the velocity structure which is often not available. At the beginning of the study, the study area was also intended to cover the whole of the Marmara region. However, throughout the course of the study the region is reduced to include only the east of the Marmara Sea, including the Princes' islands and the northern boundary of the Çınarcık basin, in particular the Anatolian and the European part of city of İstanbul. This reduction in size for the study area is mainly due to the need of going to higher frequency in particular into the range, which is of more interest for seismic hazard problems. When the

effects of earthquakes on buildings are considered, damage is expected at higher frequencies (0.5-2Hz) considering the general characteristics of the building stocks in İstanbul.

A fortunate coincidence was that during the course of the thesis, The Municipality of Istanbul carried out an intense survey of shallow structures, which provided the main source of information for the development of the 3D structure in this thesis. Since this detailed information was mainly available for the metropolitan area only and since the computational burden increases exponentially with the size, it was logical to limit the study area to the populated areas and surroundings. Note that the few existing 3D models published in the literature do not cover the shallower depth up to 1km, especially for İstanbul and surrounding. They cannot resolve the details at high frequencies and therefore do not fully compensate the need of hazard assessment.

The second important step of this study is the testing of the 3D model with real data. This depends on the availability of earthquakes occurring within the simulation boundaries as well as seismic data recorded at stations inside the study area. There is a limited number of small to moderate size of earthquakes occurred in the Sea of Marmara. They however are mostly outside the simulation boundaries and were not recorded fully by the existing stations. The only one that fulfills those needs is the event with magnitude of 4.1 occurred in 2004 close to the Princes Islands, and therefore constitutes our main reference event. This reference event also has a limited energy at low frequencies (<0.5 Hz), which is another important point that we performed modeling at high frequencies. This event was fully recorded by the RR stations placed both on the Anatolian and European side of İstanbul making it possible to test the model within the frequency range of interest, over a wide area of coverage.

The development of an integrated 3D seismic/geologic model is one of the main targets of the study. At initial stage, previous crustal studies in Marmara region created a resource for deeper structure while the available field data including surface and borehole measurements in the city of İstanbul created a resource for shallower structure. The construction of the 3-D model was based on filling the gaps between the set of reference points obtained from 1D velocity models. We have used Delaunay triangulation methodology for the interpolation of both the deep and the shallow structure independently.

Models at both scales were combined into a single one and expressed in a special format suitable for 3D structures (p-file). Considering the deep scale, we observed that velocity is relatively low below the Çınarcık basin, which reaches a depth of about 6 km. The Moho depth varies in the EW direction from 25 km under the European part to the 28-30km beneath the Anatolian part. This result is consistent with Becel *et al.* (2009), which defines that Moho depth is shallower offshore beneath the Çınarcik Basin pointing to a thinner crust in the Marmara. When considering the details of shallow structure, European part includes much more low velocity features at shallow depth than the Anatolian counterpart, which is more rigid at the shallow depth. A sudden increase in velocities towards to north is observed due to the presence of more compact materials North of Atakoy. At the easternmost European part, a local velocity decrease is observed which reflect the soft sedimentary fill near Yenikapı.

The success of 3D model testing critically depends on choosing proper numerical tools for the seismic wave propagation. In this thesis we have used a new 3-D finite difference tool (WPP) which defines second order accurate discretization of elastic wave equation based on energy stability for the overall discretization even at grid refinement interface (Nilsson *et al.,* 2007). Because that code is operated by parallel processing environment and requires high performance computational cores, it was built on two national high performance laboratories namely the large Linux clusters at ITU-UYBHM and the TUBITAK-ULAKBIM systems. To verify the 3D finite difference code, a comparison is made with the discrete wave number method (DWNM) by Bouchon (1981) using the same velocity model and the same source parameters. The comparison of the two different method shows that the amplitude and the waveform shapes are very much similar in each method. Following this verification, many experiments were performed on interrelated parameters of both user-selected parameters (such as frequency of interest, seismic velocities, the size of the domain, etc.) and automatically determined parameters (such as the number of grid points per wavelength, number of grid points, number of sampling points, computational time, etc.). The WPP code allows the use of variable grid spacing in order to make computation more efficient. Our experiments have shown that using composite grid instead of uniform grid would result in considerable gain in computational time without losing any accuracy. We have therefore adapted a variable grid pattern, starting with 25 m at the surface and reaching 100m at deeper parts. This achieved a final computational reduction of the order 30%.

An accurate comparison of the observed and synthetic waveforms depends critically on a reliable estimation of both the earthquake location and the source parameters such as origin time, magnitude and especially focal mechanism parameters. In our testing with real data, we have chosen selected the largest event (September 29, 2004, Ml=4.1) that occurred within the boundaries of the 3D model. This event occurred in Çınarcık Basin and triggered the RR Network and made strong data available from a large number of stations in addition to the permanent weak motion stations. Both the location and focal mechanism were analyzed in detail using three components waveforms from18 broadband and 100 strong motion stations.

Hypocenter location procedure, which was adapted for the particular geometry of the strong motion network, used a total of 115 P and 81 S phase reading. Only stations with distance less than 100km were used and this provided a dense set of arrival times in a relatively narrow angle of azimuth coverage. We have performed a detailed analysis of the arrival time residuals and compared the suitability of existing 1-D velocity models (Bulut *et. al.* 2007 and Karabulut *et al.*, 2002). We found that reducing the Vp/Vs ratio from 1.78 to 1.72 in the velocity model of Karabulut *et al.* (2002) gave a more consistent S arrival times. After several tests, we finally have chosen the depth to be 9.6 km, which puts the hypocenter exactly on the fault plane inferred by Armijo *et al.* (2002).

The fault plane solution of the reference event was determined using multi stage estimation process starting with the classical P-wave first motion approach and evolving to P and S-wave amplitude fitting. The conventional P-wave first motion analysis based on 103 P polarity readings gives right lateral strike slip motion with a significant component of reverse faulting (strike 105°, dip 74.19°, and rake 98.31° for Fault Plane1 and strike 256.44°, dip 17.84°, rake 62.98° for Fault Plane2). We did not remain limited with conventional method to achieve our target of finding accurate source parameters. Next an amplitude based approach was applied to find the optimal fault plane parameters, which best fit the P and SH waves not only in terms of polarity but also using amplitude. Real and theoretical P wave amplitudes shows negative (downward) polarity although the polarities of both real and theoretical SH wave amplitudes were flipped at a certain azimuthal range corresponding to either the fault plane or the auxiliary plane. We applied an exhaustive search approach, which gave a right lateral strike slip motion (strike 112°, dip 90°, and rake 108° for Fault

Plane1 and strike 200º, dip 18º, rake 0º for Fault Plane2) in agreement with the NAF. That strike direction (strike 112ºN) is also in agreement with the strike of the NAF, which locally follows the northern boundary of the Çınarcık basin. It is clearly seen that consistency of P and SH waves for this new improved solution is markedly different from the FPS obtained by conventional approach. Clearly, the additional reverse component and the misfit of the SH amplitude in the earlier result using the conventional method were spurious. Note that if we compare the amplitude distribution for the solution obtained by BDTIM solution with the solution of our study, the former one gives a total misfit in terms of both P and SH wave amplitudes.

Once a reliable estimate of the seismic source is obtained we have proceeded with the synthetic waveform generation using the 1D and 3D models. The synthetic waveforms were compared with real data in terms of their delay times, waveform shapes and amplitudes for the available stations. The comparison provided a quantitative way to evaluate how much improvement was achieved by using 3D modeling. It also served to identify parts of the model were improvements could be made in the future. 1D and 3D synthetics are very different in terms of their waveform shapes and amplitudes although the polarities of first arrivals show relatively good agreement. Compared to real data, 1D synthetics shows a high P and S (especially from EW component) wave amplitudes throughout the Anatolian side, particularly onshore areas from Bostancı to Kartal. In contrast, 3D synthetics show a very good agreement with real data. Considering the European part, once again 3D synthetics gives better amplitude fits with real data than 1D synthetics. Nevertheless the 3D synthetics have slightly lower P and higher S wave amplitudes relative to real data except for Fatih and around Golden Horn area. Waveform comparisons for stations located around Golden Horn area which is mostly covered with Thrace formation, show a different characteristics from other stations in the European part. Mostly located on hard rock sites, no shallow oscillations are observed in these waveforms and as in the case of most stations on the Anatolian part. This may arise from hard materials consisting of sandstone (greywacke), siltstone or claystone, which outcrops around the Golden Horn erosional valley. This is in agreement with Birgören *et.al.* (2008) who also found that hard rock sites are common in the Anatolian part and along the shorelines of Golden Horn. As contrast to Golden Horn, the stations in the western side of European zone, extending from Yedikule to Avcılar, provide oscillatory signals which refer deeper sedimentary cover. This corresponds mostly to the low S-wave

velocity due to soft and young sediment cover. In the case of these waveforms with high oscillatory character, a direct comparison in time domain was not very useful. Instead we have used spectral comparison (FAS-Fourier Amplitude Spectrum) of waveforms, which was more suitable for revealing the oscillatory behavior. A general inspection of spectral shapes shows that 1D synthetics seldom show any spectral peak and spectral amplitudes are lower than the real data, at nearly all frequency range. On the other hand the Fourier Spectrum of 3D synthetics shows higher amplitudes values consistent with the real data. The spectral peaks in the 3D synthetics, which shows the oscillation characteristics of the sedimentary cover, generally coincides well with the peaks in real data.

The comparison of the time residuals between observed and synthetics waveforms is carried out both by eye inspection and also more accurately by cross-correlation. Both approaches were useful since the former one detects the rising onset and the latter one takes into account the whole shape for the source pulse. Comparison of the rise time for the observed and the 1D synthetics shows that P and S time residuals may reach up to 1.0 sec. For 3D synthetics, it is clearly observed that are under 0.3 sec and 0.6 sec for P and S respectively. 3D synthetics have lower time residuals than 1D for P and S time at Golden Horn and Fatih in European part and some areas covering Üsküdar and Kadıköy. For 3D synthetics, early arrivals were observed throughout the Anatolian part and some stations in European part specifically in Avcılar. This should come from slightly higher velocities of the deeper layers in 3D model. In contrast, 3D synthetics predict late arrivals for stations located in southern European part which points to the need of fine adjustments.

The comparison of 1D and 3D synthetics with real data is also carried out automatically using the first arriving pulse. The waveforms are bandpass filtered to reveal only the first arrival pulse, which should corresponds to the source time function. We have used the vertical component for the P-wave arrivals and only EW components for the S-wave arrival. The EW component in our case corresponds mostly to the SH arrival due to the geometry of the network with respect to the event location. On the other hand, the NS component corresponds to the SV component, which is often contaminated by P-wave coda, and thus we avoided using NS component in our analysis. In fact, the observation on the NS component did not provided any significant improvement for both amplitude and time errors comparison.

First we compared the amplitude of the first arriving pulses of real and synthetics data, for both P (vertical) and S waves (EW). The difference in amplitude is defined, as the quantitative measure of the modeling error and the variance of this error is an indicator for the success of the modeling. We have observed that 3D synthetics have lower variance values than 1D case, both the P and S-waves. More specifically, 3D modeling reduced the variance of the amplitude error from 0.125 to 0.053 and from 0.073 to 0.039, respectively for P and S waves. Similarly, the arrival time was also compared by cross correlation. We have also found that an improvement with 3D is achieved by reducing the time residual variance from 0.023 to 0.019, and from 0.081 to 0.065, respectively for P and S wave.

At the last part of our study, we investigated in detail the seismic behavior of the shallow basins located inside the metropolitan area. There are a number of such basins both in the west and in the east of the metropolitan area, which vary in size and shapes. The sedimentary cover is often shallow of the order of 100 m but extending to few km in horizontal. The largest of these basins is the one where Sabiha Gökçen Airport is located. The purpose of the study is to test if the 3D structure plays critical role site amplification. The key question here is to see how much the amplification is modified by the 3D structure of the basin. In conventional analysis, the site response is determined using only the depth and 1D structure below the site, without taking into account the 3D reverberation inside the basin. This 1D approach naturally leads to a basin response which one to one identical to the basin topography. In this context, our approach is to generate synthetic signals in 3D structure simulating real earthquakes response, and we check how much the 3D amplification patterns in 3D deviates correlates with the basin topography. For that purpose, we look at the synthetic data both in time domain and frequency domain. In time domain, we clearly see that deep part of the basin amplify the wave amplitude and reflections within the basin continue for a long time without damping. This is in agreement with geologic and geotechnical properties of the basin. In frequency domain analysis, we observe that peak velocities show different characteristics for three different frequency ranges (0.5-1.0Hz, 1.0-2.0Hz and 2.0-4.0Hz). The variability of site amplification at different frequency ranges is the indicative of the impact of complicated 3D wave propagation. We generally conclude that the fundamental mode of oscillation for the sedimentary fill remains undisturbed by the 3D structure. The 3D effect is more important for the high frequency oscillations and in particular at corner parts of the basin. This effect is more perceptible on the vertical

component, although it is observed in all other components. This situation which is observed is spectral domain is also consistent with the patterns of maximum peak velocities.

We expect that the presented work is a first attempt to develop a 3D structure for the city of Istanbul and surroundings. It is clear that it will serve as a basis for further modeling studies. The model that we have developed uses the data from the most recent geophysical surveys. We did not made any attempts to include any geological information, which is mostly available in a more qualitative fashion rather than numerical. In future, quantizing and including the geologic data, as well including as new geophysical data as they become available, can improve this 3D velocity model. The model would be further tested and fine-tuned as more local events will occur and more comparison data would be possible.

REFERENCES

Aksu, A.E., T. Calon, R. N. Hiscott and D. Yasar, 2000, "Anatomy of the North Anatolian Fault Zone in the Marmara Sea, Western Turkey: Extensional Basins Above a Continental Transform", *GSA Today*, Vol. 10, No. 6, pp. 3-7.

Al-Lazki, A., D. Seber, E. Sandvol, N. Turkelli, R. Mohamad and M. Barazangi, 2004, "Tomographic Pn velocity and anisotropy structure beneath the Anatolian plateau (eastern Turkey) and the surrounding regions", *Geophysical Research Letters,* Vol.30(24).

Alterman, Z. and F.C. Karal, 1968, "Propagation of elastic waves in layered media by finite-difference methods", *Bull. Seism. Soc. Am.*, Vol. 58, pp. 367-398.

Altınlı, İ. E., 1951, "Kayışdağı Bölgesinin Jeolojisi", *İ.Ü. Fen Fak. Mecmuası.,* SeriB. XIV, pp. 2 (*in türkish*).

Ambraseys, N., 1975, "Studies in historical seismicity and tectonics", *Geodynamics Today*, *The Royal Soc.,* pp. 7-16.

Ambraseys, N. and J. A. Jackson, 2000, "Seismicity of the Sea of Marmara (Turkey) since 1500", *Geophysical Journal International*, Vol. 141, pp. 1-6.

Armijo, R., B. Meyer, S. Navarro, G. King and A. Barka, 2000, "Asymmetric slip partitioning in the Sea of Marmara pull-apart: a clue to propagation processes of the North Anatolian Fault?", *Terra Nova*, Vol. 14, pp. 80-86.

Armijo, R., N. Pondard, B. Meyer, G. Ucarkus, B. Mercier de Lepinay, J. Malavieille, S. Dominguez, M. A. Gustcher, S. Schmidt, C. Bech, N. Cagatay, Z. Cakir, C. Imren, K. Eris, B. Natalin, S. Özalaybay, L. Tolun, I. Lefevre, L. Seeber, L. Garperini, C. Rangin, O. Emre and K. Sarikavak, 2005, "Submarine fault scarps in the Sea of Marmara pull-apart (North

Anatolian Fault): Implications for seismic hazard in Istanbul", *Geochemestry, Geophysics, Geosystems*, Vol.6, doi:10.1029/2004GC000896.

Arpat, E. and F. Şaroğlu, 1972, "The East Anatolian Fault system; thoughts on its development", *Bulletin Mineral Res. Exp. Inst. Turkey*, Vol. 78, pp. 33-39.

Arpat, E. and K. Şentürk, 2000, "Development of the Marmara Sea" *(in turkish with an abstract in english) Marmara Denizi 2000 Sempozyumu*, Türkiye Deniz Araştırmaları Vakfı, No. 5, pp. 231-237.

Arpat, E. and K. Şentürk, 2003, "Geological evolution of the İstanbul region since the Middle Eocene" *(in turkish with an abstract in English) İstanbul'un Jeolojisi Sempozyumu*, pp. 39-48.

Atakan, K. and M. B. Sørensen, 2006, *Potential of Vulnerability and Seismic Risk, Large earthquake faulting and implications for the seismic hazard assessment in Europe*, RELIEF Project Deliverable No.27, Dept. of Earth Science, University of Bergen, Norway, 35p.

Barış, Ş., J. Nakajima, A. Hasegawa, Y. Honkura, A. Ito and B. Üçer, 2005, "Three-dimensional structure of Vp, Vs and Vp/Vs in the upper crust of the Marmara region, NW Turkey", *Earth Planets Space*, Vol. 57, pp. 1019-1038.

Barka, A.A. and K. Kadinsky-Cade, 1988, "Strike-slip fault geometry in Turkey and its influence on earthquake activity", *Tectonics*, Vol. 7, No. 3, pp. 663-684.

Barka, A., 1992, "The North Anatolian Fault Zone", *Ann. Tactonicae*, Vol. 6, pp. 164-195.

Barka, A., H. S. Akyüz, E. Altunel, G. Sunal, Z. Cakir, A. Dikbas, B. Yerli, R. Armijo, B. Meyer, B., J. B. de Chabalier, T. Rockwell, J. R. Dolan, R. Hartleb, T. Dawson, S. Christofferson, A. Tucker, T. Fumal, R. Langridge, H. Stenner, W. Lettis, J. Bachhuber and W. Page, 2002, "The Surface Rupture and Slip Distribution of the 17 August 1999 Izmit Earthquake (M 7.4), North Anatolian Fault", *Bulletin of the Seismological Society of America*, Vol. 92, No. 1, pp. 43-60.

Bao, H., J. Bielak, O. Ghattas, L. F. Kallivokas, D. R. O'Hallaron, J. R. Shewchuk, and J. Xu, 1998, "Large-scale simulation of elastic wave propagation in heterogeneous media on parallel computers", *Computat. Meth. Appl. Mech. Eng*. 152, 85–102.

Bayliss, A., K. E. Jordan, B. J. LeMesurier and E. Turkel, 1986, "A fourth-order accurate finite-difference scheme for the computation of elastic waves", *Bull. Seis. Sot. Am.,* 76, 1115-l 132.

Bayrakçı G., 2009, *Hétérogénéité 3D de la croûte supérieure sous la Mer de Marmara: tomographie sur une grille de sismomètres fond de mer et de profils de tirs*, Ph. D. Thesis, Institut de Physique du Globe de Paris Université Denis Diderot.

Bayrakci, G.; M. Laigle, A. Bécel, A. Hirn, T. Taymaz, S. Yolsal-Cevikbilen, 2013, "3-D sediment-basement tomography of the Northern Marmara trough by a dense OBS network at the nodes of a grid of controlled source profiles along the North Anatolian fault", Geophys. J. Int. 194, pp. 1335-1357.

Bécel, A., M. Laigle, B. de Voogd, A. Hirn, T. Taymaz, A. Galvé, H. Shimamura, Y. Murai, J. Lépine, M. Sapin and S. Özalaybey, 2009, "Moho, crustal architecture and deep deformation under the North marmara trough, from the seismarmara leg1 offshore-onshore reflection-refraction survey", *Tectonophysics,* Vol. 467, pp. 1–21.

Bécel, A., M. Laigle, B. Voogd, A. Hirn, T. Taymaz, S. Yolsal-Cevikbilen, H. Shimamura, 2010, "North Marmara Trough architecture of basin infill, basement and faults, from PSDM refl ection and OBS refraction seismics", *Tectonophysics*, Vol. 490, pp. 1–14, doi:10.1016/j.tecto.2010.04.004.

Berg, M., O. Cheong, M. van Kreveld and M. Overmars, 2008, *Computational Geometry: Algorithms and Applications*, Springer-Verlag, 3rd edition.

Beskos, D. E., 1997, "Boundary elements methods in dynamic analysis: Part II", *Appl. Mech. Rev. (ASME*), Vol. 50, No. 3, pp. 149-197.

Birgoren, G., H. Sekiguchi, and K. Irikura, 2004, "Rupture model of the 1999 Duzce, Turkey, earthquake deduced from high and low frequency strong motion data", *Geophys. Res. Lett.* Vol. 31, no. 5, L05610, doi 10.1029/2003GL019194.

Birgoren, G., O. Özel and B. Siyahi, 2009, "Bedrock Depth Mapping of the Coast South of İstanbul:Comparison of Analytical and Experimental Analyses", Turkish Journal of Earth Sciences (Turkish J. Earth Sci.), Vol. 18, pp. 315–329.

Bohlen, T. and E.H. Saenger, 2006, "Accuracy of heterogeneous staggered-grid finite-difference modeling of rayleigh waves", Geophysics, Vol. 71, pp. 109–115.
Bonnet, M., 1999, *Boundary integral equation methods for solids and fluids*, Wiley.

Boore, D. M., 1970, "Love waves in nonuniform waveguides: finite difference calculations", *J. Geophys. Res.*, Vol. 75, pp. 1512-1527.

Boore, D. M., 1972, *Finite difference methods for seismic wave propagation in heterogeneous materials, in Methods in Computational Physics*, Academic Press, pp. 1-37.
Bouchon, M., 1981, "A simple method to calculate Green's functions for elastic layered media", *Bull. Seism. Soc. Am.*, Vol. 71, pp. 959-971.

Bouchon, M., 2003, "A Review of the Discrete Wavenumber Method", *Pure appl. geophys.* Vol. 160, pp. 445–465.

Bozkurt, E., 2001, "Neotectonics of Turkey – a synthesis", *Geodinamica Acta,* Vol. 14, pp.3–30.

Bulut, F., M. Bohnhoff, W. L. Ellsworth, M. Aktar and G. Dresen, 2009, "Microseismicity at the North Anatolian Fault in the Sea of Marmara offshore Istanbul, NW Turkey", *Journal of Geophysical Research:Solid Earth, Vol.114,* doi:10.1029/2008JB006244.

Büyükakpınar, P., 2013 , *The crustal structure of the Marmara region using receiver function analysis*, M.S. Thesis, Kandilli observatory and Research Institute.

Chaljub, E. and B. Valette, 2004, "Spectral element modelling of three dimensional wave propagation in a self-gravitating Earth with an arbitrarily stratified outer core", *Geophys. J. Int., Vol.* 158, pp. 131–141.

Chaljub, E., Y. Capdeville and J.P. Vilotte, 2003, "Solving elastodynamics in a fluid-solid heterogeneous sphere: a parallel spectral element approximation on non-conforming grids", *J. Comput. Phys., Vol.* 187, pp. 457–491.

Charney, J. G., R. Fjørtoft, J. von Neumann, 1950, "Numerical Integration of the Barotropic Vorticity Equation", *Tellus,* Vol. 2: pp. 237–254.

Clayton, R. and B. Engquist, 1997, "Absorbing boundary conditions for acoustic and elastic wave equations", *Bull. Seism. Soc. Am.* Vol. 67, pp. 1529-1540.

Crank, J. and P. Nicolson, 1947, "A Practical Method for Numerical Evaluation of Solutions of Partial Differential Equations of Heat Conduction Type", *Proc. Camb. Phil. Soc.* Vol. 43: pp. 50–67.

Cohen, G., P. Joly and N. Tordjman, 1993, "Construction and analysis of higher-order finite elements with mass lumping for the wave equation", *Proceedings of the second international conference on mathematical and numerical aspects of wave propagation*, edited by R. Kleinman, pp. 152–160, SIAM, Philadephia, PA.

Çağatay, M. N., N. Görür, R. Flecker, M. Sakınç, C. Tünoğlu, R. Ellam, W. Krijgsman, S. Vincent and A. Dikbaş, 2006, "Paratethyan–Mediterranean connectivity in the Sea of Marmara region (NW Turkey) during the Messinian", *Sedimentary Geology*, 188–189, pp. 171–187.

Delaunay, B., 1934, "Sur la sphere vide", *Bulletin de l'Académie des Sciences de l'URSS, Classe des sciences mathématiques et naturelles*, No. 6, pp. 793–800.

Dewey, J. F. and A. M. C. Sengör, 1979, "Aegean and surroundings regions: Complex multiplate and continuum tectonics in a convergent zone", *Geolog. Soc. of Amer. Bull.*,Vol. 90, pp. 84–92.

Durran, D. R., 1999, *Numerical Methods for Wave Equations in Geophysical Fluid Dynamics*, Springer.

Erdik, M., Y. Fahjan, O. Özel, H. Alcik, A. Mert, and M. Gül, 2003b, "Istanbul Earthquake Rapid Response and the Early Warning System", *Bulletin of Earthquake Engineering*, Vol.1, pp. 157-163.

Ergin, K., U. Güçlü and Z. Uz, 1967, "A catalogue of earthquakes for Turkey and surrounding area (11 A.D. to 1964 A.D.) ", *Tech. Univ. Istanbul, Fac. Mining Eng., Publ.*, No. 24, pp. 169.

Ergün, M. and E. Özel, 1995, "Structural relationship between the Sea of Marmara Basin and the North Anatolian Fault Zone", *Terra Nova*, Vol. 7, pp. 278-288.

Eroskay, S.O., 1985, "Graywackes of İstanbul Region", *Proceedings of International Symposium on Design of Supports to Deep Excavations*, Turkish Group of Soil Mechanics, Bosphorus University, pp. 41-44.

Falk, J., E. Tessmer, and D. Gajewski, 1996, "Tube wave modelling by the finite-differences method with varying grid spacing", *PAGEOPH*, Vol. 148, pp. 77-93.

Frankel, A.D. and Stephenson, W.J., 2000, "Three-dimensional simulations of ground motions in the Seattle region for earthquakes in the Seattle fault zone", Bulletin of the Seismological Society of America, v. 90, p. 1251-1267.

Frankel, A.D, D. Carver, E. Cranswick, T. Bice, R. Sell, and S. Hanson, 2001, "Observations of basin ground motions from a dense seismic array in San Jose, California", Bull. Seism. Soc. Am., Vol., pp. 1–12.

Graves, R. W., 1993, "Modeling three-dimensional site response effects in the Marina district basin", San Francisco, California, *Bull. Seism. Soc. Am.*, Vol. 83, pp.1042-1063.

Graves, R.W., 1996, "Simulating seismic wave propagation in 3D elastic media using staggered-grid finite differences", *Bull. Seism. Soc. Am.,* Vol. 86, pp. 1091-1106.

Görür, N., M.N. Çağatay, M. Sakınç, M. Sümengen, K. Şentürk, C. Yaltırak and A. Tchpalyga, 1997, "Origin of the Sea of Marmara from Neogene to Quaternary paleogeographic Evolution of its frame", *Int. Geol. Rev.,* Vol. 39, pp. 342 – 352.

Gürer, Ö. F., E. Sangu and M. Özburan, 2006, "Neotectonics of the SW Marmara region, NW Anatolia, Turkey", *Geological Magazine*, Vol. 143, pp 229-241.

Gürbüz, C., S. Puskulcu and S. B. Ucer, 1992, *A study of crustal structure in the Marmara region using earthquake data in Multidisciplinary research on fault activity in the western part of the NAF,* (eds. A.M. Isıkara and Y Honkura), B.U, Report 4, 29-41.

Gürbüz, C., M. Aktar, M., H. Eyidoğan, A. Cisternas, H. Haessler, A. Barka, M. Ergin, N. Türkelli, O. Polat, B. Üçer, S. Kuleli, Ş. Barış, B. Kaypak, T. Bekler, E. Zor, F. Biçmen and A. Yörük, 2000, "The seismotectonics of the Marmara region (Turkey): results from a microseismic experiment", *Tectonophysics*, Vol. 316, pp. 1-17.

Güvercin, S., 2013, *3D P Waveelocity structure of Marmara region using local earthquake tomopgraphy*, M.S. Thesis, Kandilli observatory and Research Institute.

Havskov, J. and L. Ottemöller, 1999, "SeisAnEarthquake analysis software", *Seismological Research Letters*, Vol. 70.

Hoşgören, M. Y., 1995, *İzmit Körfezi Havzasının Jeomorfolojisi*, (ed. E. Meriç, İzmit Körfezi Kuvaterner İstifi içinde) pp.343-348, Kocaeli.

Hubert-Ferrari, A., A. Barka, E. Jacques, S. Nalbant, B. Meyer, R. Armijo, P. Tapponnier and G.C.P. King, 2000, "Seismic hazard in the Marmara Sea region following the 17 August 1999 Izmit earthquake", *Nature*, Vol. 404, pp. 269-273.

Idriss, I.M. and J.I. Sun, 1992, *User's Manual for SHAKE91: A Computer Program for Conducting Equivalent Linear Seismic Response Analyses of Horizontally Layered Soil Deposits*. Center for Geotechnical Modeling, University of California, Davis.

Imren, C., X. Le Pichon, C. Rangin, E. Demirbag, B. Ecevitoglu and N. Görür, 2001, "The North Anatolian Fault within the Sea of Marmara: a new interpretation based on multi-channel seismic and multi-beam bathymetry data", *Earth and Planetary Science Letters,* Vol. 186, pp. 143-158.

Isaacson, E. and H. B. Keller, 1966, *Analysis of Numerical Methods*, J. Wiley & Sons, New York.

İstanbul Büyüükşehir Belediyesi, 2007, *Avrupa yakası güneyi mikrobölgeleme çalışması yönetici özeti*, Deprem Risk Yönetimi Ve Kentsel İyileştirme Daire Başkanlığı, Deprem Ve Zemin İnceleme Müdürlüğü.

İstanbul Büyüükşehir Belediyesi, 2009, *Anadolu yakası mikrobölgeleme rapor ve haritalarının hazırlanması*, Deprem Risk Yönetimi Ve Kentsel İyileştirme Daire Başkanlığı, Deprem Ve Zemin İnceleme Müdürlüğü.

Jackson, J., and D. McKenzie, 1984, "Active tectonics of the Alpine-Himalayan Belt between western Turkey and Pakistan", *Geophys. J. R. Astr. Soc.*, Vol. 77, pp. 185–264.

Jastram, C. and E. Tessmer, 1994, "Elastic modelling on a grid with vertically varying spacing", *Geophysical Prospecting*, Vol. 42, pp. 357-370.

Kang, T.S. and Ch.E. Baag, 2004, "An efficient finite-difference method for simulating 3D seismic response of localized basin structures", *Bull. Seism. Soc. Am.*, 94, 1690-1705.

Karabulut, H., M-P. Bouin, M. Bouchon, M. Dietrich, C. Cornou and M. Aktar, 2002, "The seismicity in the Eastern Marmara Sea after the 17 August 1999 İzmit Earthquake", *Bullutin of Seismological Society of America*, Vol. 92, pp. 387-393.

Karabulut, H., S. Özalaybey, T. Taymaz, M. Aktar, O. Selvi and A. Kocaoğlu, 2003, "A tomographic image of the shallow crustal structure in the Eastern Marmara", *Geophysical Research Letters*, Vol. 30, pp. 10-1–10-4.

Karabulut H., A.Paul, T. Ergün, D. Hatzfeld, D. M.Childs and M. Aktar, 2013, "Long-wavelength undulations of the seismic Moho beneath the strongly stretched Western Anatolia", *Geophys. J. Int*., Vol.194, pp.450-464.

Kaya, O., 1971, "İstanbul'un Karbonifer Stratigrafisi", *TJKBüL* 14/2, pp. 143-201.

Kaya, O., 1973, *Palaeozoic of İstanbul*, E.Ü.F.F. Kitapları, No. 40.

Kelly, K.R., R.W. Ward, S. Treitel and R.M. Alford, 1976, "Synthetic seismograms: a finite-difference approach", *Geophysics*, Vol. 41, pp. 2-27.

Ketin, İ., 1973, *Umumi Jeoloji (General Geology),* Published by İTÜ, 4th Ed.

Ketin, İ., 1991, *İstanbul Jeoloji Haritası*, MTA Jeoloji Veri Bankası, Ankara.

Khazaei H. and A. Mohades, 2008, "Fingerprint Matching Algorithm Based On Voronoi Diagram", *International Conference on Computational Sciences and Its Applications ICCSA*, pp. 433-440, doi: 10.1109/ICCSA.2008.52.

Kissling, E., W. L. Ellsworth, D. Eberhart-Philips and U. Kradolfer, 1994, "Initial reference models in seismic tomography" *J. Geophys. Res.* Vol. 99, pp. 19635-19646.

Kissling, E., U. Kradolfer and H. Maurer, 1995, *VELEST user's guide-short introduction*, *Techn. Rep.*, Institute of Geophysics, ETH Zürich.

Komatitsch, D. and J.P. Vilotte, 1998, "The Spectral Element Method: An Efficient Tool to Simulate the Seismic Response of 2D and 3D Geological Structures", *Bulletin of the Seismological Society of America*, Vol. 88, pp. 368-392.

Komatitsch, D. and J. Tromp, 1999, "Introduction to the spectral element method for three dimensional seismic wave propagation", *Geophys. J. Int.,* Vol. 139, pp. 806–822.

Komatitsch, D., and J. Tromp, 2002a, "Spectral-element simulations of global seismic wave propagation-I. Validation", *Geophys. J. Int.*,Vol. 149, pp. 390–412.

Komatitsch, D., and J. Tromp, 2002b, "Spectral-element simulations of global seismic wave propagation-II. 3-D models, oceans, rotation, and self-gravitation", *Geophys. J. Int.*, Vol. 150, pp. 303–318.

Komatitsch, D., Q. Liu, J. Tromp, P. Suss, C. Stidham, and J. H. Shaw, 2004, "Simulations of ground motion in the Los Angeles basin based upon the spectral element method", *Bull. Seism. Soc. Am.*, Vol. 94, pp. 187-206.

Komatitsch, D., S. Tsuboi and J. Tromp, 2005, "The spectral-element method in seismology, in "Seismic Earth: Array Analysis of Broadband Seismograms"", edited by Alan Levander and Guust Nolet, *American Geophysical Union, Geophysical Monograph Series*, Vol. 157, pp.205-227.

Kristek, J. and P. Moczo, 2003, "Seismic-wave propagation in viscoelastic media with materialdiscontinuities: A 3D fourth-order staggered-grid finite-difference modeling", *Bull. Seism. Soc. AM.*, Vol. 93, pp. 2273-2280.

Laigle, M., A. Bécel, B. de Voogd, A. Hirn, T. Taymaz and S. Ozalaybey, 2008, "A first deep seismic survey in the Sea of Marmara: Deep basins and whole trust architecture and evolution", *Earth Planet. Science Letters*, Vol. 270, pp. 168–179.

Lay T. and T. C., Wallace, 1995, *Modern Global Seismology,* Academic Press, California,USA.

Lee, W. H. K. and J. C. Lahr, 1975, *HYP071 (Revised): A computer program for determining hypocenter, magnitude, and first motion pattern of local earthquakes,* U. S. Geological Survey Open File Report, 75-311, pp. 113.

Le Pichon, X., A.M.C. Sengör, E. Demirbag, C. Rangin, C. Imren, R. Armijo, N. Görür, N. Cagatay, B. Mercier de Lepinay, B. Meyer, R. Saatcilar and B. Tok, 2001, "The active Main Marmara Fault", *Earth and Planetary Science Letters*, Vol. 192, pp. 595-616.

Le Pichon, X., N. Chamot-Rooke, C. Rangin, C. and A. M. C. Sengör, 2003, "The North Anatolian Fault in the Sea of Marmara", *Journal of Geophysical Research*, Vol. 108, B4, 2179, doi:10.1029/2002JB001862.

Le Pichon and C. Kreemer, 2010, "The Miocene to Present kinematic evolution of the eastern Mediterranean and Middle East and its implications for Dynamics", *Annual Review of Earth and Planetary Sciences,* Vol. 38, pp. 323-351.

Levander, A.R., 1988, "Fourth-order finite-difference P-SV seismograms", *Geophysics,* Vol. 53, pp. 1425-1436.

Li S. C., Z. H. Xu, G. W. Ma and W. M. Yang, 2014, "An adaptive mesh refinement method for a medium with discrete fracture network: The enriched Persson's method", *Finite Elements in Analysis and Design, Elseiver*, Vol. 86, pp. 41-50.

Madariaga, R., 1976, "Dynamics of an expanding circular fault", *Bull. Seism. Soc. Am.*, Vol. 67, pp. 163-182.

McClusky, S., S. Balassanian, A. Barka, C. Bemir, S. Ergintav, I. Georgiev, O. Gurkan, M. Hamburger, K. Hurst, H. Kahle, K. Kastens, G. Kekelidze, R. King, V. Kotzev, O. Lenk, S. Mahmoud, A. Mishin, M. Nadariva, A. Ouzounis, D. Paradissis, Y. Peter, M Prilepin, R. Reilinger, I. Sanli, H. Seeger, A. Tealeb, M. N. Toksöz and G. Veis, 2000, "Global Positioning System constraints on plate kinematics and dynamics in the eastern Mediterranean and Caucasus", *Journal of Geophysical Research*, Vol. 105, B3, pp. 5695-5719.

McKenzie, D., 1972, "Active tectonics of the Mediterranean region", *Geophys. J. R. Astr. Soc.,* Vol. 30, No. 2, pp. 109– 185.

Moczo, P., 1989, "Finite-difference technique for SH-waves in 2-D media using irregular grids - application to the seismic response problem", *Geophys. J. Int.,* Vol. 99, pp. 321-329.

Moczo, P. and P.Y. Bard, 1993, "Wave diffraction, amplification and differential motion near strong lateral discontinuities", *Bull. Seism. Soc. Am.,* Vol. 83, pp. 85-106.

Moczo, P., J. Kristek and E. Bystrıcký, 2001, "Effıcıency and Optımızation of the 3-D Finite-difference modeling of Seismic ground motion", *J. Comp. Acous*., Vol.09, pp.593.

Moczo, P., J. Kristek, and L. Halada, 2004, *The Finite-Difference Method for Seismologists-An Introduction*, Comenius University*,* Bratislava.

Moczo, P., J. Kirstek, M. Galis, P. Pazak and M. Balazovjech, 2007, "The Finite-Difference and Finite-Element Modeling of Seismic Wave Propagation and Earthquake Motion", *Acta Physica Slovaca*, Vol. 57, pp.177-406.

Morton, K. W. and D. F. Mayers, 1994, *Numerical Solution of Partial Differential Equations,* Cambridge University Press.

Nilsson, S., N. A. Petersson, B. Sjögreen and H. O. Kreiss, 2007, "Stable difference approximations for the elastic wave equation in second order formulation", *Society for Industrial and Applied Mathematics*, Vol. 45, pp. 1902–1936.

Ohminato, T. and B. A. Chouet, 1997, "A free-surface boundary condition for including 3D topography in the finite-difference method", *Bull. Seism. Soc. Am.* Vol. 87, pp. 494-515.

Okay, A.I. and O. Tüysüz, 1999, "Tethyan sutures of Northern Turkey. In The Mediterranean Basins: Tertiary extension within the Alpine Orogen", (eds. B. Durand, L. Jolivet, F. Horvat and M. Séranne), *Geological Soc., London. Special pub.* Vol. 156, pp. 475-515.

Okay, A.I., E. Demirbağ, H. Kurt, N. Okay and İ. Kuşçu, 1999, "An active, deep marine strike slip basin along the North Anatolian Fault in Turkey", *Tectonics*, No. 18, pp. 129-148.

Okay, A.I., A. Kaslilar-Özcan, C. Imren, A. Boztepe-Güney, E. Demirbag and I. Kuscu, 2000, "Active faults and evolving strike-slip basins in the Marmara Sea, northwest Turkey: a multichannel seismic reflection study", *Tectonophysics*, 321, 189-218..

Okay, A.I., 2008, "Geology of Turkey: A synopsis", *Anschnitt*, Vol. 21, pp. 19-42.

Olempska E., A. Nazik, Ş. Çapkınaoğlu and D. G. Saydam-Demiray, 2015, "Lower Devonian ostracods from the Istanbul area, Western Pontides (NW Turkey): Gondwanan and peri-Gondwanan affinities", *Geological Magazine*, Vol. 152, pp 298-315.

Olsen, K. B. and R. J. Archuleta, 1996, "Three-dimensional simulation of earthquakes on the Los Angeles fault system", Bull. Seismol. Soc. Am., Vol. 86, pp. 575-596.

Olsen, K. B., 1991, "Seismic hazard analysis in Salt Lake Valley by finite-difference simulation of three dimensional elastic wave propagation", *5th Annual INEL Computing Symposium (Idaho Falls, ID) Proceedings*, 20.

Olsen, K. B., 2000, "Site amplification in the Los Angeles basin from three-dimensional modeling of ground motion", *Bulletin of the Seismological Society of America,* 90, pp.77-94.

Önalan, M., 1981, "Depositional environment of İstanbul Ordovician and Silurian sequence: *İstanbul Earth Science Review*", Vol.2, No. 3-4, pp. 161-177.

Özgül, N., 2011*, İstanbul il alanının jeolojisi*, İstanbul Büyükşehir Belediyesi, İstanbul kent jeolojisi projesi.

Özgül, N., 2012, "Stratigraphy and some structural features of the İstanbul Palaeozoic", *Turkish J. Earth Sciences*, vol. 21, pp. 817-866.

Parke, J.R., T. A. Minshull, R. S. White, D. McKenzie, I. Kuscu, J. M. Bull, N. Görür and C. Sengör, 1999, "Active faults in the Sea of Marmara, western Turkey, imaged by seismic reflection profiles", *Terra Nova*, Vol. 11, pp. 223-227.

Parsons, T., 2004, "Recalculated probability of M ≥ 7 earthquakes beneath the Sea of Marmara, Turkey", *Journal of Geophysical Research*, 109, B05304, doi: 10.1029/2003JB002667.

Petersson, N.A. and B. Sjögreen, 2010, "Stable grid refinement and singular source discretization for seismic wave simulations", *Comm. Comput. Phys.*, Vol. 8, No. 5, pp. 1074–1110.

Petersson N. A. and B. Sjögreen, 2011, *User's guide to WPP version 2.1.5*, Center for Applied Scientific Computing, Lawrence Livermore National Laboratory, CA.

Picozzi, M., A. Strollo, S. Parolai, E. Durukal, O. Ozel, S. Karabulut, J. Zschau and M. Erdik, 2009, "Site characterization by seismic noise in Istanbul, Turkey", *Soil. Dyn. Earthq. Eng.*, 29(3), pp. 469–482.

Pinar, N. and E. Lahn, 1952, "Descriptive catalogue of Turkish earthquakes", *Ministry of Construction, Publ.* Ser. 6, No. 36, 153.

Pitarka, A. ,1999, "3D elastic finite-difference modeling of seismic motion using staggered grids with nonuniform spacing", *Bull. Seism. Soc. Am.* Vol.89, pp. 54–68.
Priolo, E., J. M. Carcione and G. Seriani, 1994, "Numerical simulation of interface waves by high-order spectral modeling techniques", *J. Acoust. Soc. Am.*, Vol. 95, pp. 681–69.

Pulido N., A. Ojeda, K. Atakan and T. Kubo, 2004, "Strong ground motion estimation in the Sea of Marmara region (Turkey) based on a scenario earthquake", *Tectonophysics*, Vol. 391, pp. 357–374.

Sanchez-Sesma, F.J. and F. Luzon, 1995, "Seismic Response of Three-Dimensional Alluvial Valleys for Incident P, S and Rayleigh Waves", *Bulletin of the Seismological Society of America*, Vol. 85, pp. 269-284.

Semblat J.F. and J. J. Brioist, 2000a, "Efficiency of higher order finite elements for the analysis of seismic wave propagation", *Journal of Sound and Vibration*, Vol. 231, No. 2, pp. 460-467.

Semblat, J.F., A. M. Duval A. M. and P. Dangla, 2000b, "Numerical analysis of seismic wave amplification in Nice (France) and comparisons with experiments", *Soil Dynamics and Earthquake Eng.*, Vol. 19, No.5, pp. 347-362.

Semblat, J.F., M. Kham and P. Y. Bard, 2008, "Seismic wave propagation in alluvial basins and influence of site-city interaction", *Bulletin of the Seismological Society of America*, Vol. 98, No.6, pp. 2665-2678.

Semblat, J., 2011, "Modeling Seismic Wave Propagation and Amplification in 1D/2D/3D Linear and Nonlinear Unbounded Media", *Int. J. Geomech., SPECIAL ISSUE: Material and Computer Modeling*, Vol.11, pp. 440-448.

Serpentine Wave Propagation, https://computation.llnl.gov/project/serpentine/, Lawrence Livermore National Laboratory, USA.

Sipahioğlu, S., 1984, "Kuzey Anadolu Fay Zonu ve .Çevresinin Deprem Etkinliğinin İncelenmesi", *Deprem Araştırma Bül*. No45, s. 1-149.

Siyako, M., T. Tanis and F. Saroglu, 2000, "Marmara Deniz aktif fay geometrisi", *TÜBITAK Bilim Tek. Derg.,* Vol. 388, pp. 66-71.

Sjögreen B. and N. A. Petersson 2012, "A Fourth Order Accurate Finite Difference Scheme for the Elastic Wave Equation in Second Order Formulation", *Journal of Scientific Computing*, Vol. 52, pp. 17-48.

Skarlatoudis A. A., C. B. Papazachos, N. Theodoulis, "Spatial distribution of site effects and wave propagation properties in Thessaloniki (N. Greece) using a 3-D finite difference method", *Geophysical Journal International*, Vol.185, pp. 485-513.

Smith, A.D. and T. Taymaz, 1995, "High Resolution Seismic Profiling in the Sea of Marmara (NW Turkey): Late Quaternary Tectonics and Sedimentation", *Bulletin of Geological Society of America*, Vol.107, 923-936.

Soysal H., S. Sipahioglu, D. Kolcak and Y. Altinok, 1981, *Turkiye ve Cevresinin Tarihsel deprem Katalogu*, TUBITAK, Proje no. TBAG 341, Istanbul, pp. 86.

Stein, R.S., A. Barka and J.H. Dieterich, 1997, "Progressive failure on the North Anatolian fault since 1939 by earthquake stress triggering", *Geophysical Journal International,* Vol. 128, pp. 594-604.

Şahin Ş., X. Bao, N. Turkelli, E. Sandvol, U.Teoman and M. Kahraman, 2013, "Lg Wave Attenuation in the Isparta Angle and Anatolian Plateau (Turkey) " *Pure and Applied Geophysics*, Vol.170, pp. 337-351.

Şengör, A.M.C., 1979, "The North Anatolian transform fault: its age, offset and tectonic signifiance", *Jour. Geol. Soc. Lond.*, Vol. 136, pp. 269-282.

Şengör, A.M.C. and Y. Yılmaz, 1981, "Tethyan evolution of Turkey: a plate tectonic approach", *Tectonophysics,* Vol. 75, pp. 181-241.

Şengör, A.M.C, N. Görür and F. Şaroğlu, 1985, "Strike-slip faulting and related basin formation in zones of tectonic escape : Turkey as a case study, in Strike-slip deformation, basin formation and sedimentation", edited by K.T. Biddle and N.C Blick, *Soc. Econ. Palen. Mine. Spec. Publication*, pp. 227-264.

Tromp J., 2007, "Theory and Observations – Forward Modeling and Synthetic Seismograms: 3-D Numerical Methods", *Treatise on Geophysics*, pp.191-217.

Turkelli, N., E. Sandvol, E. Zor,R. Gok, T. Bekler, A. Al-Lazki, H. Karabulut, S. Kuleli, T. Eken, C. Gurbuz, S. Bayraktutan, D. Seber and M. Barazangi, 2003, "Seismogenic zones in Eastern Turkey", *Geophys. Res. Lett.,* 30 (24) (2003), pp. 8039.

Tüysüz, O., A.A. Barka and E. Yiğitbaş, 1998, "Geology of the Saros Graben and its implications for the evolution of the North Anatolian fault in the Ganos-Saros region, northwestern Turkey" *Tectonophysics*, Vol. 293, pp. 103-126.

Viezzoli A., A. V. Chiristiansen, E. Auken and K. Sorensen, 2007, "Spatially constrained inversion for quasi 3-D modelling of AEM data", *ASEG2007 - 19th Geophysical Conference*, pp.1-4, doi:10.1071/ASEG2007ab157.

Virieux, J., 1984, "SH-wave propagation in heterogeneous media: velocity-stress finitedifference method", *Geophysics,* Vol. 49, pp. 1933-1957.

Virieux, J., 1986, "P-SV wave propagation in heterogeneous media: velocity-stress finite-difference method", *Geophysics*, Vol. 51, pp. 889-901.

Wong, H.K., T. Lüdmann, A. Ulug and N. Görür, 1995, "The Sea of Marmara: a plate boundary sea in an escape tectonic regime", *Tectonophysics*, pp. 231-250.

Xu, S. Z., 2001, *The Boundary Element Method in Geophysics,* in Geophysical Monograph Series, Society of Exploration Geophysicists, Tulsa, Oklahoma, 169–203.

Yaltirak, C., 2002, "Tectonic evolution of the Marmara Sea and its surroundings", *Marine Geology*, Vol. 190, pp. 493-529.

Yomogida, K. and J. T. Etgen, 1993, "3-D wave propagation in the Los Angeles basin for the Whittier-Narrows earthquake", *Bull. Seism. Soc. Am.* 83, 1325–1344.

Yörük, A., 2000, "The seismotectonics of the Marmara region (Turkey): results from a microseismic experiment", *Tectonophysics*, Vol. 316, pp. 1-17.

Zahradnik, J., F. Gallovic, E. Sokos, A. Serpetsidaki, A. Tselentis and F. Gallovic, 2008, "Quick Fault-Plane Identification by a Geometrical Method: Application to the Mw 6.2 Leonidio Earthquake, 6 January 2008, Greece", *Seismological Research Letters,* Vol. 79, No 5.

Zor, E., S. Özalaybey, C. Gürbüz, 2006, "The crustal structure of the eastern Marmara region, Turkey by teleseismic receiver functions", *Geophysical Journal International*, Vol. 167, pp. 213-222.